School of Computing,

Science & Engineering

(Petroleum and Gas Engineering)

MPhil in

The Effect of Fracture Orientation on Permeability

Mabrouk D.A. Al-Shukri (@00340428)

Abstract

Shale contain tiny pores where oil and gas are trapped, and fracking is undertaken to interconnect them and to release oil and gas. Furthermore, hydraulic fracturing is the process of injecting high-pressure fluids as high as 10 k psi into rocks to fracture them, and permeability is optimised by inducing complicated fractures into the shale. Previous authors have studied fracturing orientation techniques, however, their work considered only simple fractures.

In this work, complicated fractures were considered using different shale samples from Mancos and Marcellus. To determine their permeability, these samples were induced with fractures at different orientation angles and tested at an overburden pressure of between 100 and 200 bar using a Nano-Perm machine. Computerised Tomography (CT) was also used to determine the porosity and to characterise the shale samples, with regard to crack width, crack length and to determine if there were any natural fractures. The liquid saturation method was also carried out to find the pore volume, whilst XRF fluorescence was also used to determine the chemical composition of the shale samples.

There was a good agreement in the porosity results for the two different methods used, specifically the CT scan and the saturation method. Moreover, it was found that, for the Mancos Shale, the more complex fracture had a greater permeability at ΔP's of less than 2 bar and an overburden pressure of 100 bar. The greater number of passageways within the shale through which the gas could flow can explain this. However, above a ΔP of 2 bar with overburden pressures of 150 bar on less complex fractures had a lower permeability because the overburden pressures will have reduced the gaps between the passageways due to the greater accumulated passageways, and hence the reduced flow.

For the Marcellus Shale, it was found that, at overburden pressures of more than 150 bar and for all ΔP's, the more complex fractures had a greater permeability. It was also shown that the Marcellus Shale had a greater permeability compared with Mancos. This is because the Marcellus reservoir has a marked ratio of calcium and cementing materials, which comparatively alter the rock structure and render it relatively incompressible.

Dedication

To my best beloved late brother, Ali and my adored father, God bless their souls. To my mother, may God give her happiness and a long prosperous life. Finally, to my family, especially my daughters (Sondus and Malak), and my sons (Siraj and Muhammad), may God also give them happiness and a long and prosperous life; thanks for their unlimited patience, moral support, continuous encouragement, sympathy and soothing care. “You stood by me, supported me and believed in me. Words will never say how grateful I am to you all and how wonderful you all are.”

Acknowledgements

First and foremost, I would like to express my profound and sincere gratitude to my supervisor, Dr M. Burby, for his unlimited patience, kindness, and good manners. One simply could not wish for a better or friendlier supervisor. I would also like to thank my Co-Supervisor Dr A. Nourian and Professor G. G. Nasr for their guidance, moral support, and continuous encouragement from the beginning of my MPhil research to completion.

My supervisor and co-supervisor have supported me throughout my research with their unrestrained patience and knowledge. Their detailed and constructive comments and support throughout this work were the cornerstones in building my MPhil research stage by stage. Their kind support and guidance have been of great value to me in this study.

I extend my gratitude and thanks to all who have supported me, namely: Dr G. C. Enyi, Dr David Smith, Dr Ahmad Fakhruddin, Dr Hisham Al-Shaheen and PhD students, Aminu Abba Yahaya, and Mr Alan Mappin for their additional practical and moral support.

My special loving appreciation goes to my spouse, Entissar, and to my children, Sondus, Siraj, Muhammad and Malak. They have lost a lot because of my ongoing absence whilst working on my research. Their encouragement and sympathy have been a very positive factor for me in finishing my work. My thanks are due to my loving mother and as well to the other members of my big extended family, including my brothers and sister for their loving support and encouragement.

Finally, I would like to extend my heartfelt thanks to all those who have helped me to accomplish my thesis, even by offering a smile.

Table of Contents

List of Tables

List of Figures

Chapter 1: Introduction

1.1 Introduction

The time of cheap, accessible conventional oil and gas reservoirs has nearly ended; this has resulted in a shift by the oil industry towards expensive unconventional oil and gas resources. Thus, it has been reported that conventional oil and gas extraction has reached a peak and is now about to gradually diminish (Campbell and Laherrere, 1998). Petroleum experts, encouraged by the shift of world oil prices which recently reached above $100 /bbl., have shifted their focus and efforts to increase the efficiency of the recovery process and to consider wells that were originally identified as unprofitable. The scope of this work is to investigate the effect of complex fracture orientation on the permeability of core shale samples. This leads to aid the development of fracture techniques to enhance oil/gas recovery from shale rocks.

A shale rock matrix is a sedimentary rock/reservoir formed or shaped by a build-up of clay layers, exceeding 50% clays and an inferior amount of quartz or carbonate minerals (Britt and Schoeffler, 2009). Over millions of years, it is gradually squeezed and compressed into a mudstone. Shales are formed from four main constituents: clay, quartz silt, carbon-rich organic matter, and calcium carbonate. These occur in various ratios in different types of shale, but geologists adopt the term shale to clay- and organic matter-rich mudstones that are fissile (dividable into thin beds). Shale reservoirs are typified by ultra-low permeability and porosity.

Unconventional oil and gas are mainly heavy, multifaceted, carbon-laden (carbon carrying), and imprisoned deep underground in tightly sealed formations. Unconventional oils are characteristically heavier and sourer than even the lowest class of conventional oil. To meet global requirements for high-quality oils, these oils require extra intensive treatment and processing. Therefore, unconventional oils can cost more to produce because of the increased cost of production and processing, and because of their environmental impacts.

Fracking is the procedure of injecting high-pressure liquids (as high as 10 k psi) into rocks to fracture them. These artificial or human-made fractures are kept open via proppants, for example, sand or ceramic particles. Fracking includes drilling down to about 2km vertically,

after that laterally outwards for around 3km. The first fracking stimulation was carried out in 1947 for a gas well managed by the Pan American Petroleum Corporation; this was in the Hugoton field, named Klepper Well No. 1, and was situated in Grant County, Kansas. This well initially had low productivity, and although it had been successively acidised, productivity was still low. Following the fracturing, the productivity of the well was increased and this process is now common practice for enhancing the productivity of both oil and gas wells.

Hydraulic cracks may form naturally as pressurised fluids escape from deeply buried rocks; this fractures the rocks as the fluids escape upwards. Shale contains several tiny pores where natural gas or oil may be trapped but this porosity is not interconnected, which render shales with ultra-low permeability. In order to release oil and gas, permeability must be initiated through hydraulic fracturing. Fracking creates thin, fluid-filled fissures which enable the interconnection of pores in mudstones; this enables oil and gas to flow out via the rock and towards the well (Huang et al., 2014).

Shale reservoirs are very tight due to their extreme compressibility, which is caused by the overburden load and because they are very soft with an extremely small grain size. Consequently, these characteristics affect permeability and porosity. The limited porosity and low permeability hinder the access of oil and gas inside these shales. Fracking is one of the most important methods used to overcome this obstacle and optimise these reservoirs. It achieves this by interconnecting their isolated porosity by choosing suitable fracture orientation to ease the flow of oil and gas (Shah et al, (2010).

Scholars have studied the geomechanical properties of shale reservoirs; for example, permeability, porosity and their relationship to each other (Collins and Jordan, 1961; Tickell et al., 1933). They have also researched compressibility, ductility, brittleness, rock strain, deformation, Young's Modulus and Poisson's Ratio and their influences on shale reservoir productivity (Al-Anazi et al., 2011; Gharahbagh & Fakhimi, 2011; Laudeman, & Ershaghi, 1981). They have researched parameters of pressure, confining differential and in-situ stresses, and the relationship between these stresses and permeability and porosity; as permeability and porosity decrease with additional stress (AL Qahtani et al., 2011; Cho et al., 2012; Hopkins, 1977; Katsumi et al., 2013).

Practical experience has demonstrated that not all shale formations react to fracking efficiently. It is essential to find and correctly design other fracturing methods that might overcome all or some of the confines or limits. Generally, hydraulic fracturing includes a comparatively slow loading rate on a nearby rock and causes bi-wing fracture geometries. In comparison, the explosive fracturing method involves the extreme quick loading of the formation, which produces an immediate spread of multiple fractures. Due to the great stress and heat created throughout the detonation, the near borehole region approaches its compression limit. This study will further the understanding of the complex fracture orientation type and its potential for well productivity.

1.2 Aims and Objectives of this Research

1.2.1 Aims

The aims of the research are to characterise the geomechanical properties of shales from Barnett, Eagle Ford, Mancos and Marcellus Reservoirs and to determine how simulated induced complex fractures affect permeability.

1.2.2 Objectives

The main objectives are to:

- Characterise the chemical composition of the shale samples using x-ray fluorescence (XRF);
- Measure the pore volume of the shale samples, apply a porosity calculation using the liquid saturation method and compare this porosity with the CT scan porosity to validate the results;
- Measure the porosity, crack width and crack length using a CT Scan and volume graphics;
- Measure the permeability for different fracture orientations using the Nano-Perm machine at a range of overburden pressures for the second set of shale samples (Marcellus) at 34.5, 69.0, 103.5 and 138 bar. The permeability of the third set of the shale samples (Mancos and Marcellus) is to be measured at 100, 150 and 200 bar.

1.3 Report Overview

The report is divided into five chapters, outlined as follows:

Chapter 1: Provides an introduction to the study, which provides a brief description of unconventional shale reservoirs and presents the aim and objectives of the research.

Chapter 2: Describes shale composition, shale geomechanical properties, fracking technology and pulsed fracturing. The use of analytical techniques, such as Computerised Tomography (CT) for shale characterisation, and the relationship between compressibility and porosity are also described.

Chapter 3: Describes the shale, specifically the composition of Barnett, Eagle Ford, Mancos and Marcellus. A flowchart describes the research steps. The chapter provides a discussion on the test procedures for the CT scan to measure the porosity, the crack width and crack length, the measurement of the permeability using the Nano-Perm machine and the elemental analysis of the shale using X-ray Fluorescence (XRF).

Chapter 4: Presents and discusses the results of the work. This details the permeability results and compares the results between the different shale samples, and porosity calculations; moreover, the CT scan construction images are also provided, along with the elemental analysis of the shale.

Chapter 5: Presents the conclusions and recommendations of the research into the geomechanical properties of the shale rock by testing Barnett, Eagle Ford, Mancos and Marcellus. Permeability was measured for Mancos and Marcellus but only the characterisation was determined for all four shale samples (Barnett, Eagle Ford, Mancos and Marcellus). In addition, the author recommends that further studies are conducted in different fracturing orientations to deepen the understanding of this trend by using other approaches to study permeability and physical shale composition.

Chapter 2: Literature Review

2.1 Introduction

In this chapter, the literature surrounding the research will be presented, which will cover the following areas:

- Unconventional reservoirs.
- The composition of shale.
- The geomechanical properties of shale, including permeability, Poisson's Ratio and Young's Modulus.
- Fracturing technology.
- Fracture orientations and the effect on permeability.

The link among these areas is the need for unconventional reservoirs to be hydraulically fractured to produce economical oil and gas. To achieve efficient hydraulic fracturing, it is necessary to understand the composition of shale and to use a range of geomechanical properties. These properties are porosity, permeability, Poisson's Ratio, Young's Modulus and fracturing orientation; these are essential to complete the process and obtain good results.

2.2 Unconventional Reservoirs

Unconventional oil and gas are mainly heavy, multifaceted, carbon laden, tightly sealed, and imprisoned deep underground. Unconventional oils are characteristically heavier and sourer than the lowest class of conventional oil. For them to meet global requirements for high-quality oil, they need intensive treatment and processing. Such unconventional oils would cost more in terms of production and processing and in terms of their environmental impacts. Unconventional reservoirs of oil and gas were not accessible before an understanding of advanced technology was reached in the oil industry: Unconventional reservoirs of oil and gas do not run or flow naturally via the rock, which renders them much more difficult to extract. For a simple analysis, the difference between conventional and unconventional reservoirs is the difference between a saturated sponge and a piece of saturated clay. It is easy to squeeze water from the sponge, but difficult to squeeze it from the piece of clay (Warpinski et al, . (2009).

2.3 Composition of Shale

Shale, or mudstone, is a sedimentary rock shaped over millions of years by the accumulation of clay layers (Britt and Schoeffler, 2009) that have gradually been squeezed and compacted into a mudstone. Typically, shales are formed of the following constituents: Clay minerals (55.2%), quartz (23.9%), carbonate (9.3%), feldspar (6.1%), organic matter (4.2%), Fe-oxides (0.8%), and other minerals (0.5%) (Torsaeter et al., 2012). These occur in various ratios in different shales, but geologists give the term 'shale' to clay and organic matter-rich mudstones that are fissile.

Shale reservoirs are characterised by their extremely low permeability and porosity. These reservoirs are very tight due to their extreme compressibility; this is because they are very soft and their grain sizes are extremely small. Consequently, these characteristics affect their porosity and permeability. Their low porosity and very low permeability hinder the production of large quantities of oil and gas. Fracking is one of the most important techniques used to overcome this obstacle and optimise these reservoirs. The orientation of hydraulic fracturing is very important in terms of oil well production, i.e., complex fractures (fractures at multiple different angles) add multiple channels for the oil and gas to flow through the rock to the borehole, which consequently optimises oil and gas production.

2.4 The Relationship between Compressibility and Porosity

Li et al. (2004) conducted a study entitled, "A New Relationship of Rock Compressibility with Porosity". This study developed a new formula: pore volume (Vp) = bulk volume (Vb) - solid volume (Vs), this comprises two parameters of rock: the elastic modulus and Poisson's Ratio, which are easier to assess in the test site than through compressibility. The compressibility of the rock grows when porosity increases, whilst the usual empirical rule displays the reverse. However, the new formula demonstrates that the compressibility of the rock is dependent on its rigidity. Thus, rock compressibility in a typical choice of reservoir is usually less than that of the reservoir fluid.

The relevance of the study by Li et al. to this research lies in the consideration of porosity and permeability, which are both affected by compressibility. Compressibility helps in extracting oil and gas from the pores in the rock matrices. When pore pressure reduces, the reservoir rock becomes compressed. Compressibility creates energy to help drive oil out of the reservoir rock. The rock compressibility is measured by determining the pore volume change against the pore pressure. Hall (1953) provided a plot of rock compressibility versus porosity using the statistics of his laboratory experiments. According to Hall, compressibility reduces as rock porosity becomes larger. In fact, the rigid rock matrix is less compressed and must have a slighter compressibility than a non-tight rock. Therefore, Hall's results are logically incorrect, which suggests that his core measurement for the compressibility of rock is doubtful and disputable. Moreover, Hall's plot provides the same amount of compressibility for the lithology of different rocks, which assumes they possess the same porosity value despite their different rigidities.

Rock is a porous medium, consisting of solid particles and voids between particles. As shown in Figure 2-1, the porous medium encompasses three volumes: pore volume (the volume between the grains), solid volume (the volume of the grains) and bulk volume (the volume of the grains plus the volume of the pores between the grains). The voids between the grains represent the porosity. The porosity is the bulk volume of the rock minus the volume of the grains.

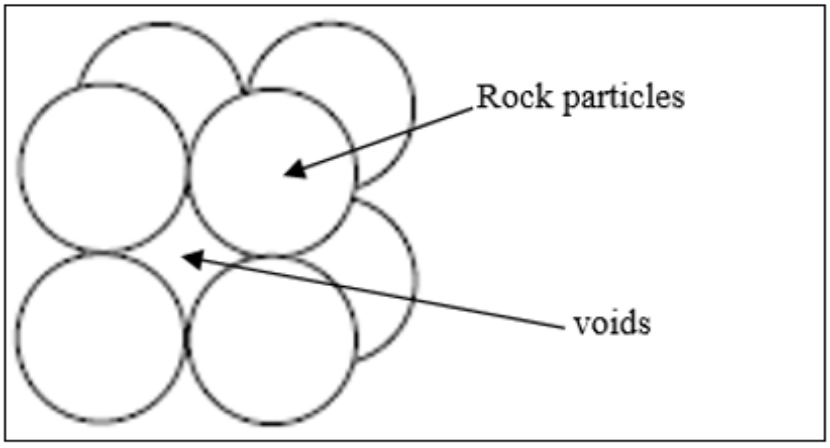

Figure 2-1: Material Composition of Rock (Li et al., 2004)

Figure 2-2 shows rock which is subjected to two stresses: external stress (σ) and internal stress/pore pressure (p). When either of the two stresses changes, all three volumes will change respectively.

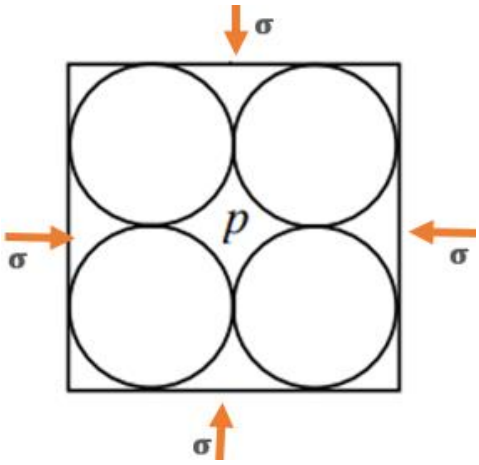

Figure 2-2: Stress Composition of Rock (Li et al., 2004)

In Figure 2-2, σ outer stress generally remains invariable and just a change in the pore volume may add to the production of oil. Changes in the pore pressure occur due to the release of fluid. The change in pore pressure triggers the geomechanics, which starts work within the rock matrix, enhancing permeability and consequently productivity because geomechanical stresses create fractures and cause the interconnection of porosity in the reservoir. The porosity is interconnected due to the fractures that occur, which lets the oil and gas accumulated in the pores enter the wellbore.

During oil production, the external stress is changeable but does not affect the production. Only the change of pore volume may affect the production of oil. Therefore, the pore volume change is the main concern of the reservoir engineer. The pore volume with pore pressure, which is commonly termed the rock compressibility, is defined as shown in Eq. 2.1:

$$\mathbf{C_p} = \frac{\mathbf{dV_p}}{\mathbf{V_p dp}} \qquad 2.1$$

Where,

C_p rock compressibility, MPa^{-1}

V_p pore volume of rock, m^3

This is based on Hall's plot of rock compressibility versus porosity values and obtained from the figures from the laboratory tests. Newman (1973) identified an analogous trend of rock compressibility by porosity value in Hall's plot by using consolidated both sandstone and limestone. The means to determine the rock compressibility by Hall, in which he found the following relationship between rock compressibility and porosity, are shown in Eq. 2.2:

$$\mathbf{C_p} = \frac{\mathbf{2.587x10^{-4}}}{\boldsymbol{\phi}^{\mathbf{0.4358}}} \qquad 2.2$$

Where,

C_p : rock compressibility, MPa^{-1}

Φ: porosity, f

Figure 2-3 illustrates Hall's relationship between porosity and compressibility. When the compressibility increases, the porosity decreases due to an increase in the compaction/compression of the rock matrix.

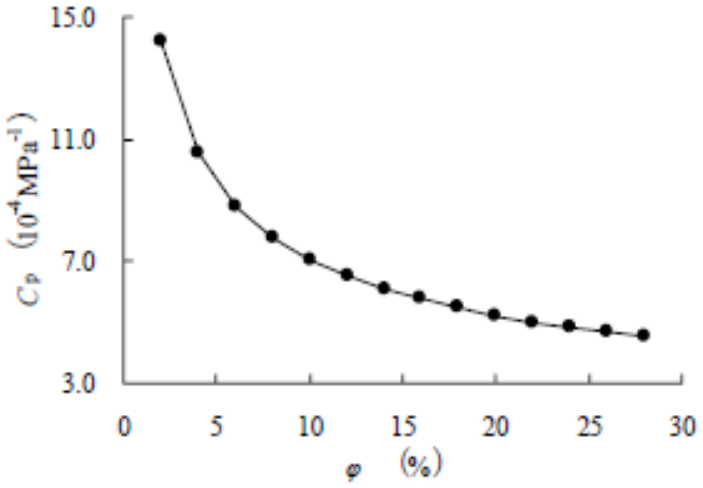

Figure 2-3: Compressibility Versus Porosity (Hall, 1953)

The deformation of the porous matrix, which is caused by the reorganisation of solid grains, is termed 'structural deformation', as shown in Figure 2-4. In this rearrangement, the volume of

the grains is not altered at all, whereas both the pore and bulk volumes are all changeable with stress alteration.

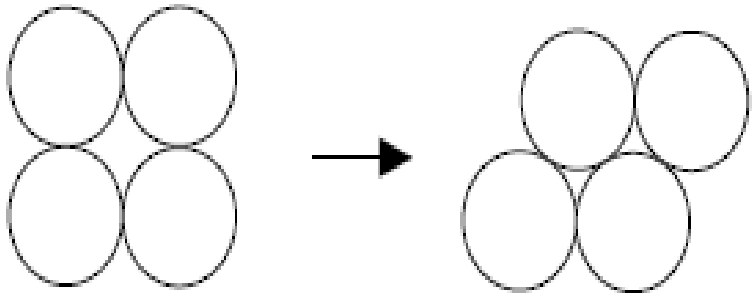

Figure 2-4: Structural Deformation of Porous Media (Li et al., 2004)

The deformation, shown in Figure 2-4, was caused by the reorganisation of solid grains. This is termed 'structural deformation'.

Figure 2-5 shows the deformation of the porous matrix, which is caused by the volume alteration of solid grains but not by their reorganisation; this is termed 'primary deformation'. In this action, the grains' arrangement is not altered at all; however, the three volumes of the porous matrix are together subject to change. This primary deformation is mostly produced in tight rock/soil due to cementation between grains.

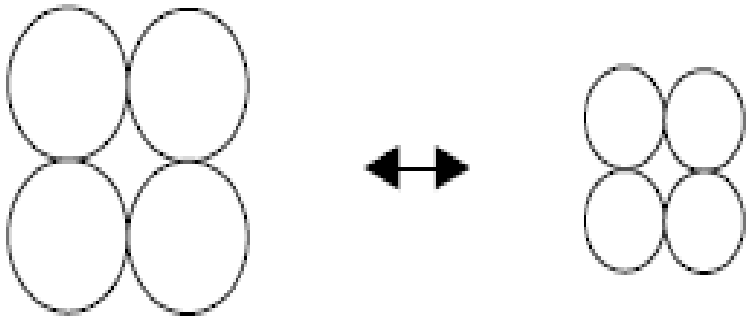

Figure 2-5: Primary Deformation of Porous Media (Li et al., 2004)

As shown in Figure 2-6, when internal stress/pore pressure differs from $\boldsymbol{p_1}$ to $\boldsymbol{p_2}$ and skeleton stress at once differs from $\boldsymbol{\sigma s_1}$ to $\boldsymbol{\sigma s_2}$, all volumes of the rock change respectively. This deformation form is primary because of the cementation between its grains, as shown in Eq. 2.3 and 2.4:

$$\mathbf{C_p = \frac{dV_s}{V_s dp}} \qquad 2.3$$

Where,

C_P MPa^{-1}

V_s : skeleton volume, m^3

P: pressure, psi: rock compressibility,

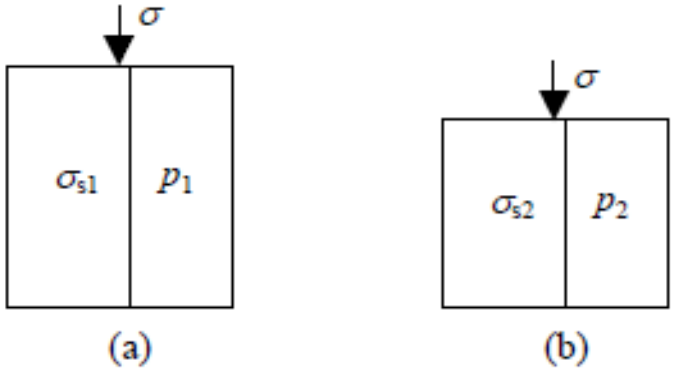

Figure 2-6: Compression of Rock (Li et al., 2004)

$$\mathbf{C_p = \frac{\phi}{1-\phi} C_s} \qquad 2.4$$

Where,

C_P : rock compressibility, MPa^{-1}

C_s : skeleton compressibility, MPa ^{3}

ϕ : porosity, f

It can be seen from Eq. 2.4 that the compressibility of rock is dependent on the mineral rigidity in rock, i.e. rigid minerals, such as calcium, quartz and silicon render the rock smaller in compressibility value. This fact may explain why shale is higher in compressibility than other rocks, for example, sandstone. Moreover, rock compressibility is also dependent on its porosity value, and loose rock may attain more compressibility.

Figure 2-7 shows the relationship between porosity and compressibility. When the porosity voids are plentiful, the compressibility increases, due to more space between the grains in the rock matrix; for example, when the compressibility is around 0.05 MPa, the porosity is around 28%, according to Hall's plot.

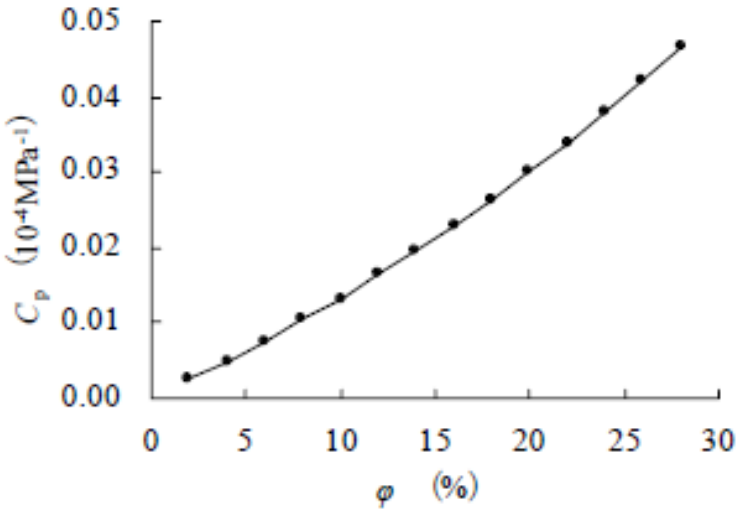

Figure 2-7: Compressibility of Rock Versus Porosity (Hall, 1953)

Rahman et al. (2009) conducted a study entitled the "Interaction between Induced Hydraulic Fracture and Pre-existing Natural Fracture in a Poro-elastic Environment: Effect of Pore Pressure Change and the Orientation of Natural Fractures". Rocks of a reservoir comprise lots of fractures, seams, bedding and defects. In models of conventional fracking, the supposition is that the induced fracture is perfect, simple, conventional, bi-wing, and spreads equally in a flat vertical to the least stress. Furthermore, obviously cracked formations may vary significantly from fracking in straight reservoirs. Owing to interaction through natural cracks, the fissure can spread unequally or in several strands or sections in naturally fractured reservoirs. The existence of natural fractures changes the way the influenced crack propagates through the rock. Daneshy (1974) showed that a fracture follows the local pathway of minimum opposition, not the global path, which leads to significant branching.

Blanton (1982, 1986) demonstrated that a crack spreading crosses an ordinary fracture, goes into the natural crack, or, in some situations, goes into the natural fracture for a small space,

then begins to spread again in an automatically favourable orientation, relying mainly on the oncoming angle.

Practical researchers propose that hydraulic fractures rise to cross-present fractures at a high differential stress and at high angles of approach. At low approach angles and small stress differences, the natural fracture opens, preventing the fracturing liquid from stopping the completed crack from crossing, at least temporarily.

Wright and Conant (1995) conducted a study entitled, "Hydraulic Fracture Reorientation in Primary and Secondary Recovery from Low-Permeability Reservoirs". They found that an in-situ stress state controls several aspects of the fracture propagation, involving: the geometry of hydraulic fractures, near-borehole crack zigzagging, and hydraulic frack direction.

Understanding the main role that the stress state plays, not just in fracking but also in the stability of wellbore and formation sand control, is a challenge the industry has long faced. It has often unsuccessfully addressed the problems by just determining the state of in-situ reservoir stress.

Wade and Bilgesu (2012) conducted a study on the "Impact of Hydraulic Fracture and Subsequent Increased Production Due to in-situ Stress Changes in the Marcellus Shale". They found that the reservoirs of shale gas are rapidly becoming a significant source of natural gas. The shale reservoirs were not previously investigated for economic production due to their extra-low permeability figures. However, by using hydraulic fracturing in combination with horizontal well completions, shale formations have become prudently producible, particularly amongst Marcellus Shale plays (a play, is a group of oil fields in the same region that are controlled by the same set of geological circumstances).

Olson et al. (2004) conducted a study on "Improving Fracture Permeability Prediction by Combining Geomechanics and Diagenesis". High temperatures and reactive liquids in sandstone reservoirs state that the interaction and response between mechanical and geochemical procedures might considerably enhance the development of rock and crack characteristics. Geomechanical modelling is a method for forecasting the spatial planning of

opening method fracture systems. A model founded on the subcritical fracture expansion is utilised to create crack trace models (Olson, 1993; Olson et al., 2001).

An essential ability of such modelling is the capability to foresee the existence or non-existence of crack assemblage, and the form of the crack length spread. The diagenesis is the alternation in interstitial water composition or change in temperature or both, which generally leads to a chemical change of the existing minerals. Diagenesis is the outcome from any system of physical, chemical, or biological change to these comparatively young deposits as they are lithified (converted into rocky material). However, the majority of current literature highlights the orientation of earth stresses (Crampin, 1987; Heffer, and Lean, 1993), the integrity in fissures, and a prone host rock as critically essential controls on porosity, liquid flow attributes, and the sensitivity to effective stress alterations (Dyke, 1995; Laubach et al., 2004; Olson and Gale, 2004).

2.5 The Role of Geomechanics in Reservoir Simulation

Gutierrex and Lewis (1998) conducted a study on the "Role of Geomechanics in Reservoir Simulation". Geomechanics is essential to explain rock deformations because of the pore pressure and temperature changes caused by the production and injection of fluids. As such, rock permeability and pore compressibility will be affected by rock failure, while the pore pressure will also vary due to changes in the volume of pores. It is recognised that geomechanical reaction and fluid flow is a fully-coupled procedure because pore pressure modifications influence rock mechanical reactions and vice versa, and these two processes occur at the same time.

The geomechanics, shown in Figure 2-8, is essential to explain rock deformations because of the pore pressure and temperature alterations caused by the production and injection of fluid. The pore pressure changes influence the rock mechanical reaction. Consequently, injecting fluid into the formation and producing oil initiates geomechanics, which fractures the rock and consequently increases the permeability and production, and vice versa.

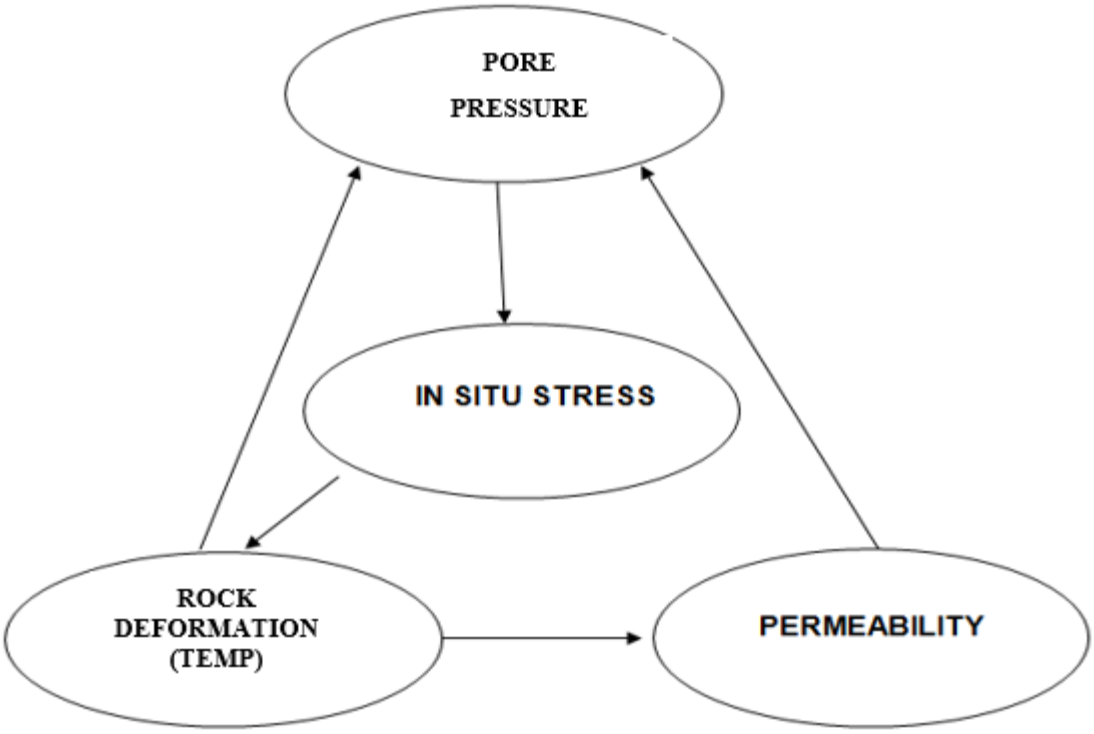

Figure 2-8: Schematic of the Interaction between Geomechanics and Fluid Flow in a Deformable Reservoir (Can, 1992; Settari et al., 1992; Terzaghi et al., 1925)

Okubo et al. (2013) conducted a study on "Stress Distribution in Fractured Medium and Fracture Propagation due to Formation Pressure Changes" and found that fracking is a crucial scheme to enhance fluid production in the development of a hydrocarbon basin in conjunction with different well testing techniques, for instance, drill stem tests of build-up, etc.

The local stress field that might be measured by acoustic emissions analysis during drilling governs crack propagation. In recent years, it has similarly become well known that fracking a well plays a key part in the growth of shale oil. It is also recognised that the length and direction of cracks induced by fracking are powerfully affected by the earth's top layer stress enclosure under which any basin is located. Thus, it is essential to have knowledge of the local stress field and the rock physical parameters of the basin formations prior to fracturing. To represent failures in the earth's top layer materials in a basic way, a lengthy finite element technique is utilised, (Belytschko and Black, 1999).

2.6 Fracability Evaluation in Shale Reservoirs

Jin et al. (2014) conducted a study on "Fracability Evaluation in Shale Reservoirs - An Integrated Petrophysics and Geomechanics Approach". Brittleness is considered one of the most significant mechanical properties of rock, which has been integrated in nearly all shale petrophysics reports of unconventional reservoirs (Chong et al., 2010; Jarvie et al., 2007; Li et al., 2013; Rickman et al., 2008; Wang and Gale, 2009). Moreover, it is presumed that formations that contain high brittleness are simple to fracture (Alassi et al., 2011; Kundert and Mullen, 2009; Rickman et al., 2008; Slatt and Abousleiman, 2011), but this presumption is not always correct, as a formation with higher brittleness may act as a fracture barrier. For example, dolomitic limestone has a high brittleness, but in shale reservoirs, it is a fracture barrier since, in shale formation, the fracture gradient is less than that of a dolomitic limestone structure (Bruner and Smosna, 2011). Consequently, brittleness alone is not sufficient to characterise the fracability of unconventional shale reservoirs. In fracking, extra parameters, for instance, specific energy, ought to be incorporated to evaluate the fracture (Altindag, 2010).

Collins and Jordan (1961) conducted a study entitled, "Porosity and Permeability Distribution of Sedimentary Rocks". Porosity is a measure of a rock's ability to contain fluids. Collins and Jordan found that porosity and permeability, in general, decrease with increasing depth; this is because of growing compaction due to the increasingly confining pressure and the increasing load of newer overlying burden sedimentation. They also found porosity as a ratio between the bulk volume of the rock and the pore space volume of the same rock, as shown in Eq. 2.5. Sometimes, there is porosity but no interconnection; therefore, in this case, there is porosity, but the permeability is zero or very low.

$$\emptyset = \frac{\textbf{pore volume}(\textbf{m}^3)}{\textbf{bulk volume } (\textbf{m}^3)} \qquad 2.5$$

Where,

ϕ : porosity, %

Permeability is an indication of the capability for fluids, gas or liquid, to flow through rocks. High permeability indicates that fluid passes through the rock more easily. Permeability within a fractured porous media is mostly controlled by the geometry, the interconnection of the pores and some fractures, and by the stress state.

Permeability (K) is calculated as follows (Eq. 2.6) (El-Sayed and Ehab, 1999):

$$\mathbf{K} = \frac{\mathbf{q}}{\mathbf{2\pi l(p_2 - p_1)}} \mathbf{ln} \frac{\mathbf{r_2}}{\boldsymbol{r_1}} \qquad 2.6$$

Where,

q = flow rate, m^3; K = permeability constant (mD); l = length of cylinder (m); r_2 = radius of cylinder (m); r_1 = radius of axial hole (m), P_1 = pressure of fluid in axial hole (pa); P_2 = pressure of surrounding fluid (pa).

Youn and Gutierrez (2011) conducted a study into the "Effect of Fracture Distribution on Permeability of Fractured Rock Masses". They identified that fractured rock permeability is an essential issue in various fields. In most cases, crack permeability is much bigger than the intact rock permeability. Thus, knowing the system of the fracture is the most essential part in finding out the fractured rock permeability.

Furthermore, several scholars and researchers, such as Snow (1969) and Stothoff (2000), have developed explicit applied and discrete fracture-matrix models. Furthermore, the dual continuum technique, involving dual porosity and dual permeability, have been established and utilised by Barenblatt et al. (1960). Whilst, Oda (1985) established a crack and permeability tensor technique, which accounts for the volume fraction of the crack set within the entire cracked rock.

2.7 Single-Phase Flow through Natural Fractures

Jones et al. (1988) conducted a study entitled, "Single-Phase Flow through Natural Fractures", and identified that, by relying on the variation between the matrix and crack permeability and

the number of apertures, natural cracks can have a large or little contribution to large reservoir flow characteristics. Flow through a fracture is usually characterised using the equation of classical cubic law (Witherspoon et al., 1980) for a constant-state isothermal laminar flow linking two parallel plates, as shown in Eq. 2.7:

$$Q = 5.11 \times 106 \left[\frac{W \Delta P b^3}{L \mu}\right] \quad 2.7$$

Where,

Q = flow rate (bbl/day)

w = width of fracture face (ft)

ΔP = pressure differential (psi)

b = fracture aperture (in)

L = length of fracture (ft)

μ = fluid viscosity (cp)

2.8 Visualisation of the Channel Flow through a Single Fracture

Mijrata et al. (2002) conducted a study on the "Visualisation of the Channel Flow through a Single Fracture". Fluid flow through a rock mass is important for the understanding of environmental problems, particularly for the geological isolation of nuclear waste and toxic materials. The hazardous substances are carried by the fluid flow through the rock mass matrix. The rock mass is in the upper part of earth's crust where the geological separation is carried out, and includes various assortment scales of fractures. These fractures have a higher permeability than the unbroken parts of the solid rock mass, and this controls the fluid flow through the rock mass. Thus, the characterisation of the fluid flow behaviour through the fractures is one of the major subjects of this study.

Although a fracture surface is coarse and some pieces of its surface touch each other, it was found that the geometry of the contact regions influences flow paths more meaningfully than that anticipated from considering just the nominal area fraction of these contacts. This would

cause the crack permeability to diverge from the local cubic law (Mgaya et al., 2006). Moreover, the fracture permeability is affected by the stress working on the fracture surface. A number of studies have researched these factors to evaluate the fracture permeability more precisely (Barton et al., 1985; Tsang & Witherspoon 1981; Walsh 1981; Witherspoon et al., 1980). These authors concluded that the lengthways roughness on the walls of the fracture plays a certain role in controlling the flow. In the typical parallel-plate representation for a fracture, the flow is relative to the cube of the constant aperture. However, when the effect of the fracture roughness is taken into consideration, the flow follows a comparable 'cubic' law where the cube of the single value for the opening has to be replaced by a suitably weighted average.

2.9 Stress-Strain Relationship

Liao et al. (2009) conducted a study entitled the, "Stress-strain Relationship Based on Strain Space", and stated that the quantity of stress that may be applied prior to the rock failure relies on the rock type and composition, temperature and the time the rock is kept under stress, i.e. the rock generally breaks quicker than if it is underground when stress is applied, as shown in Eq. 2.8.

$$\mathbf{stress(\sigma)} = \frac{\mathbf{force(F)}}{\mathbf{area(A)}} \qquad \mathbf{2.8}$$

Where,

F = force (Newton),

A = area (m^2)

2.10 Young's Modulus and Poisson's Ratio

Takahashi (2012) conducted a study on the "Rock Physics Model for Static Young's Modulus and Compressive Strength of Soft Sedimentary Rocks". As shown in Eq. 2.9, Young's Modulus (E) is the ratio between the stress, σ, and the strain, ε, or the deformation caused by this stress:

$$\mathbf{E} = \frac{\boldsymbol{\sigma}}{\boldsymbol{\varepsilon}} \text{ (psi)} \qquad \mathbf{2.9}$$

Where,

E = Young's Modulus, psi

Figure 2-9 and Eq. 2.10 shows Young's Modulus, which is a stress and strain measurement method. The strain is measured by dividing the increase in length due to applied force to the original length; Young's Modulus is the ratio between stress and strain.

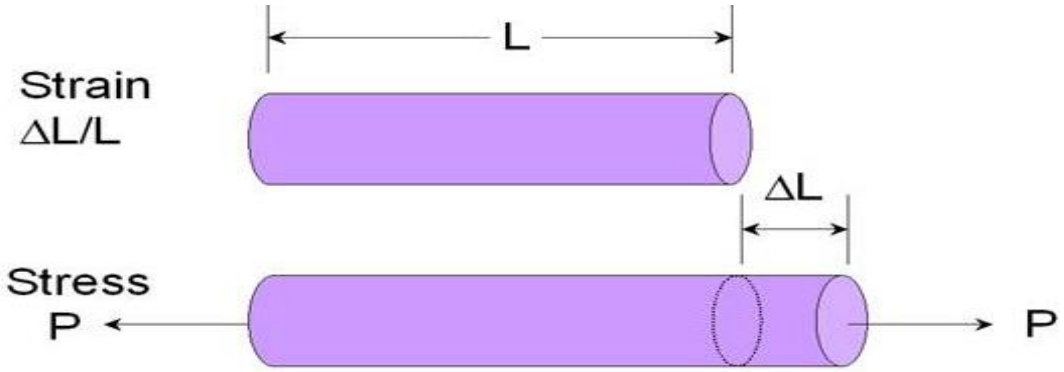

Figure 2-9: Young's Modulus (Takahashi, 2012)

$$\textbf{Young's modulus } (\mathbf{E}) = \frac{\textbf{Stress}}{\textbf{Strain}} = \frac{\mathbf{P}}{\mathbf{\Delta L/L}} = \frac{\mathbf{PL}}{\mathbf{\Delta L}} \text{ (psi)} \qquad \mathbf{2.10}$$

Where,

E = Young's Modulus psi, P = stress or pressure (MPa), ε = strain (no unit) and L = original length (m).

ΔL = elongation length, m

2.11 Relation of Young's Modulus and Poisson's Ratio to Brittleness

Rickman et al. (2008) conducted a study on the "Practical Use of Shale Petrophysics for Stimulation Design Optimisation: All Shale Formation Beds Are Not Clones of the Barnett Shale". Figure 2-10 shows their findings regarding the connection between brittleness, Young's Modulus and Poisson's Ratio.

Brittle shale is prone to natural fracturing and is expected to react well to fracking treatments. There is a requirement to measure the brittleness factor to combine both rock mechanical properties in a shale matrix Wolhart et al., (2005).

In terms of Poisson's Ratio, the lower the value, the extra brittle the rock, and when the values of Young's Modulus increase, the brittleness of the rock increases. As the units of Poisson's Ratio and Young's Modulus are notably dissimilar, the brittleness created by both components is combined, and the average is taken to yield the brittleness coefficient as a percentage.

The idea of rock brittleness unites both Poisson's Ratio and Young's Modulus. These two parts are joined to mirror the rock's ability to fail under stress (Poisson's Ratio) and keep a fracture (Young's Modulus) once the rock is fractured. Thus, ductile shale is not a preferred reservoir as the formation has the tendency to repair any natural or hydraulic fractures. Easily malleable shale, on the other hand, makes a fine seal, preventing the hydrocarbons from moving away to the more brittle shale below.

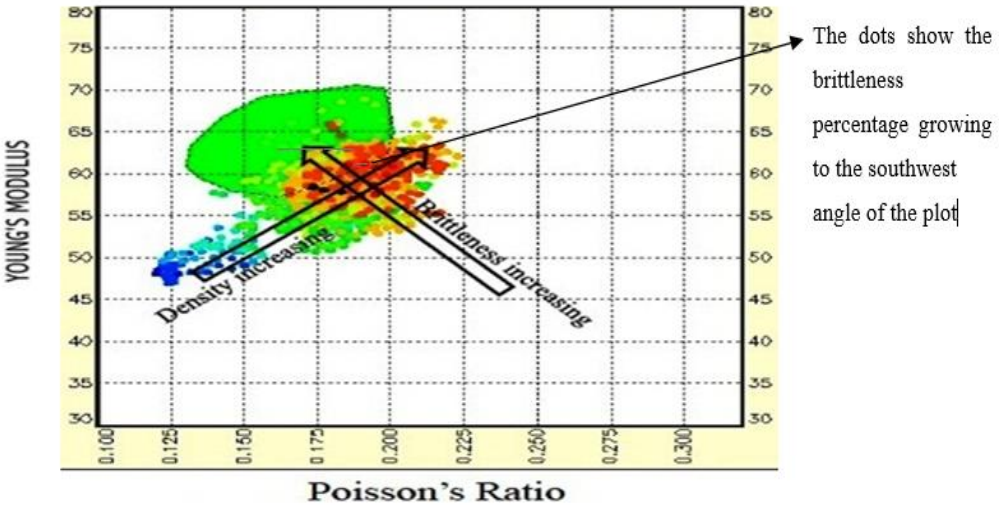

Figure 2-10: Brittleness Young's Modulus and Poisson's Ratio (Rickman et al., 2008)

2.12 Geomechanical Properties of Shale

Reservoir rock properties are identified by core analysis or logging and by the analysis of the production tests. The two techniques, separately and together, are broadly used in reservoir

evaluations. For cracked reservoirs, a difficulty exists in linking the core parameters to the in-situ reservoir properties (Collins and Jordan, 1961).

Potyondy (2007) researched the pore geometry effect and demonstrated that the pores with edges have a greater impact on the simulated material stiffness and strength compared with pores with a rounded shape (Gharahbagh and Fakhimi, 2011). Poisson's Ratio and Young's Modulus are the two major constants used in rock failure models.

Thus, Young's Modulus (the ratio between stress and strain) is used to assess the rock material stiffness, whereas Poisson's Ratio is applied to estimate the simultaneous increase in elongation that corresponds with the thickening of the cross-sectional area inside the elastic range (Al-Anazi et al., 2011; Al-Awad, 2001).

2.12.1 Barnett Shale

A number of shales from various sources are used in this research. To further understand their properties, it is important to identify their chemical composition. The shales used in this work were Barnett, Eagle Ford, Mancos and Marcellus. The permeability was measured for Mancos and Marcellus only, but the characterisation was conducted for the four shale samples (Appendix F shows the Barnett, Eagle Ford, Mancos and Marcellus Shales Chemical Analysis).

The Barnett Shale is a well-known oil/gas supply reservoir and one of the most common shales in North America that has a huge hydrocarbon potential. It is situated in the Fort Worth Reservoir of North Central Texas, which is the main producing natural gas field in the USA, producing around 5.5 billion standard cubic feet per day Bcf/d. Furthermore, it increased its production to 9 trillion cubic feet (Tcf) by the end of the year 2010. It is hard to predict well performance and resources due to geological difficulty; therefore, it is usual to find wells with a similar production interval showing large variances in production quantities (Ezisi et al., 2012).

Due to the local complex nature of the Barnett Reservoir, and considering reservoir formations, it is often hard for petroleum engineers to correctly predict future performance with inevitability

for drilled and undrilled oil/gas well positions (Hall et al., 2010). For example, a well can produce 3 Bcf (billion cubic feet) while a nearby well might produce just 1.3 Bcf.

The Barnett Shale chemical composition, as shown in Figure 2-11, consists of mica, illite, kaolinite, chlinochlore, quartz, microcline and pyrite. The Barnett Shale quartz and mica represent about the same ratio, which is approximately 30%, whereas illite represents about 25%.

Table 2-1: Typical Mineral Abundances for the Barnett Shale (Burner and Smosna, 2011).

Barnett Shale	% Elemental composition
Quartz	35-50
Clays, primarily illite	10-50
Calcite, dolomite, siderite	0-30
Feldspars	7
Pyrite	5
Phosphate, gypsum apatite	Trace

The mineral constituents of these shales contain quartz, feldspar, pyrite, mica, clay and some carbonates with a different wt.%. The clay mineral ratio is contained in kaolinite and illite with few chlorite constituents. The Barnett Shale, shown in Table 2-1, has comparatively high quantities of hardness and bulk density because of its high wt.% of quartz (Aydin, 2009).

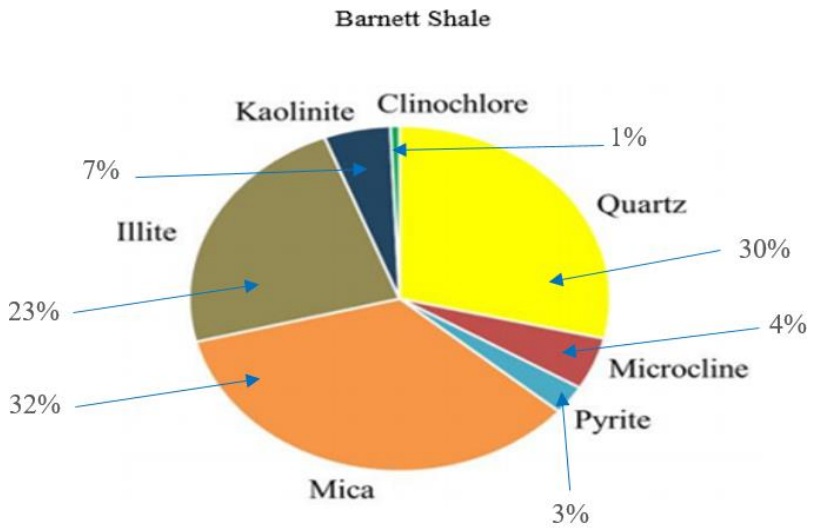

Figure 2-11: Mineral Components of Barnett Shales (Zhi and Ahmad, 2016)

The mineral constituents for Barnett Shale, shown in Table 2-2, are as follows: quartz, 28.7%; clay, 63.6%; feldspar, 4.9%; pyrite, 2.7% and carbonate, 0%. The density is about 2 g/cm3 and the hardness index 434-467 (Aydin, 2009).

Table 2-2: Mineral Composition, Density and Hardness of Shale Samples (Aydin, 2009).

Shale Sample Class	Quartz wt.%	Clay wt.%	Carbonate wt.%	Feldspar wt.%	Pyrite wt.%	Density, g/cm^3	Hardness Index
Barnett	28.7	63.6	0	4.9	2.7	1.932-1.956	434-467

2.12.2 Eagle Ford Shale

The stratigraphy and sedimentary facies of the Eagle Ford Shale (Cretaceous) will be discussed in this section. The key part of the Eagle Ford formations extends along the strike line from the San Marcos Arch in the northeast into the Maverick Reservoir along the border with Mexico. The maximum initial production is in a strike-parallel belt reservoir ward of the Karnes trough and landward of the Cretaceous shelf margin. The three lithologies include the majority of the Eagle Ford Shale in the area: argillaceous shale, calcareous mudrock, and limestone. The mud rocks mostly consist of coccoliths and hold more total organic carbon than the other lithologies

(stratigraphic units). Alterations in thickness and facies inside the Eagle Ford suggest that the area was a topographic high on the sea floor and that alterations in the bathymetry influenced the facies distribution and eventually production from the Eagle Ford Shale (Harbor, 2011; Reed and Ruppel, 2012).

The Eagle Ford Shale is a hydrocarbon-laden formation, situated in Texas State, and an unconventional shale oil and gas reservoir. Eagle Ford Shale is a recent discovery because activities of drilling and completion began around 2009. The key difference between this type of formation and other formations of an equivalent type, for example, Marcellus and Mancos Shales, is its ability to yield gas and liquid hydrocarbons.

Starting from 2008 to the present time, the Eagle Ford Shale Reservoir has been one of the most important established areas. From the first well that was drilled to access the formation, 1,103 wells have been drilled and finalised for production. The Eagle Ford Shale Reservoirs extend from the USA-Mexico border via the south-western part of Texas State. Its geological age (100 million years) matches the Lower Cretaceous, Paleozoic Era. The reservoir depth between the northern and southern parts differs between 6,000 to 15,000 ft and changes in width range from between 300 to 400 ft. However, an essential point for consideration is the high heterogeneity of this formation (Mullen, 2010).

Table 2-3: Presents a summary of reservoir properties from core data analysis (Stegent et al., 2010).

	min	max
TOC, %	2	6
Porosity, %	8	18
Water saturation, %	7	31
Permeability, milliDarcies	0.000001	0.0008
YM, psi	1.00E+06	2.00E+06
Poisson's Ratio	0.25	0.27

2.12.3 Mancos Shale

The Mancos Shale in the San Juan Basin in northwestern New Mexico has become a target of interest as new technologies have unlocked the potential of its unconventional resource petroleum plays, (Broadhead, 2015). The Mancos Shale is an important shale deposit located in the western part of the USA. The Mancos Shale is located in Dakota and intertongues with the Mesaverde Group. It is a carbon-rich form of Cretaceous (around 100 million years ago) shale, with a porosity range of 6-8% and a clay content of about 20-25% (Holt et al., 2012). The rock permeability has been found to be in the range of 10 Nano-Darcy (Sarker and Batzle, 2010).

The mineralogy of Mancos Shale in percentages, shown in Figure 2-13, are: quartz, 43%; calcite, 12%; dolomite, 10.5%; mica/illite, 11.5%; kaolinite, 9%; plagioclase feldspar, 5.5% and other ratios of unnamed elements, 5.5% and 3%. The organic contents are the outcome of both plants and animals' residues inhabiting the area. The high percentage of quartz signifies that the reservoir is highly brittle and frackable.

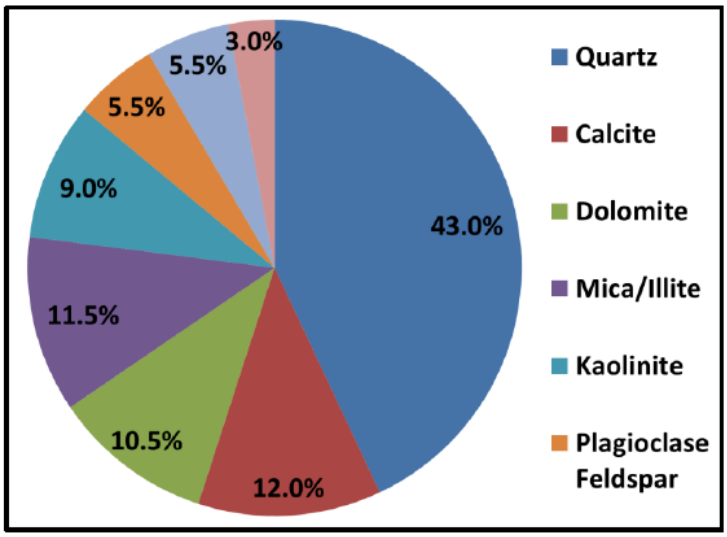

Figure 2-12: Mineralogy of Mancos Shale (outcrop), (Mokhtari et al., 2013).

2.12.4 Marcellus Shale

Zamirian and Ameri (2016) conducted a study entitled, "Measuring Marcellus Shale Petrophysical Properties". Marcellus Shale is a Devonian black, and is part of the Appalachian Basin that starts from New York, continues through Pennsylvania and West Virginia, and extends inside Ohio and Maryland (Bartuska, et al., 2012). It is advantageously situated for the markets in the North-Eastern areas, the Eastern Seaboard, and the Great Lakes region of the USA. Found 4,500 ft to 8,500 ft deep in the formation, natural gas is produced most proficiently using advanced horizontal drilling techniques in combination with fracking enhancement treatments. Despite advances in technology, the emergence of the very-low permeability structures in Marcellus Shale has created fresh challenges for the expansion of the resource.

Soeder (1988) conducted a study on "Porosity and Permeability of Eastern Devonian Gas Shale" for which high-accuracy core analysis was carried out for eight gas shale samples from the Devonian basin. The samples consist of the Middle Devonian Age Marcellus Shale in Morgantown, West Virginia. Porosity and permeability values were evaluated on eight shale cores from Devonian, and are tabulated in Table 2-3. The gas utilised in this measurement for these core samples was nitrogen. Different samples, shown in Table 2-3, were taken and

analysed from Huron and Marcellus formations at different depths, which gave the following data on the net stress, porosity to gas and permeability.

Table 2-4: Devonian Shale Core Sample Analysis Results (Soeder, 1988).

Sample	Formation	Depth (ft)	Net Stress (psi)	Porosity of gas (%)	Permeability μD
EGSP-WV-5 Mason County	Huron shale	3,028	1,750 3,000	<0.10 <0.10	0.066 0.014
More no 1(KY) Leslie County	Huron shale	2,904	1,750 3,000	0.12 <0.10	0.022 0.005
EGSP OH-6/4 Gallia County	Huron shale	2,771	1,750 3,000	<0.10 <0.10	6.80 4.50
EGSP OH-9 Megs County	Huron shale	3.245	1,750 3,000	0.15 <0.10	0.001 0.0002
EGSP WV-6 Monongalia County	Marcellus	7.448.5	3000 6,000	9.28 8.67	19.613 5.909
EGSP OH-6/4* Gallia County	Huron shale	2,770.8	1.750 3,000	<0.10 <0.10	8.342 5.489
EGSP OH-6/5 Gallia County	Huron shale	2,441.4	1.750 3,000	0.18 <0.10	0.248 0.008
EGSP OH-8 Noble County	Huron shale	3,325	1.750 3,000	<0.10 <0.10	0.194 0.078

Different samples were taken from Barnett, Eagle Ford and Marcellus Shale formations, which were analysed and gave the following data of the kerogen and porosity, as demonstrated in

Table 2-4. Barnett Shale produced the maximum kerogen ratio, then Marcellus whilst Eagle Ford produced the lowest ratio. In comparison, porosity was at a maximum for Barnett, then Eagle Ford and finally Marcellus. More kerogen content contains higher oil and gas ratios but there is no relationship between porosity and permeability or oil production; sometimes there is porosity but the permeability is low. The presence of organic matter in shales increases porosity because most pores in shales are placed in organic matter (Ambrose et al., 2010).

Table 2-5: Estimated % Kerogen by Volume and Porosity for Barnett, Eagle Ford and Marcellus (Soeder, 1988).

Sample	Kerogen (Vol.) %	Porosity %
Barnett	5.3	2.3
Eagle Ford	2.4	0.4
Marcellus	5.0	0.2

Figure 2-13 shows a Barnett sample under back-scattered electron (BSE) images of 9 different gas shale formation samples prepared in a cross-section with Focused Ion Beam (FIB) milling. The bedding planes are perpendicular to the images and the horizontal field represents 5.12 micrometre. Most of the samples are seen to contain dispersed kerogen, whilst the very bright material is pyrite. Note that in most images, the kerogen is porous with darker holes.

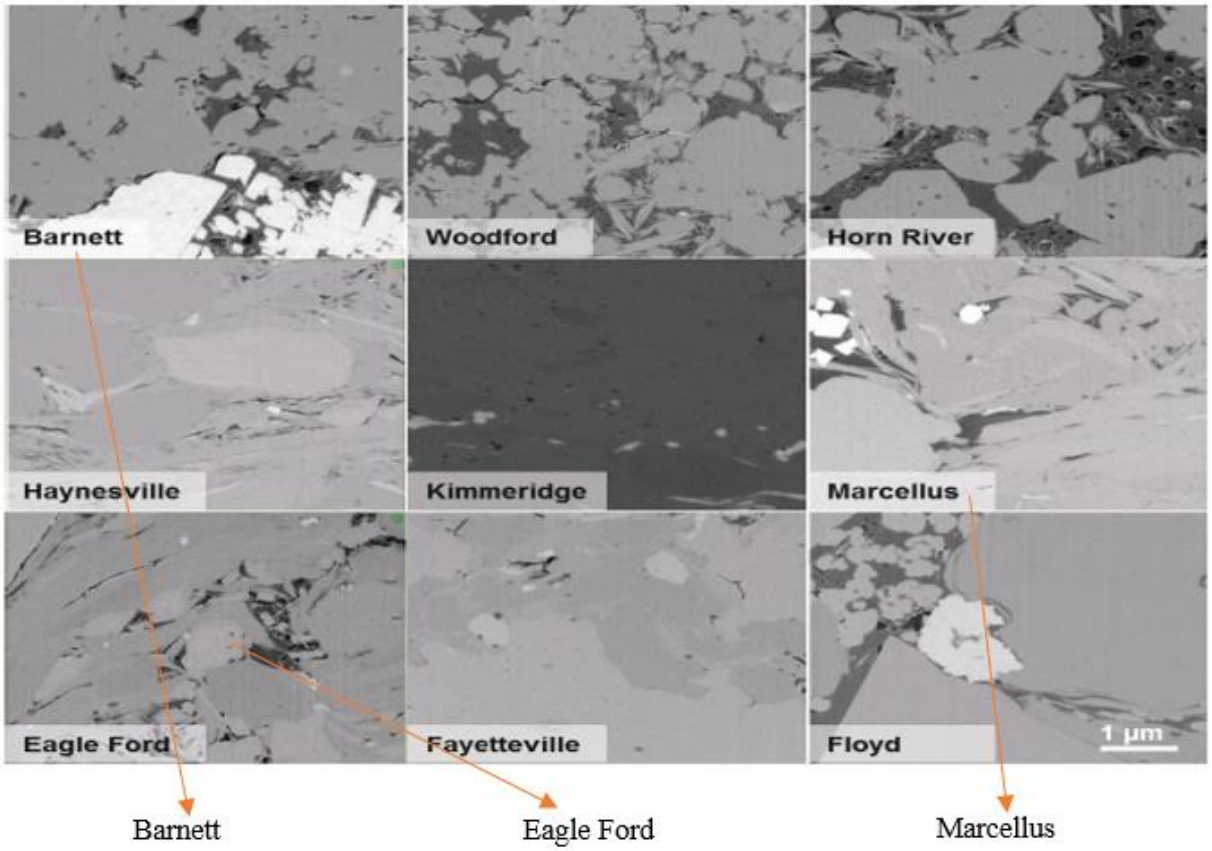

Figure 2-13: Barnett Sample under Back-Scattered Electrons (BSE) Images of the 9 Different Shales Sampled Prepared in Cross-Section with Focused Ion Beam (FIB). Horizontal Field Width in All Images is Identical, (Zamirian and Ameri, 2016).

In terms of the mineralogical constituents, as shown in Table 2-6 from the x-ray diffraction (XRD) analysis, Marcellus Shales are rich in calcite at 75.14%; they contain a small quantity of clay (illite) at 12.94%, quartz at 9.74% and pyrites at 3.18%. The composition demonstrates that the shale is brittle because of the higher ratio of calcite within the formation (Ding et al., 2011). These outcomes disclosed uniformity with the published figures of XRD analysis on the analogous outcrop shale samples (Lora, 2015). The ratio of quartz is very low so the fracability is too low for Marcellus Shale.

Table 2-6: Mineralogy of Marcellus Shale (Lora, 2015).

Whole Rock Mineralogy (Weight %)	
Calcite	75.14
Illite	12.94
Quartz	8.74
pyrites	3.18

2.13 Fracturing Technology

Hydraulic fracturing is the process of injecting high-pressure fluids (sometimes as high as 10 k psi) into rocks to fracture them. These artificial or human-made fractures are kept open by proppants, for example, sand or ceramic particles. Hydraulic cracks may be created naturally when pressurised fluids escape upward from deep reservoirs and fracture rocks in their way. Fracking causes the pores in mudstones to become interconnected and, because of this, the oil and gas flow out through the rock and towards the well (Collins and Jordan, 1961).

This research demonstrates complex fractures at different angles for Mancos and Marcellus Shale samples tested at 100, 150 and 200 bar overburden pressures. However, previous researchers have overlooked the complex fracture orientations. A complex fracture is a varied fracturing technique, where fractures occur at different orientation angles and locations within a sample, which facilitates the flow of oil and gas through multiple channels to the borehole and thus recovers oil and gas production.

While unconventional oil reservoirs may be enhanced by hydraulic fracturing, reservoirs that predominantly consist of clay sediment size of <62.5 µm and at most < 2 µm might not be possible to fracture. This is because, after reservoirs are fractured, the clay deposits of the size 62.5 µm, turn back into mudstones again due to compaction and chemical alterations through the burial diagenesis process (Aplin and McQuaker, 2011).

In the field, conventional techniques are used to determine in-situ stress, for example, overcoring and hydraulic fracturing, but these methods include many limits and economic downsides (Bock and Foruria, 1984). In-situ stresses can vary from point to point in a rock mass and are volume dependent. However, it is not always likely to produce a definite mathematical formula/relationship between stresses and depth, which is usually wanted by the designer, (Kumar et al., 2004).

In a comparatively small volume of rock, for example, $1m^3$, stresses may vary notably over a small distance. This can be due to discontinuities in geological structures and variations in the rock properties of a mass of natural rock. Therefore, conflicting results may be obtained if reduced measurements are undertaken or are performed at dissimilar sites. Therefore, the complex nature of rock structures can make the interpretation of well logs tricky and often useless. Moreover, severe borehole conditions repeatedly prevent the application of geophysical well logs (Laudeman and Ershaghi, 1981).

2.14 Geomechanical Models to Compare the Productivity of Shale Reservoirs Using Different Fracture Techniques.

Safari et al. (2013) conducted a study entitled “Integrating Reservoir and Geomechanical Models to Compare the Productivity of Shale Reservoirs Using Different Fracture Techniques”. The research involved the application of a pressure load with a ductile-brittle transition that would be set off with a number of fractures spreading out from the borehole. The fracturing load was applied over a period of milliseconds to initiate and lengthen multiple fractures laterally from the borehole.

The downsides of the hydraulic fracturing method were that 20 to 30% of the water used in the process was lost in the formation when cleaning up, which sheds doubt over the fracture efficiency and highlights the possibility of damaging the fracture sand face.

2.15 3D Analysis and Engineering Design of Pulsed Fracturing in Shale Gas Reservoirs

Pulsed Gas Fracturing, which is used to tailor the pressure-time performance of a pulse source to initiate several fractures and avoid natural limits in hydraulic and explosive fracturing techniques, has been overlooked. In this technique, a dynamic pulse is triggered in the order of milliseconds to initiate and spread multiple cracks that radially start at the holebore as ductile to brittle alteration is prompted (Kutter and Fairhurst, 1971; Nilson et al., 1985). This could represent the best fracturing technique in the future, as this makes the clean-up operation easier and quicker. This type of technique is just an alternative fracturing method; the outcomes demonstrate that, if planned precisely, pulsed fracturing might help prompt a ductile to brittle change and may initiate complex fracture networks. Pulsed fracturing makes a burden approximately an order of scale above the in-situ stress degree, but could remain underneath the elastic limit of the rock (Coates, 1967; Safari et al., 2013).

Safari et al. (2014) conducted a study entitled, "3D Analysis and Engineering Design of Pulsed Fracturing in Shale Gas Reservoirs". The work considered the ability to make complex linked fracture networks, which might remain unlocked throughout production. It is important to increase permeability to enhance the extraction of oil and gas from shale oil and gas layers/beds. In the time and pressure extent of the fracking processes, it is not easy to create crack complexity in a ductile shale, although, while subjected to a high pulse loading, the rock may show a brittle to ductile change and a complex crack network could be initiated.

The main concern is that, in a deep shale reservoir it may not be possible to fracture efficiently because the formation could heal/close/repair itself thereby cancelling the fractures. As an outcome, it is important to find alternative fracturing methods that might:

- Make extensive and open fracture networks,
- Reduce the use of slickwater (fluids) and as well proppants, and,
- Make the most of the recovery and productivity of oil and gas (Gandossi, 2013; Safari et al., 2013).

The majority of the field observations propose that rock will tend to fracture if its Young's Modulus is high and its Poisson's Ratio is low. The idea of pulsed fracturing is to tailor the

pressure-time performance of a pulse source to make multiple cracks and avoid limits innate in both hydraulic and explosive fracturing. Hydraulic cracks characteristically yield individual single cracks aligned with the maximum principal in-situ stress orientation/direction.

There are various pulse sources that may be utilised, for example, propellant burning, electric pulses, and plasma tools, to initiate stress waves inside the formation rock matrix. The propellant pulse source releases a high-energy gas pulse with deflagration. The resulting crack patterns from a pulsed cracking operation are shown in Figure 2-14. This Figure shows the multiple fractures that propagate when the pulsed fracture is set off. The forking and slip along externally propagating cracks might induce a self-propping system, as demonstrated in Figure 2-14.

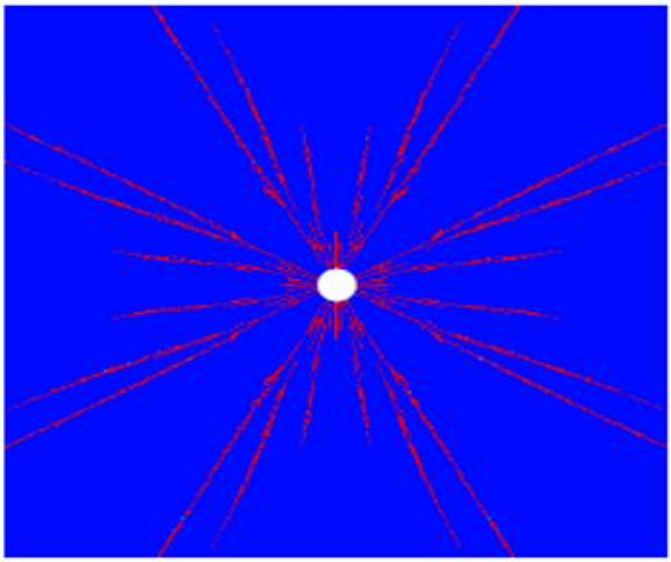

Figure 2-14: Branching as Observed from a Pulsed Fracturing (Kutter and Fairhurst, 1971: Nilson et al., 1985).

2.16 Engineering design of pulsed fracturing

Following the application of the pulse-rise interval, which triggers multiple radiated cracks, many post-peak scenarios may be followed. The initial scenario is to apply a pulse source, which gives a bigger decay time and non-stop gas penetration, while post-peak, as illustrated in Figure 2-15, may be attained by successively using many or multi propellants. The second scenario

includes a comparatively fast gas outflow into the made primary fractures, which is illustrated in Figure 2-15. The third scenario entails the pumping of gas at an additional reduced rate and for a long amount of time into a previously made crack network. Any of the aforementioned scenarios may lead to dissimilar fracture network designs.

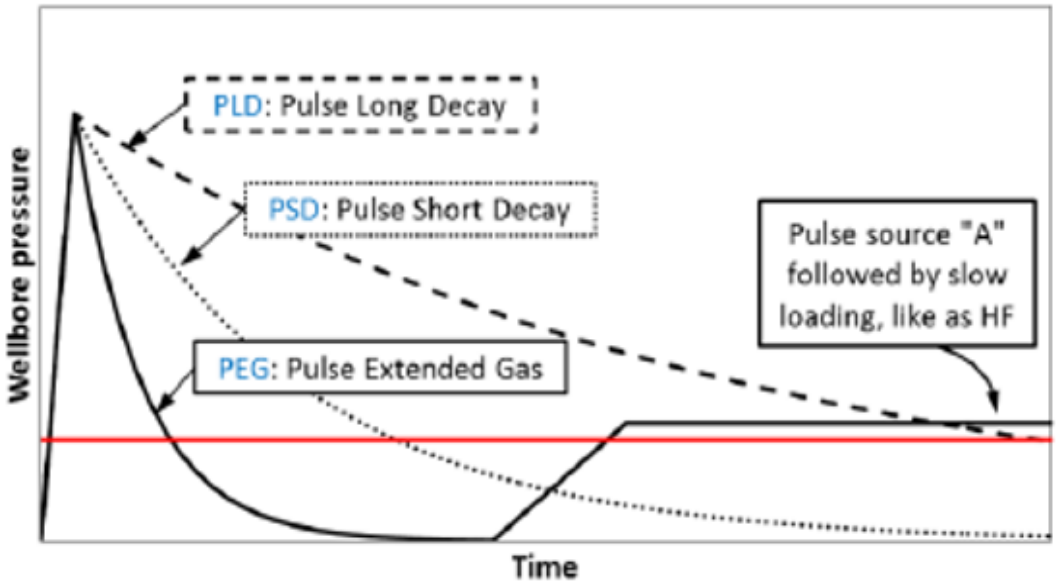

Figure 2-15: Different Scenarios for Pulse Pressure Profile (Kutter and Fairhurst, 1971; Nilson et al., 1985).

The application of high-energy gas and pulses would limit proppant transportation that might assist and maintain crack conductivity inside the network. Thus, the potential issue of crack conductivity maintenance with no proppant, under high-closure stresses is of maximum importance while pulsed cracking is applied. Nevertheless, practical observations of channelling, advocate that a slip along newly-made coarse surfaces could initiate a self-propping system, as shown in Figure 2-16.

The use of high-energy gas and pulses can limit proppant transportation, which can help to maintain crack conductivity inside the network. Therefore, as previously suggested, the possible issue of the maintenance of crack conductivity with no proppant under high-closure stresses is of maximum importance while pulsed cracking is applied. However, practical observations of

channelling, advocate that a slip lengthwise against coarse surfaces can trigger a self-propping system.

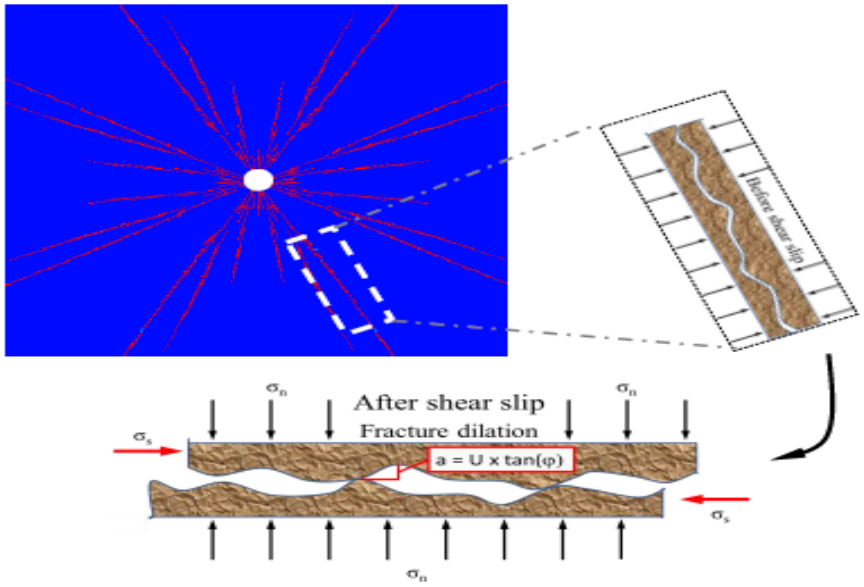

Figure 2-16: Slip/Dilation Potential along Asperities that Promote Misalignment and Self-Propping under in-situ Stress Field (Kutter and Fairhurst, 1971; Nilson et al., 1985).

2.17 Chapter Summary

This chapter has detailed unconventional reservoirs, the composition of shale, the geomechanical properties of shale, and how this helps in enhancing the oil/gas recovery of unconventional reservoirs. Fracking technology and the effect of fracking orientation on permeability have also been detailed. A number of authors have studied shale fracture orientation and its effect on reservoir permeability, but they have only addressed basic fractures. The author of this research dealt with complex and multiple complex fractures with the aim of increasing the permeability of tight shale reservoirs and thereby increasing the production of oil and gas.

It has been noted that there has been limited work on the effects of complex fractures on permeability covering varying shale types. Therefore, this is the area on which the research will concentrate.

The main findings of the chapter are:

- Shale rock is formed of clay minerals 55.2%, quartz 23.9%, carbonate 9.3%, feldspar 6.1%, organic matter 4.2%, Fe-oxides 0.8%, other minerals 0.5%.
- The porosity of unconventional reservoirs is not all interconnected, which renders them with very ultra-low permeability. Pore geometry and mineral components, and the TOC and maturity of organic matter show that depositional environment, diagenesis, and the thermal evolution of organic matter control the formation and conservation of pores. Shales with a high TOC have ultra-low porosity because a high organic content causes high hydrocarbon production. Organic pores were closed because of the compaction after the hydrocarbon generated was expelled (Er et al., 2016).
- Shales contain many small pores and hold natural gas or oil or both.
- Geomechanics can cause different fracture orientations, which influence the production rate when a well is drilled.
- The compressibility of rock is dependent on the mineral rigidity present in the rock, i.e. rigid minerals render the rock smaller in compressibility value.
- Many researchers agree that the behaviour of the non-Darcy flow is caused by a turbulent flow because of the high velocity and the inertia force due to the lithology and tortuosity.
- Rock matrix is a quasi-brittle material that includes flaws, pores, and micro-cracks. The existence of pores involves a substantial effect on the rock engineering properties; for instance, uniaxial tensile strength, uniaxial compressive strength and stress of crack initiation.
- Permeability within a fractured porous media is mostly controlled by the geometry, the interconnection of the pores and some fractures, and by the stress state.
- The two components of Poisson's Ratio and Young's Modulus work together to mirror the ability of a rock to fracture when a stress is available. They keep the fracture open when the rock fails under stress.

Chapter 3: Experimental Apparatus and Method of Data Collection

3.1 Chapter Overview

This chapter describes how the shale samples from the Barnett, Eagle Ford, Mancos and Marcellus Reservoirs were processed, and the experimental setup (Nano-Perm) and procedure for a range of equipment used to investigate the effects of complex crack orientation on permeability. The chapter covers:

- Sample preparation.
- The chemical composition of the shale samples.
- Crack and porosity data using the Computerised Tomography (CT) scan.
- Operation of the Nano-Perm machine used to obtain the permeability of the second set of the shale samples (Marcellus) over a range of overburden pressures 34.5, 69. 103.5 and 138 bar. The permeability of Mancos and Marcellus (third set of shale samples) measured at overburden pressures of 100, 150 and 200 bar.

3.2 Flow Chart

The flow chart, shown in Figure 3-1 highlights the experimental work that was undertaken, starting with the preparation of the shale samples collected from Barnett, Eagle Ford, Mancos and Marcellus Reservoirs. The samples were initially analysed for their chemical composition using an XRF spectrometer. The pore volume for the second set of shale samples (Marcellus) was then calculated using the liquid saturation method which involved finding the difference in weight between the dry and wet samples and, by knowing the density of the brine, the pore volume can be calculated. This value of porosity was compared with porosity measured using the CT scan, as shown in Table 4-7.

The second set of shale samples (Marcellus), shown in Figure 3-2 and Table 3-1, was then induced with complex fractures using a powered-hack saw. The CT was used to determine the crack width and crack length and to analyse the samples for any natural cracks. The Nano-perm

machine was then used to determine the permeability of the second set of shale samples (Marcellus) for the following range of overburden pressures: 34.5, 69, 103.5 and 138 bar. These overburden pressures generally represent the well depths of the shale reservoirs mentioned in this research. It was noted in the literature that every 207 bar of overburden matches around 152.4 m burial depth of a typically compressed reservoir (Fatt and Davis, 1952).

Permeability was also measured for the third set of shale samples (Mancos and Marcellus) at overburden pressures of 100, 150 and 200 bar.

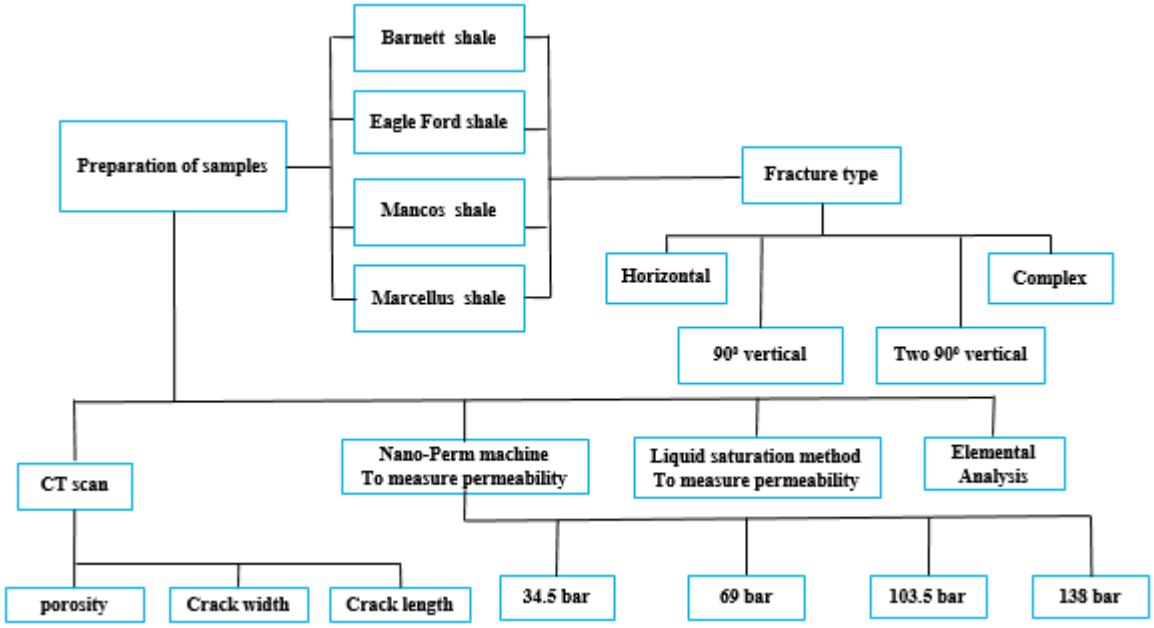

Figure 3-1: Flow Chart of Method and Data Collection

3.3 Geomechanical Properties of Shale

Many authors trying to understand the physics of the flow and to ultimately enhance productivity have investigated the geomechanics of shale rock. This research aimed to investigate the geomechanical properties, such as the permeability and porosity of the shale reservoirs, through testing shale core samples of different fracture orientations to further develop an understanding of these properties on permeability. The study also investigated how permeability is affected by fracture orientation relative to the bedding plane under varying

overburden pressures. Thus, the geomechanical properties of six shale samples from Marcellus were fractured at different angles of orientation, as shown in Table 3-1.

3.4 Preparation of the Samples

The Marcellus Shale samples were fractured using a powered-hack saw, each to the required fracture orientation, as shown in Figure 3-2 and defined in Table 3-1. These were as follows: unfractured (1), 90^0 vertical fractured (2), two - 90^0 vertical fractured (3), horizontal fractured (4), triangle complex fractured (5), and line complex fractured (6).

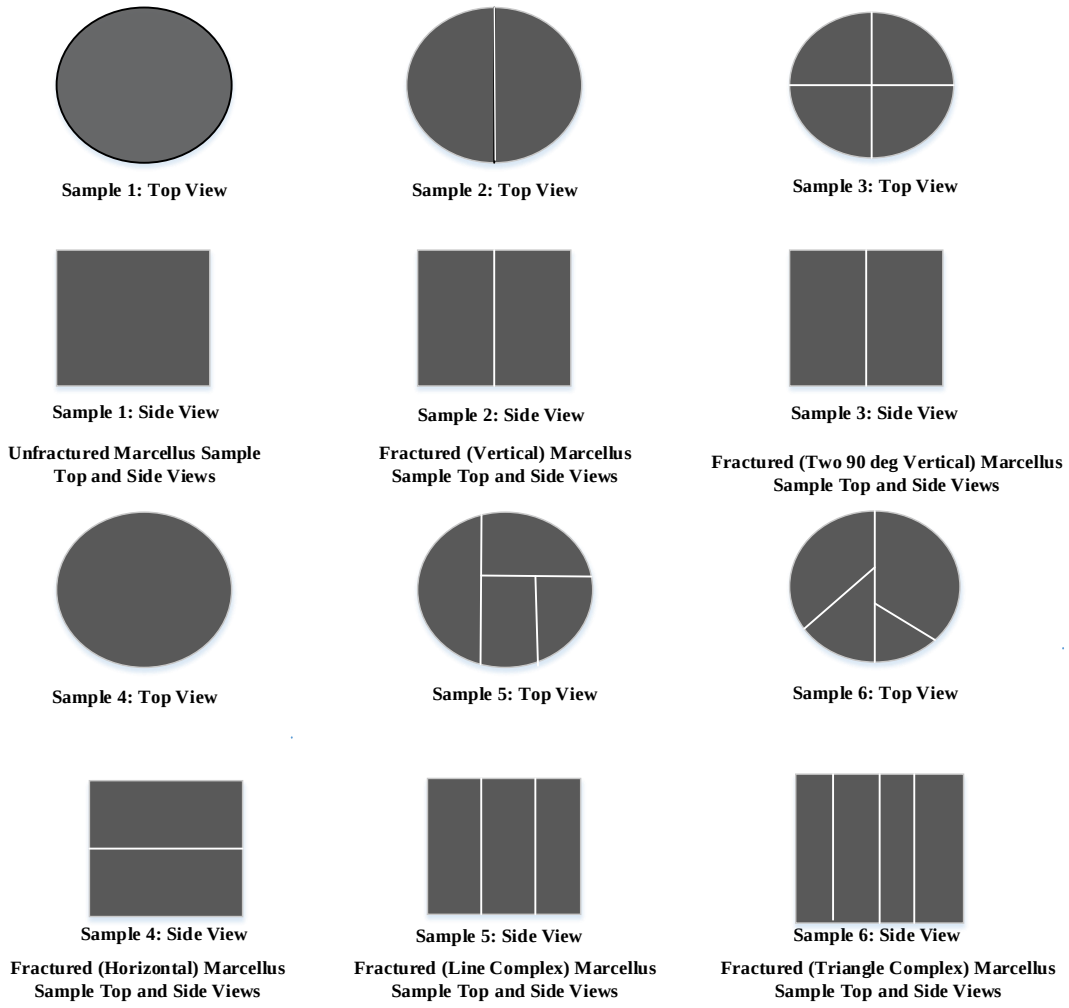

Figure 3-2: No Fracture and Different Fracture Orientations of Marcellus Shale Samples

Table 3-1: Shale Samples Preparing and Fracturing.

Samples	Fracture type	Sample Size. mm	Preparation: cutting and lapping	See Figure in Appendix B
Sample 1	Natural	6.35 (L) * 37.44 (D)	The six shale samples from Marcellus Reservoirs were prepared by fracturing them using a powered-hack saw, each to the required fracture orientation. The fractured samples were then lapped to make their surfaces match and encased in a plastic sleeve which was then heated to form a shrink-wrapped seal.	B1
Sample 2	90^0 vertical	27.74 (L) * 37.44 (D)		B2
Sample 3	Two 90^0 vertical	27.74 (L) * 37.44 (D)		B3
Sample 4	Horizontal	27.74 (L) * 37.44 (D)		B4
Sample 5	Triangle complex	13.4 (L) * 37.44 (D)		B5
Sample 6	Line complex	13.4 (L) * 37.44 (D)		B6

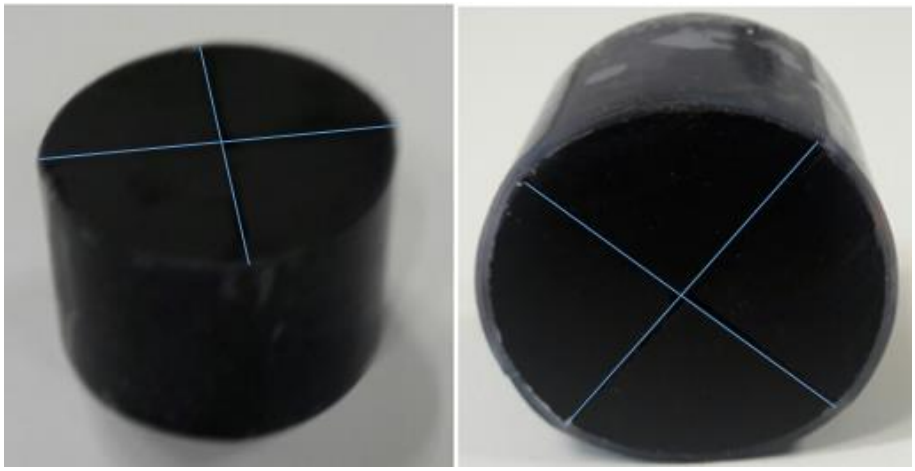

Figure 3-3: Two 90-degree Vertical Marcellus Shale Sample

3.5 CT scan

The Computerised Tomography (CT) scan technique is based on the attenuation of the x-ray beams penetrating the scanned object at different angles as the sample is rotated in front of the

x-ray source and a detector records the transmitted x-ray intensity data. From these projections, a cross-sectional slice is generated through the core via a computerised reconstruction process. A three-dimensional image can then be reconstructed from the cross-sectional slices taken from the sample. CT scans were used to establish whether there were any pre-existing fractures in the unfractured core that may affect permeability, and then to determine the crack length and width of the induced fractures of the fractured samples. There were no pre-existing fractures.

3.6 Equipment Description and Principle

The CT scanner (manufacturer: GE Sensing & Inspection Technologies phoenix |x-ray and model: V|tome|x s 240) used data optimisation and reconstruction software. The x-rays produced by the machine have wavelengths in the range of 0.01-10 nm. The x-ray machine shown in Figure 3-4, contained two x-ray tubes, the microfocus and the nanofocus (x-ray spot size down to 100 nm). These are used to deal with the different sample sizes; for example, the nanofocus is for small-size samples (smaller than 2 pence coin) and the microfocus is for normal-size samples, which can be the same or a larger size than a 2 pence coin.

The CT scanner consists of a sliding door, which is used to access the CT scan chamber and sample manipulator and x-ray tube enclosure, the monitor adjusts and controls the scanning process and control console to control the sample position. In addition, there is a desktop computer for the reconstruction and to post-process the scanned work.

The first set of shale samples (Mancos, Eagle Ford and Marcellus) 152.4 mm (L) by 50.8 mm (D) were scanned using the microfocus tube, and, from the scan results, the core samples' porosities were determined through the module defect analysis software, Volume Graphic (VG) analysis. In the 3D volume, grain structures, layering and fractures in 3D can be studied.

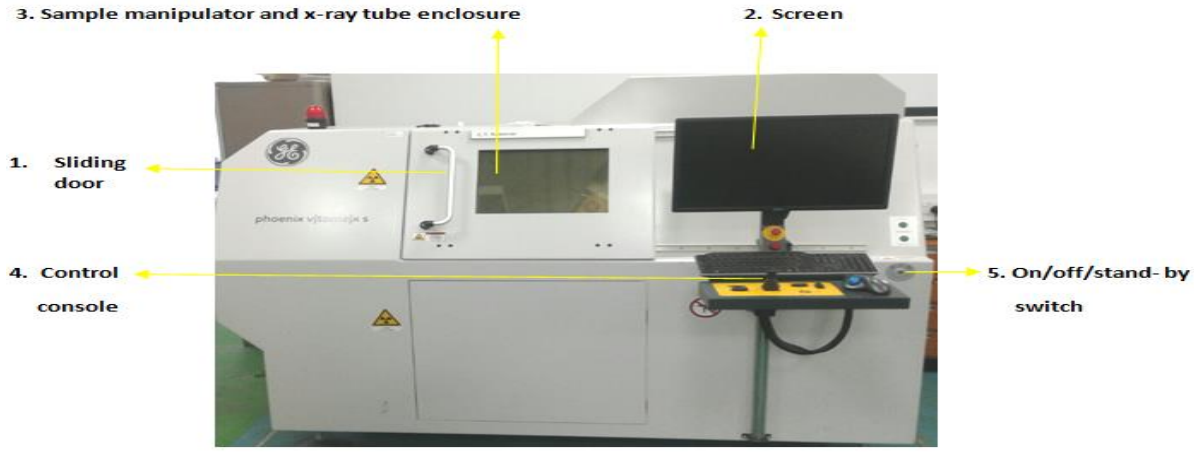

Figure 3-4: Micro-CT Scanner at Petroleum Lab, the University of Salford

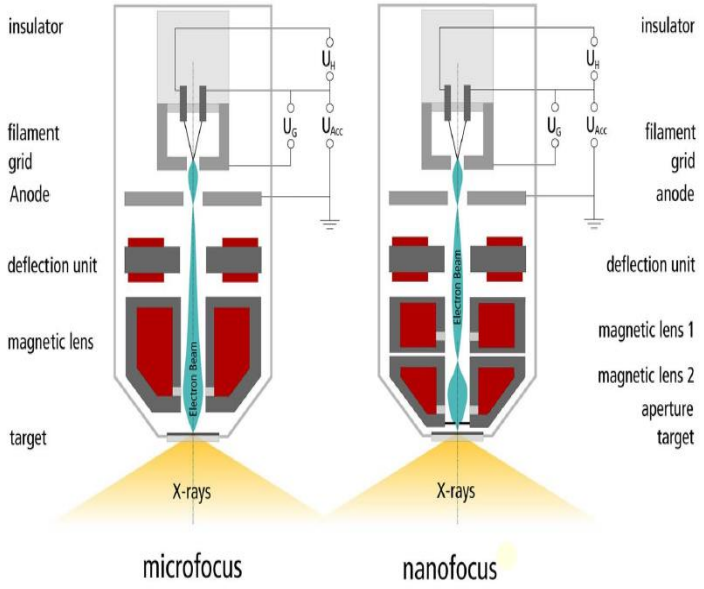

Figure 3-5: Microfocus - Nano Focus (from a CT Scan Manual)

The tubes, shown in Figure 3-5, consist of a deflection unit and target insulator, filament grid, anode and magnetic lens.

3.7 CT Scan Principles and Applications

Over several decades, x-ray Computerised Tomography (CT) has gained wide acceptance as a routine analysis tool. In the oil industry, the cost of utilising a CT scan for rock characterisation

is small in comparison to the overall project value and can improve the probability of reaching the upper end of an NPV (net present value) range. Efforts in support of the more widespread use of CT scanning to investigate field-related problems, such as formation damage solutions and improved perforations, may offer improvements in the recovery of problematic oil and gas wells. CT scanners have been in use in the petroleum industry for 30 years or more as an effective tool for studying basin rocks (Siddiqui and Khamees, 2004).

3.8 CT scan Setup

The CT scan setup consisted of a number of stages:

Stage One: CT scan setup, which is performed in the following steps:

i. Create a new project.
ii. Mount sample, under a tilt, to avoid Feldkamp issues (avoid sample planes parallel in the cone beam.).
iii. Switch x-ray ON (i.e. 100kV / 100μA, lowest timing, Sensitivity = 1) and press Live-Image.
iv. Drive CNC Coordinates X = 0 mm and select the CT Sample ROI (Region Of Interest).
v. Adjust x-ray parameter, timing, and filter.
vi. Select the average number of projections, random detector movement.
vii. Auto scan|optimiser and write-in filter type + thickness.
viii. If the background is inhomogeneous, create a new offset and gain correction.
ix. Define the observations area.
x. Start CT (stepping, fast|scan or auto|ct).

After completing a CT scan, the x-ray images were compiled into a quality 3D view of the interior of the scanned specimen. This process is known as reconstruction, and the most important parameter in the process is called the image centre of rotation. The process of reconstruction is essentially an overlaying procedure, where the individual x-ray images are aligned and laid on top of each other to form the final image.

Stage Two: The reconstruction of CT scan was performed undertaking the following steps:

i. Start datos|x reconstruction and load the PCA-file.
ii. Use the agc or scan|optimiser for geometry correction.
iii. Use bhc correction.
iv. Set 0° rotation and define a min. ROI (Region Of Interest) for reconstruction.
v. Start CT reconstruction.

Stage Three: Post-processing of the data, which refers to the use of filters on the existing volume. When filtering starts, the filter type and filter size are chosen and the filter volume is clicked. These filters available are:

- *Median*: low-pass filter, which is particularly useful for reducing noise with minimal edge blurring.
- *Gauss:* reduces the noise in the volume, and reduces the size of outer radii after surface extraction.

The parameters, shown in Table 3-2, are typical of those used when performing the CT scan. The number of images was typically 1000 or more and the skip was set to 0. If the skip is 1 and the images required are 1000, the CT scan will produce 1000 + 1 image, with a timing of 333 seconds. Sensitivity was set to between 0.5 and 4, whereas current in μA and voltage in kV is equal or larger than 80.

Table 3-2: CT Scan Parameters and their Values

Parameters	Values
Average	2
Number of images	1400
Sensitivity	2.000
Size	1000
Skip	0
Timing	333
Current, μA	≥ 80
Voltage, kV	≥ 80

The energy of the x-ray has to be decided by tuning the voltage. A value of 80kV is sufficient to penetrate the minerals and makes a good contrast between the void and solid. The resultant current is around 80μA.

A series of detectors record the transmitted x-ray intensity data. From these projections, a cross-sectional slice is generated through the core via a computerised reconstruction. A three-dimensional image can be reconstructed from the cross-sectional slices taken from the sample. The main factors that limit the resolution of a conventional CT include the x-ray tube beam size, the detector array, and the broad energy spectrum of the x-ray beam.

3.9 Image Segmentation

The common practice in geological fields is to employ thresholding techniques to segment such images by applying a visually interpreted threshold or image processing approach. A summary of the parameters was undertaken to obtain x-ray attenuation profiles. The detailed procedures for a synchrotron micro-CT Scan are as follows:

First, the energy of x-ray must be decided by tuning the voltage. A value of 90 kV is sufficient to penetrate the minerals and ensure a good contrast between the void and solid. The resultant current is around 100 μA. Then, the correction images must be acquired to remove inhomogeneity in the background images, i.e. images with only air between the source and detector. Two such images are required, one with the x-rays on and one with the x-rays off (also called the flat and dark field in the synchrotron micro-CT). The flat field is necessary to account for the non-uniformities in the x-ray beam and the non-uniform response of the detector.

A section of the sample was segmented and used for the image extraction and volume analysis. After segmentation, the image was extracted and a 3D visualisation of the extracted geometry of the processed CT scans of the shale sample was produced. The porosity of the scanned samples was then determined using the Volume Graphics (VG) Software. The shale core samples scanned were Mancos and Marcellus.

3.10 Reconstruction

Reconstructing a CT scan produces a representation of the interior features of an object. A regular single x-ray image can also show the same features, but accurate locations of interior features cannot be determined from a single view. The CT process uses x-ray images from many different views through a thin section of an object to pinpoint the locations of the internal features. When the scan is reconstructed, the resulting image is a cross-sectional view of the object as if it had been cut through the plane at the scan location.

3.11 Post-Processing Scan Data

3.11.1 Introduction

During the post-processing stage, a number of analyses covered porosity (shown in Tables 4-6 and 4-7 and Figures 4-6 and 4-7) and crack width; furthermore, crack length measurements were also undertaken (Table 4-5). Image analysis was also undertaken for the Marcellus Shale. This includes voxel discretisation, reconstruction and surface determination. Porosity can be

calculated from the CT image with a single scan of a core sample by detecting the pore space by image segmentation techniques.

Segmentation is the first treatment applied to CT images before analysing the physical characterisation. It consists of the pore spaces extraction in each scale corresponding to the CT image resolution. In addition, three-dimensional CT scans may provide interesting qualitative views of the interior structure of shale samples. Using a CT scan, the core sample porosity can be calculated using the model defect analysis, Volume Graphics or VG.

3.11.2 Porosity Estimation by CT scan

Porosity can be calculated from the Computerised Tomography (CT) image with a single scan of a core sample; this is achieved by detecting the pore space through image segmentation techniques. By using a CT scan, the core sample porosity can be calculated using the model defect analysis, Volume Graphics (VG).

3.11.3 Calculating Porosity Using CT scan

The porosity of the samples was obtained using the post-processing software and by undertaking the following steps:

i. Adjust the square and click each angle to make sure that the sample is within the frames at different angles.
ii. Click scan/optimiser, Compute, Apply, Yes and Accept.
iii. Click auto/ROI, activate the 3 items, start and Yes.
iv. Minimise the square and play with angles to be sure that the sample remains inside the rectangle and click Start, Save and Yes.
v. Click in the right lower quarter to make the square appears.
vi. Click volume analysis, zoom in or zoom out to size the shapes.
vii. Click surface determination, Automatic and adjust the red line to get the best array of grains and click Finish.

viii. Rotate the sample and adjust the red line to get the clear view of grains and put the axes by clicking the Tripod and choose Show Box.

ix. Click 'Define material by example area', move the small rectangle aside, select area using a mouse and click next.

x. Select an example region in a slice view below using the mouse to define the material and click finish two times.

xi. Click New Detection, choose the default (v 2.1), voids, activate Show Preview and click 'Use determined Surface'.

xii. Put a value of 3 for Probability threshold and see the result (a big number of probability gives a small number of porosity and vice versa), and always put the maximum size = 0.05; for example, if you get a small value of porosity, decrease the value of the probability and adjust the probability until you get an acceptable value.

xiii. Click Calculate.

xiv. Wait until the porosity has been calculated and then click 'Add colour coding'.

3.11.4 Measuring Crack Width and Crack Length Using CT scan

The following steps were undertaken to determine the crack width and crack length:

i. Select, Selection Modes and then Ellipse.

ii. Press the left button of the mouse and drag over the shape to be restarted, resize using the red crosses.

iii. Extend the redline in the first right quarter to cover the area.

iv. To create a region of interest, click first R sign on the left top corner and go to region 1 of interest on the right side of the computer under the grey box (right click) and go to enable ROI to render settings.

v. Click on the grey button (next light source 2) and click transparency and input zero and enter. Any analysis should be done when the region 1 is highlighted.

vi. Go to the selection modes and choose 'adaptive line' to draw a line using the left button of the mouse from side to side.

vii. Extend the line in the top left corner to cover the whole circle then click R in the left top corner (first R) to create a region of interest, and wait for the calculation.

viii. To measure the length of the line, click the instrument and choose the polyline length, if the line is not straight, or distance, if the line is straight.

ix. Click the start point and then hold Ctrl and click the end to measure the length of polyline (if the distance is not a straight line).

x. Click the start point and then drag to the end to measure the length of a distance (if the distance is a straight line).

xi. To undo the last step, right-click on the right to Scene Tree and choose Delete.

3.12 Measuring Permeability Using Nano-Perm Machine

The Nano-Perm machine, shown in Figure 3-6, is designed to measure the permeability of the ultra-low permeability shale reservoirs, especially unconventional shale reservoirs. Permeability was measured using the Nano-Perm machine, as shown in Figure 3-5. The Nano Perm rig consists of two core holders (D & E) that can be pressurised with an overburden pressure of up to 276 bar, by using the hydraulic pump (G). A meniscus tube (C) is used to monitor the movement of the liquid in mm/s (industrial coloured oil is usually used to be clearly seen through the meniscus glass). The Console Switch (A) is used to switch the machine on and off, and a vent valve (B) is used to release the overburden pressure (34.5, 69, 103.5, 100, 138, 150, 200 bar) when the experiment is completed. Gas Valve (F) is used to control nitrogen from the cylinder and is used to build differential pressure for the permeability measurements, shown in Figure 3-5 (for more detail, see Appendices B, D and E).

A: Console Switch,	B: Vent Valve,	C: C: Meniscus Tube,
D: Core Holder (i),	E: Core Holder (ii)	F: Gas-In Valve,
G: Overburden Pressure Pump.		

Figure 3-6: Nano-Perm Machine at Petroleum Lab, the University of Salford

3.13 Experimental Procedure for the Nano-Perm Machine

The following steps were used when operating the Nano-Perm machine:

i. Open the Nitrogen Tap.
ii. Turn the regulator of nitrogen pressure to 100 psi (6.9 bar).
iii. Use the overburden pump to achieve the desired overburden pressure (check the pump oil level).
iv. Turn the Gas-In valve to get a differential pressure of 35 psi (2.413 bar).
v. Start the stopwatch, and when done read off the meniscus and stop the stopwatch and record the time.
vi. Divide the meniscus (cc) by the time it took to evaluate ‘Q’.
vii. Substitute in the equation to calculate the permeability.

3.14 Experimental Procedure

At the set overburden pressure required and differential pressure 35 psi (= 2.413 bar), permeability through the sample was obtained by measuring the displacement of the industrial oil. The flow rate reading in mm/s is divided by the time in seconds taken by the stopwatch to find the flow rate (Q). By knowing the area of sample (A), the sample length (L), the atmospheric pressure (Pa), viscosity ($\boldsymbol{\mu}$), differential pressure ($\Delta \boldsymbol{P}$) and mean pressure (Pm), and by using Eq. 3.1, the permeability (K) can be calculated.

$$\boldsymbol{K_{air}} = \frac{\boldsymbol{Q} * \boldsymbol{\mu} * \boldsymbol{L} * \boldsymbol{Pa}}{\Delta \boldsymbol{P} * \boldsymbol{Pm} * \boldsymbol{A}} (\boldsymbol{mD}) \qquad 3.1$$

3.15 Permeability Error Estimation

The error in permeability measurement, which occurred while reading the meniscus tube, is estimated to be ± 1 cc/s. This measurement error also includes the tuning option with a stopwatch whilst taking the readings. The error bars are shown in Figures 4-8 and 4-15.

3.16 X-ray Fluorescence (XRF) for Shale Composition

This equipment belongs to Energy Dispersive X-ray Fluorescence Technology (ED-XRF). An x-ray fluorescence spectrometer (XRF) is an x-ray tool used for the comparatively non-destructive chemical analyses of rocks and fluids. This was used to measure the chemical composition of the shale samples.

Figure 3-7: X-ray Fluorescence (XRF) Spectrometer

3.16.1 Principles of XRF

The XRF technique relies on essential principles that are shared by several other instrumental devices, involving interactions between electron beams and x-rays with specimens. The breakdown of elements into geological materials, by using x-ray fluorescence, is made possible when materials are stimulated through high-energy, short wavelength radiation, when they become ionised. If this energy is sufficient to remove an inner electron, then the atom becomes unstable and an outer electron substitutes for the missing inner electron. Once this occurs, energy is released due to the reduced binding energy of the inner electron with an outer electron. Since the energy of the released photon is characteristic of a transition between a definite electron shell in a specific element, then the resulting fluorescent x-rays can be used to identify elements that are available in the sample.

3.16.2 XRF Calibration

The XRF calibration used the mining setting ‘all geological’, i.e. the calibration measures the complete elemental list. The device is calibrated by the company each year (which is standard practice for this type of device) and was checked on the day with a Certified Reference Materials

(CRM). The values fell within the parameters and were used in the characterisation. The setting used on the XRF estimates the amount of the element in the sample; it does not use equations to see if it is a carbonate, etc. For more detail on the calibration applied and to compare between CRM and the characterisation provided by the XRF spectrometer, refer to the Certified Reference Materials Table: G1, page 189, Appendix G.

The equipment was set up in a bench stand complete with a lead shield and was remotely controlled via a laptop. Each sample was analysed by the ends of the core. Each end was scanned 3 times for 600 seconds to give the direct ppm (parts per million) of elements and not oxides, etc. These fell within the acceptable error and the limits of detection (LOD) of the device (if any of the elements fell outside of the requirements, the device would be sent for repair, because once it has given one element error, the rest could also be faulty).

The definition of 'quantitative' XRF analysis depends, significantly, on the application and the planned use for the data. For environmental applications, the XRF results are quantitative, and if the measurement accuracy is within 20%, the results are accepted by an approved research laboratory method (US EPA/ERT, 1991).

3.16.3 Fundamental parameters calibrations

Fundamental parameter (FP) techniques have been understood and utilised on laboratory XRF systems to analyse a varied number of materials. In history, FPXRF instruments that have been applied for environmental use have depended on site-specific calibration methods but with the availability of field portable computing power, the fundamental approach is valid for FPXRF analysers and offers multi-site capabilities. However, uncertainties in the data used to generate theoretical coefficients may lead to errors and biases in FP analytical models, which are based on these data. Therefore, changes based on certified reference materials may be necessary to produce dependable results. Rather than empirical methods that require matrix-specific calibration standards, the FP approach utilises theory to pre-determine interelement coefficients. The lower the average atomic number of the sample, the higher the intensity of the incoherently scattered peak. Several criteria must be met to successfully apply FP techniques in XRF analyses (Kalnicky et al., 1995).

3.16.4 Analysis

i. X-ray fluorescence is utilised in most chemical analyses of key elements (Si, Ti, Al, Fe, Mn, Mg, Ca, Na, K, P) in rocks and sediments.
ii. Majority of chemical analyses are of trace elements (in loads >1 ppm; Ba, Ce, Co, Cr, Cu, Ga, La, Nb, Ni, Rb, Sc, Sr, Rh, U, V, Y, Zr, Zn) in rocks and sediments.

3.16.5 XRF Limitations

In theory, the XRF has the capability to sense x-ray emissions from practically all elements reliant on wavelength and the strength of incident x-rays. Nevertheless, in practice, most economically existing instruments are restricted in their capability to exactly and precisely measure elements that have $Z<11$ in most expected earth resources; for example, from hydrogen to neon, Z is the atomic number.

3.17 Chapter Summary

This chapter has provided detail on the preparation of the shale samples from the four different reservoirs to investigate the effects of fracture orientation on permeability. Also discussed in this chapter was the experimental setup and procedures that were used to characterise the material composition of the shale, namely porosity, which was measured using the CT scan and the liquid saturation method. The permeability of the shale was measured using the Nano-Perm machine. The following chapter will discuss the results of the analyses in relation to the fracture orientation on permeability and the impact this may have on well productivity.

Chapter 4: Results and Discussion

4.1 Overview

This chapter presents the results and discusses the findings of the research. The findings will be presented in the following order:

- Shale composition,
- Porosity (CT Scan),
- Shale Porosity,
- Permeability (Nano-Perm), and
- Liquid Saturation method to measure porosity.

4.2 Shale composition: X-ray Fluorescence (XRF)

The XRF technique involves interactions between electron beams and x-rays with specimens. Since the energy of the released photon is characteristic of a transition between a definite electron shell in a specific element, the resulting fluorescent x-rays can be used to identify chemical elements that are available in the sample.

Following the XRF analysis, the results recorded in Table 4-3 shows that silicon (Si) and aluminium (Al) are the chief elements in the Mancos rock, adding to nearly 37% of the entire weight. Bal (balance) is not an element but the remainder of chemical compositions that could not be analysed by the XRF (such as oxygen, nitrogen, carbon). Other elements, for instance, magnesium (Mg), iron (Fe), sulphur (S) and titanium (Ti), can also be observed as slight contents, i.e. less than 1.8%. For more detail on the shales' chemical analysis, refer to Table: F3, page 181, Appendix F.

4.3 Barnett, Eagle Ford, Mancos and Marcellus Shales

4.3.1 Barnett Shale

Table 4-1: Percentage Breakdown of the Barnett Shale Sample Chemical Elements & Others

Chemical	Average Percent
Bal	53
Ca	41
Si	3
Others*	4

*Others: Total of all chemical elements in the sample that individually are less than 1.8%

Figure 4-1 and Table 4-1 show the results achieved from the x-ray spectrometer analysis of the Barnett Shale core sample analysed by XRF. At 53%, 'Bal' (Balance: elements that are not predictable by the XRF) has a higher percentage. The next largest percentage in the core sample is calcium at 41%, followed by silicon at 3%. Further elements that contain a percentage lower than 1.8% include sulphur, iron, and potassium amongst others; these are termed as 'others' and total 4%.

In the current characterisation, it can be concluded that the calcium element ratio is elevated in the Barnett Shale sample and that is why the sample is not as cemented in comparison with other shale samples. This is consistent with XRF chemical analysis results (Table: F1, page 171, Appendix F gives further information on the chemical analysis).

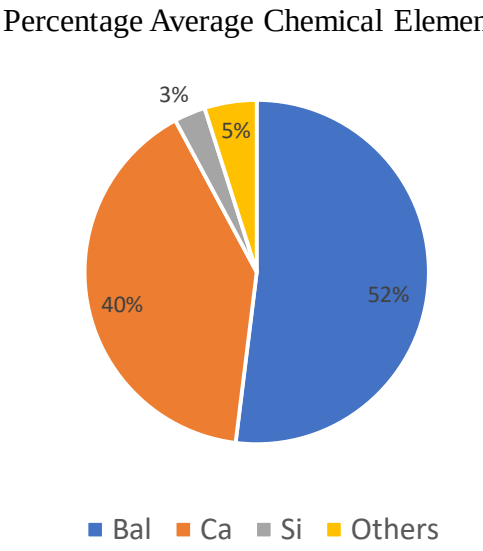

Figure 4-1: X-Ray Fluorescence for Barnett Shale Characterisation

4.3.2 Eagle Ford Shale

Table 4-2: Percentage Breakdown of the Eagle Ford Shale Sample Chemical Elements & Others

Chemical	Average Percent
Bal	53
Ca	28
Si	16
Others*	3

* Others: Total of all chemical elements in the sample that individually are less than 1.8%

Figure 4-2 and Table 4-2 demonstrated the results reached from the x-ray fluorescence analysis of the Eagle Ford core shale sample examined by XRF (further detail is provided in Table: F2, page 175, Appendix F). It can be seen that Bal. (Balance: comprising the elements not known by the XRF) represents the highest percentage of 53%. Calcium comprises another large

percentage at 28%, whilst silicon encompasses 16% in the analysed sample. The remainder of the elements make up a percentage of less than 1.8%, and include, for example, sulphur, iron, and potassium. Other compositional elements are labelled as 'others' in Figure 4-2 and comprise 3% of the sample.

It can be deduced that the calcium share is larger in the Eagle Ford Shale core sample, which explains that the sample is highly cemented compared with other shale core samples. This is clearly found in the XRF analysis (in Appendix F, on page 172).

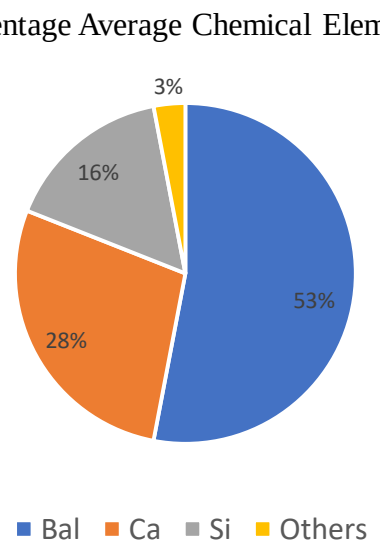

Figure 4-2: X-Ray Fluorescence for Eagle Ford Shale Characterisation

4.3.3 Mancos Shale

Table 4-3: Percentage Breakdown of the Mancos Shale Sample Chemical Elements & Others

Chemical	Average Percent
Bal	53
Si	31
Ca	5
Al	6
Others*	10

* Others: Total of all chemical elements in the sample that individually are less than 1.8%

Figure 4-3 and Table 4-3 indicated the results attained from the x-ray fluorescence analysis of the Mancos Shale sample tested by the XRF. Bal. has the highest percentage at 53%, whilst silicon represents another large percentage at 31%. This is followed by the calcium element at 5% and aluminium element at 6%, and 'other' elements represent less than 2% in the sample (for example, sulphur, iron, and potassium amongst others).

It can be ascertained that the calcium ratio is too small in the analysed Mancos Shale sample, which is why the sample is not as cemented as other shale samples. This understood from the XRF analysis (further detail is shown in Appendix F on page 172).

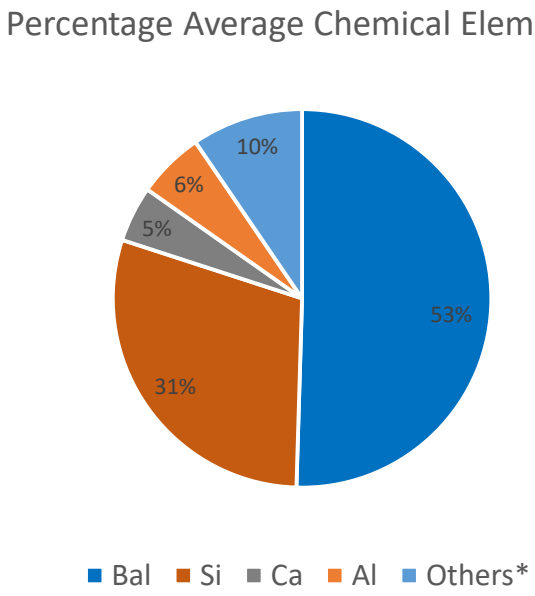

Figure 4-3: X-ray Fluorescence for Mancos Shale Characterisation

4.3.4 Marcellus Shale

Table 4-4 indicates that calcium (Ca), silicon (Si) are the prime elements in this shale rock study, constituting nearly 45% of the whole weight. Extra elements, such as potassium (K), sulphur (S) and iron (Fe) can be also detected but at smaller contents.

Table 4-4: Percentage Breakdown of the Marcellus Shale Sample Chemical Elements & Others

Chemical	Average Percent
Bal	53
Ca	43
Si	2.0
Others*	2.0

* Others: Total of all chemical elements in the sample that individually are less than 1.8%

Figure 4-4 and Table 4-4 designated the results obtained from the x-ray fluorescence analysis of the Marcellus Shale sample tested using the XRF fluorescence. It can be understood from Figure 4-4 that the Bal. (Balance: the remainder of the elements which cannot be measured) represents the main percentage at 53%. The second largest percentage, at 43% is calcium, followed by silicon at around 2%, which is low; however, this is according to the XRF results (refer to Table: F4, page 185, Appendix F). Other elements that comprise less than 1.8% of the sample include K, S, Fe and Al, among other elements, and are named 'others' in Figure 4-4. Thus, it seems that the calcium element is more important in the composition of Marcellus Shale sample, as there is a raised degree of cementing in this sample compared with other samples.

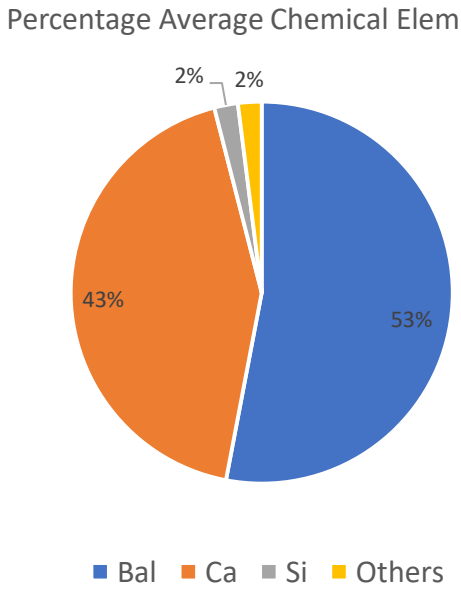

Figure 4-4: X-ray Fluorescence for Marcellus Shale Characterisation

4.4 Induced Fracture

The induced fracture crack width and crack length were also measured by using the CT scan reconstruction technique. The crack width was measured at four locations then averaged; these are shown in Table 4-5, along with the diameter of the samples.

The average crack width and the crack length are found for 4 samples collected from Marcellus Reservoir; the crack width and crack length for the other two samples are not taken as these are unfractured and fractured at different orientation angles, as demonstrated in Table 4-5.

Table 4-5: The Crack Width and Crack Length Measurement

Sample fracture type	Size, mm	Reservoir	Average crack width, mm	Crack length, mm	See Figure
Unfractured 1	6.35 (L)*37.44 (D)	Marcellus Shale	0.21	6.35	4.10 (a & b)
Horizontal 2	27.72 (L)*37.44 (D)	Marcellus Shale	0.14	37.44	4.10 (g & h)
90^0 vertical 3	27.72 (L)*37.44 (D)	Marcellus Shale	0.22	37.44	4.10 (c & d)
Two 90^0 vertical 4	27.72 (L)*37.44 (D)	Marcellus Shale	0.19	37.44	4.10 (e & f)
Triangle complex 5	13.4 (L)*37.44 (D)	Marcellus Shale	NA*	NA*	4.10 (k & l)
Line complex 6	13.4 (L)*37.44 (D)	Marcellus Shale	NA*	NA*	4.10 (i & j)

*The crack width and crack length were not measured for samples 5 and 6. Measuring all samples was unnecessary as the same hack-saw was utilised to induce fractures for the same shale samples.

As can be seen, three different lengths were used in the analysis because the length of the sample does not affect the crack width and crack length. For full measurement steps via the CT scan, refer to Table B2, page 153, Appendix B.

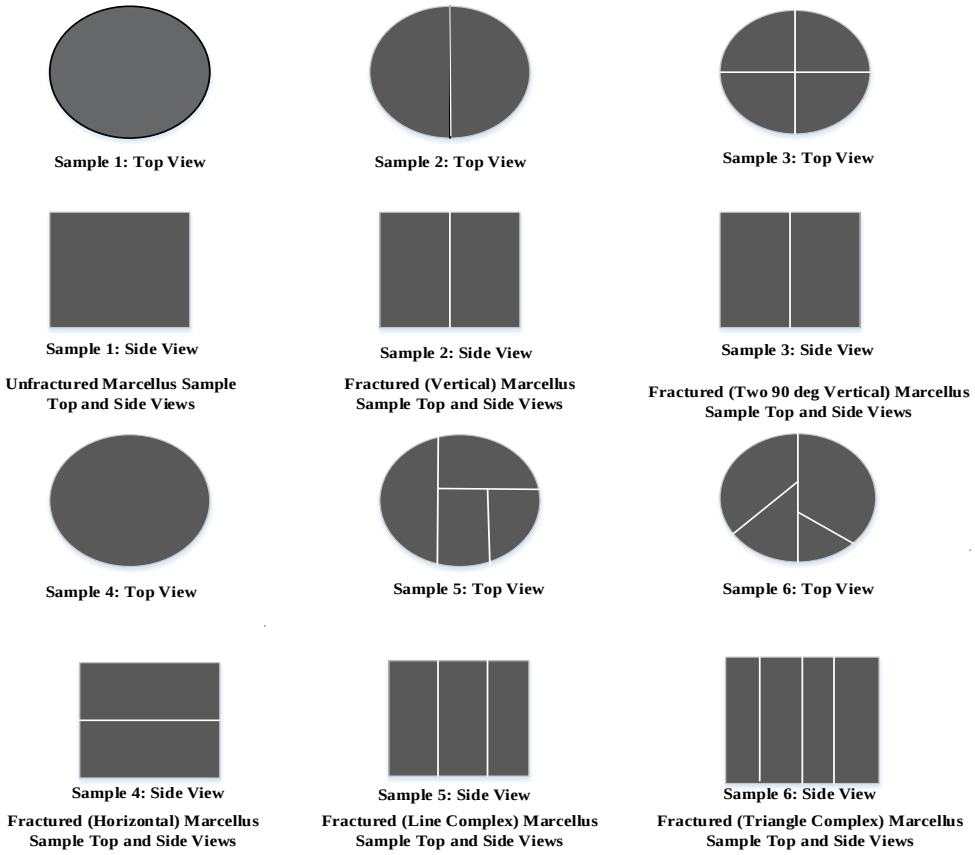

Figure 4-5: Crack Width and Crack Length Measurement

4.5 Porosity Calculation and CT scan Image Construction

The Eagle Ford, Mancos and Marcellus samples are the first sets of unfractured shale samples* that were used to measure the porosity using a CT scan. The porosity is calculated using the CT scan, as demonstrated in Figure 4-6, which presents the value of the percentage voids. For example, the Marcellus porosity for the unfractured sample is equal to 1.37%.

* The first set of shale samples comprises Eagle Ford, Mancos and Marcellus, refer to Table 4-6,

* The second set of shale samples only comprises Marcellus Shale, refer to Table 4-5,

* The third set of shale samples comprises Barnett, Eagle Ford, Mancos and Marcellus, refer to Figure 4-13, and for the chemical analysis, refer to Appendix F, page 172.

Table 4-6 presents the porosity values and description for the Eagle Ford, Mancos and Marcellus Shales for the non-fractured samples. The shale samples have similar levels of porosity regardless of the bedding plane and the reservoir from which they were obtained.

Table 4-6: The Porosity Values for Each Sample.

Samples No	Sample size, mm	Description	Porosity%
Sample 1	152.4 (L)*50.8 (D)	No Fracture Eagle Ford (parallel to the bedding plane)	5.08
Sample 2	152.4 (L)*50.8 (D)	No Fracture Mancos (perpendicular to the bedding plane)	5.05
Sample 3	152.4 (L)*50.8 (D)	No Fracture Mancos (parallel to the bedding plane)	4.45
Sample 4	152.4 (L)*50.8 (D)	No Fracture Marcellus (perpendicular to the bedding plane)	5.25
Sample 5	152.4 (L)*50.8 (D)	No Fracture Marcellus (parallel to the bedding plane)	5.76

Table 4-6 shows that the porosity was measured before fracturing. The directions in which the samples were cut in the reservoir formation were parallel or perpendicular to the bedding plane.

The porosity of the unfractured and fractured samples was found using the CT scan and is shown in Figures 4-6 and 4-7 as the value of percentage voids. Here, the Marcellus porosity for the unfractured sample is 1.37%, (for more detail, refer to Table B2, page 153, Appendix B).

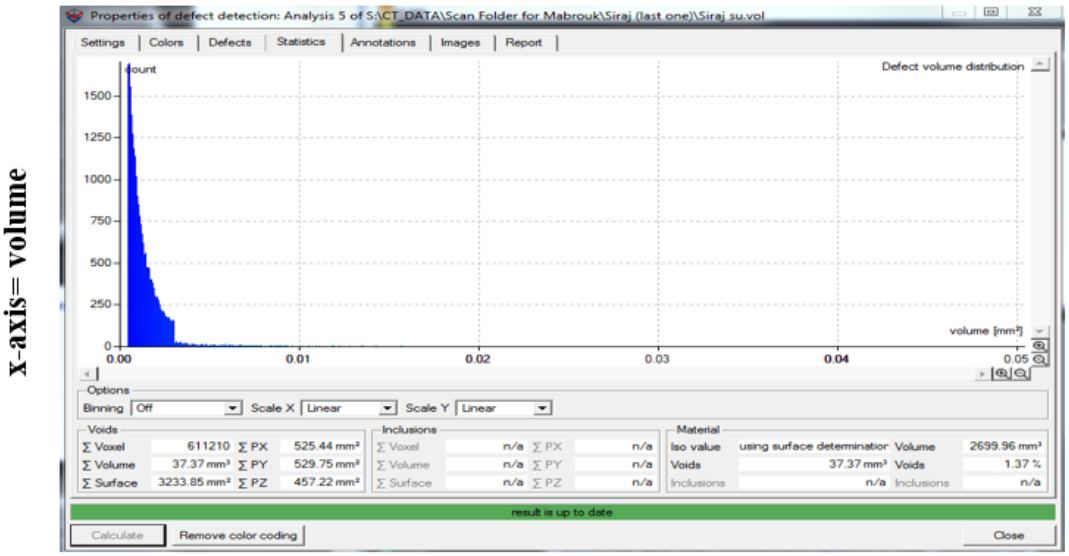

Figure 4-6: Marcellus Unfractured Shale Sample (1) Porosity Computation using CT Scanner

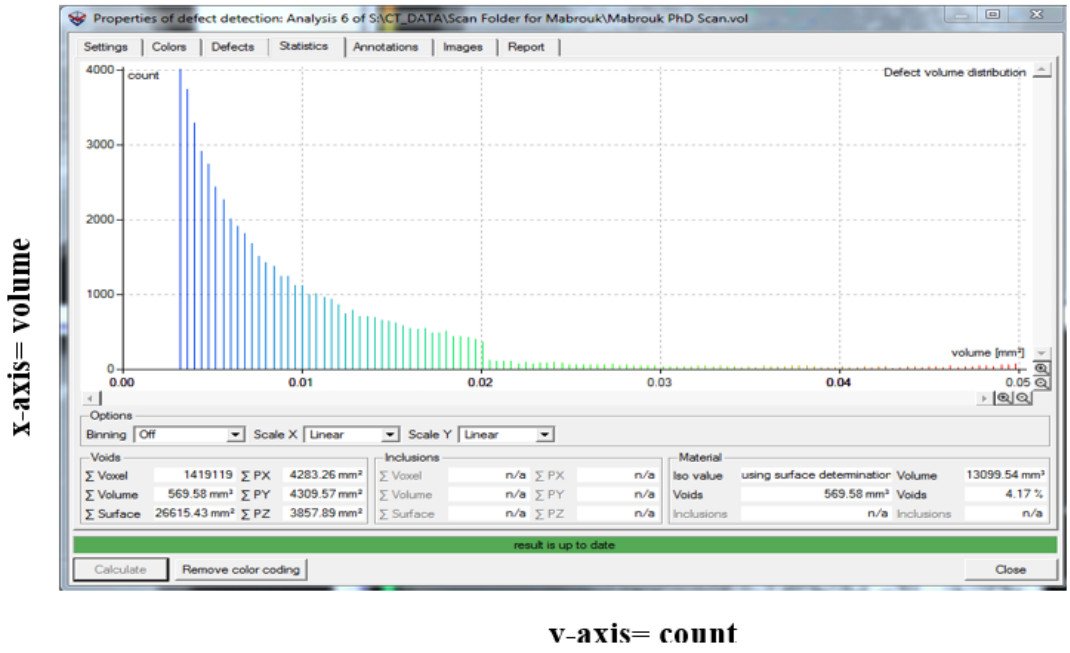

Figure 4-7: Marcellus Horizontal Fractured Shale Sample (2) Porosity Computation using CT Scanner.

Table 4-7 presents the different porosity values between the unfractured (1) and fractured Marcellus Shale samples (2, 3, 4, 5 and 6). It is clear that, when the sample is fractured, the

porosity increases as the fractures create extra percentage voids in the rock. The more complicated the fracture, the greater the porosity.

Table 4-7: Marcellus Shale Porosity Values

Shale Type	Sample size, mm	Porosity
Marcellus Unfractured Shale Sample Porosity (1)	6.35 (L)*37.44 (D)	1.37%
Marcellus Horizontal Fractured Shale Sample Porosity (2)	27.72 (L)*37.44 (D)	4.17%
Marcellus Vertical Fractured Shale Sample Porosity (3)	27.72 (L)*37.44 (D)	4.50%
Marcellus Double Fractured Shale Sample Porosity (4)	27.72 (L)*37.44 (D)	4.89%
Line Complex fracture (5)	13.4 (L)*37.44 (D)	1.81%
Triangle Complex fracture (6)	13.4 (L)*37.44 (D)	1.82%

The overburden pressures represent well depths of 345m, 690m, 1034m and 1379m, as seen in Table 4-8.

Table 4-8: Overburden Pressure and Corresponding Well Depths

Bar	MPa	Well Depth in Meters
34.5	3.45	345
69	6.90	690
103.5	10.35	1034
138	13.80	1379

In Alaska, the vertical stress fluctuates with depth with most of the wells experiencing 0.85 to 1 psi/ft (McNeal et al., 2017). Moreover, it was noted in the literature that every 207 bar of

overburden matches around 152.4 m burial depth of a typically compressed reservoir (Fatt and Davis, 1952).

4.6 Permeability Results for the Second Set of Shale Samples (Marcellus)

Preliminary testing using a Marcellus Shale sample was undertaken. Table 4-7 shows the porosity for the following Marcellus Shale samples: unfractured (1), fractured horizontal (2), 90-degree vertical (3), two 90-degree vertical (4), line complex (5), and triangle complex (6) fractures. The porosity crack length and width were characterised using the CT scanner and the permeability was obtained using the Nano-perm machine.

The porosity increased from unfractured to triangle complex fractured; this was due to the creation of more voids. The average crack width ranged from 0.14 to 0.22 mm. Furthermore, permeability is affected by the type of fracture (for complex maximum value) and the amount of overburden pressure, and is inversely related to the overburden pressure.

When comparing permeability with the type of fractures made, the permeability increased as follows: from unfractured (1) to 90^0 vertical (2), two 90^0 (3), horizontal (4), and finally, at complex and triangle complex (5+6) fractured shale samples, the permeability was low due to the extra lapping. Moreover, in all of the fracture cases, it can be seen that the complex fractures produced the lowest levels of permeability. It would have been expected that more complex fractures would have greater permeability due to the greater number of passageways through the sample.

It can also be seen that two parameters affect the permeability pressure and type of fracture; the more pressure, the less permeability, and a greater sample fracture increases the permeability. The researcher tried to measure the permeability before and after fracturing to compare the two cases but it was not possible as the shale samples are ultra-low in permeability.

Table 4-9: Comparison of Permeability, Porosity and Crack Width & Length for the Second Set of Shale Samples (Marcellus).

Marcellus Shale Samples	Sample Size, mm	Porosity% (CT Scan)	Average Width, mm (CT Scan)	Length, mm CT Scan	Permeability, mD: Nano-Perm				Figure No
					34.5 bar	69 bar	103.5 bar	138 bar	
Sample 1: Unfractured (natural)	6.35 (L) * 37.44 (D)	1.37	0.21	34.26	$2.80126 * 10^{-8}$	$2.701225 * 10^{-8}$	$2.6811 * 10^{-8}$	$2.20112 * 10^{-8}$	See Figure B1
Sample 2: Vertical fracture	27.72 (L) *37.44 (D)	4.50	0.22	37.44	Permeability had not been measured for 34.5 bar for sample (2)	$1.7295 * 10^{-7}$	Permeability had not been measured for 103.5 bar for sample (2)	$1.6666 * 10^{-7}$	See Figure B2
Sample 3: Two 90^0 vertical Fracture	27.72 (L) * 37.44 (D)	4.89	0.19	37.44	$3.6870 * 10^{-7}$	$3.555 * 10^{-7}$	$3.4237 * 10^{-7}$	$3.160 * 10^{-7}$	See Figure B3
Sample 4: Horizontal fracture	27.72 (L) * 37.44 (D)	4.17	0.14	37.44	$1.2229 * 10^{-7}$	$1.1792 * 10^{-7}$	$1.1355 * 10^{-7}$	$1.0482 * 10^{-7}$	See Figure B4

Sample 5: Line Complex fracture	13.4 (L) * 37.44 (D)	1.81%	NA*	NA*	$8.7347 * 10^{-8}$	$7.8612 * 10^{-8}$	$7.4244 * 10^{-8}$	$6.9876 * 10^{-8}$	See Figure B5
Sample 6: Triangle Complex fracture	13.4 (L) * 37.44 (D)	1.82%	NA*	NA*	$8.0560 * 10^{-8}$	$7.6003 * 10^{-8}$	$7.1777 * 10^{-8}$	$6.9671 * 10^{-8}$	See Figure B6

*The crack width and crack length were not measured for samples 5 and 6 because these would not differ from the other samples as the same hack-saw was used to induce fractures for all samples.

Figure 4-8 shows the Marcellus Shale permeability at 69 bar and 138 bar for unfractured (1), 90^0 vertical (2), two 90^0 vertical (3), horizontal (4), line complex (5) and triangle complex (6) fractured shale samples (see Figure 4-4).

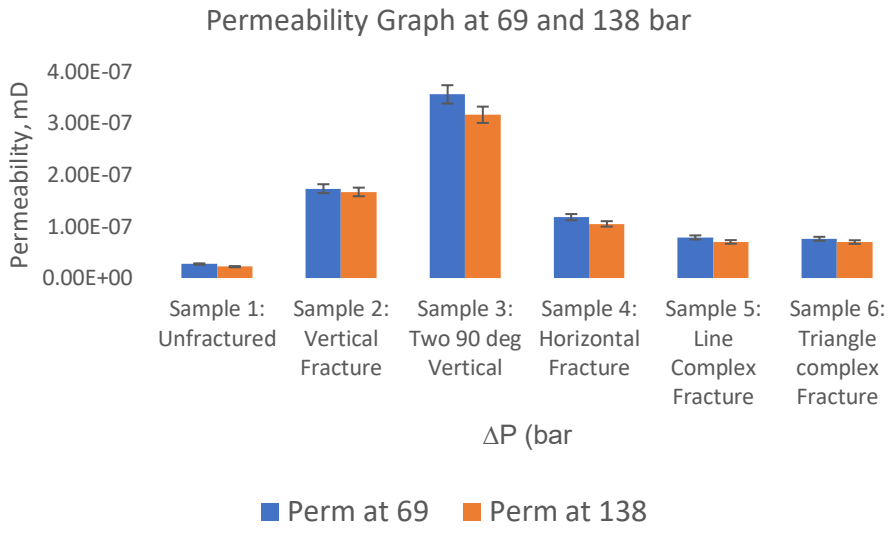

Figure 4-8: Permeability of Marcellus Shale Samples for different fracture permutations

The permeability for the fractured samples at an overburden pressure of 69 bar and 138 bar are shown in Figure 4-8. The permeability values at 69 bar are higher than at 138 bar because of the compression, where more compression means less permeability and vice versa. Thus, it was noted that the more complex the fracture, i.e. more passageways, the greater the permeability.

4.7 Calculation of Porosity using the Liquid Saturation Method

To determine the pore volume, the weight of the six dry samples, the second set of shale samples, which are unfractured and induced fractures (Marcellus Shale), were recorded to obtain a base weight. A salt solution with a density of 1.045 g/cm^3 was prepared using a hygrometer. The salt solution was used to represent the average salinity of the typical reservoir.

The shale samples were completely submerged in the salt solution and left for 24 hrs. The samples were then taken out, wiped with tissue cloth to remove any surface water, weighed, and the weights were recorded. This process was undertaken until a steady state of sample weight was observed. From the difference in weight, the pore volume was calculated using the following equation: $\Delta V = \frac{\Delta W}{\rho}\ cm^3$. This was used to calculate the porosity of the samples by

dividing pore volume of each sample by its bulk volume; this porosity was compared with the CT scan porosity for the same samples.

As shown in the unfractured sample (1), the weight increased from day 1 to day 3 and then became constant from day 3 to day 6, which was subsequently taken as the final weight. The weight was measured each day at the same time and then, from the difference, the pore volume and porosity were calculated for each sample.

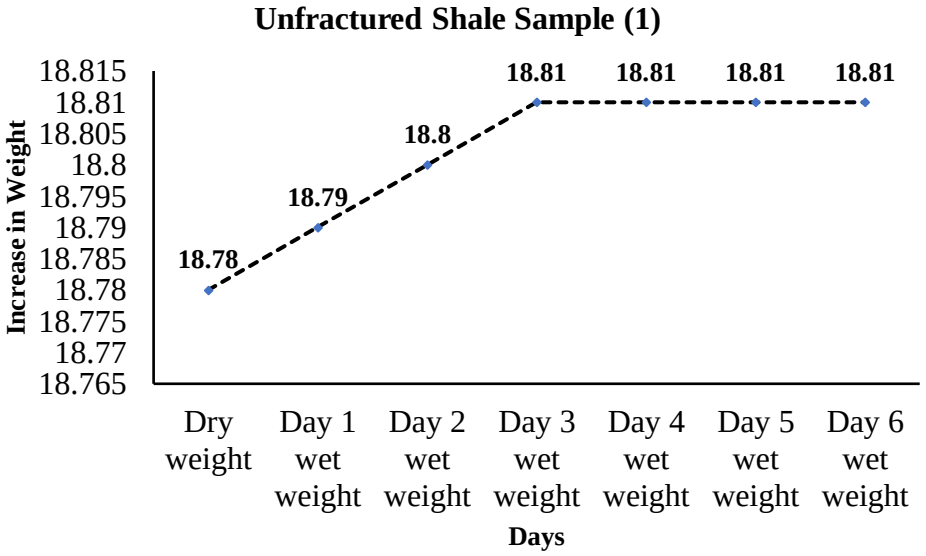

Figure 4-9: Unfractured Shale Sample Weight Difference

The weight of unfractured shale sample (1) gradually increased, as demonstrated in Figure 4-10, which then became constant for the last three days of the experiment.

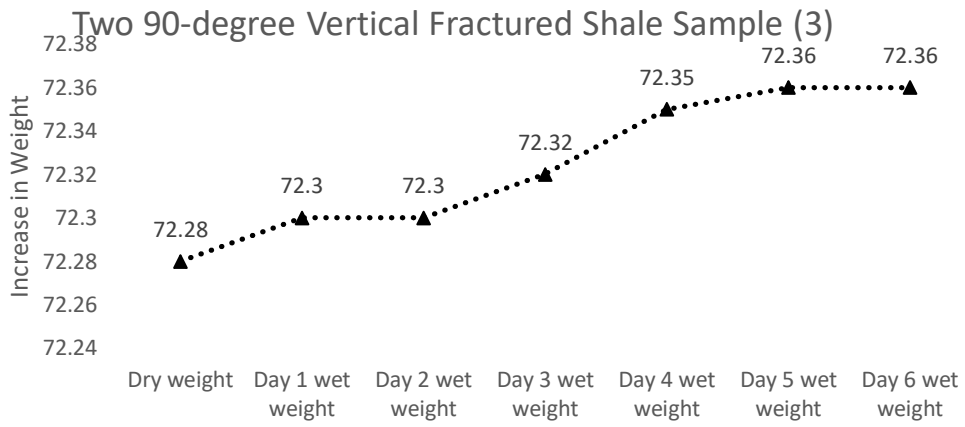

Figure 4-10: Two 90-degree Vertical Fractured Shale Sample Weight Difference

As can be seen in Figure 4-11, the weight of the two-vertical fractured sample (3) gradually increased over the first 4 days and then became constant after day 5.

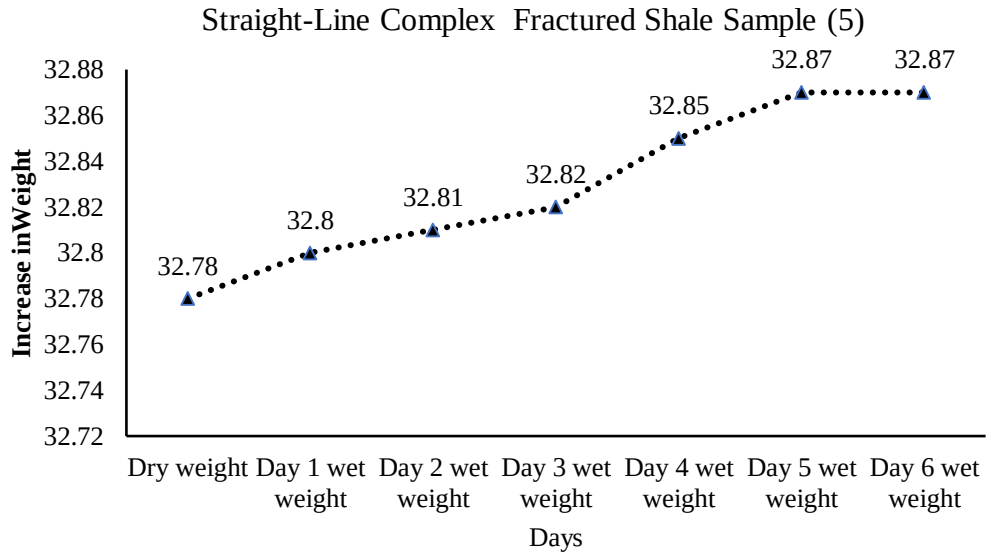

Figure 4-11: Straight-Line Complex Fractured Shale Sample Weight Difference

As shown in Figure 4-12, for sample (5) the saturation profile is similar to the previous fractures with saturation occurring after 6 days.

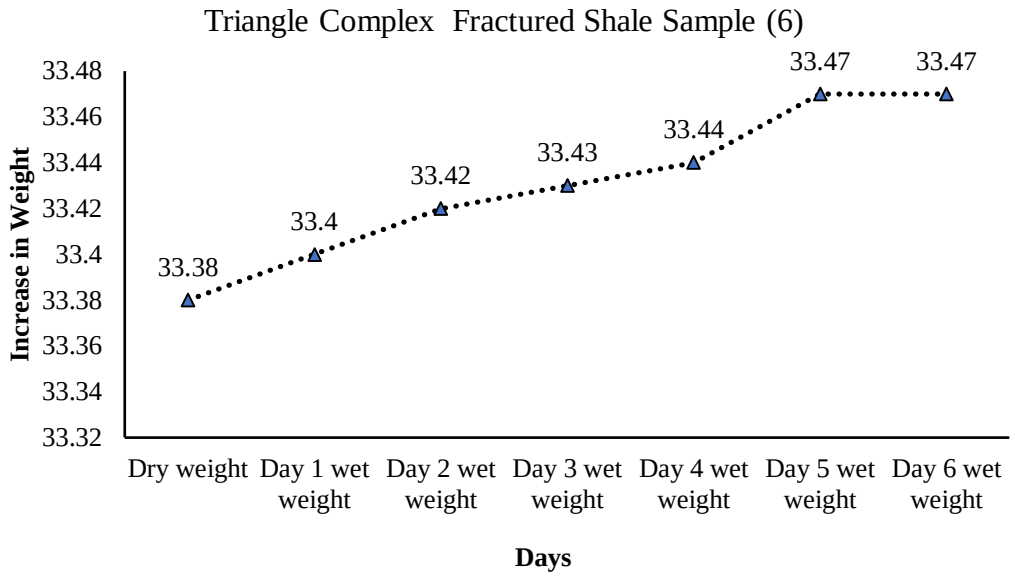

Figure 4-12: Triangle Complex Fractured Shale Sample Weight Difference

The difference in weight, shown in Table 4-10, was determined for the samples that were immersed in salt solution for six days, then the difference between the initial (dry) and the final (wet) weight for each sample was divided by the salt solution density to calculate the pore volume. This pore volume was divided by the bulk volume of each sample to find the porosity, which was then compared with the CT scan porosity for comparison and validation. As can be seen in Table 4-10, there is good agreement between the measurements of porosity using the CT scan method and the sample saturation method.

Table 4-10: Initial and Final Weight Difference of Marcellus Shale

(second set of shale samples).

Samples	Initial Weight W, g	Final Saturated Weight W_f, g	The difference Weight ΔW, g	Pore Volume ΔV, cm^3	Samples Volume V= $\Pi r^2 h$, cm^3	Sample Saturation Porosity (ϕ) = $\frac{Pore\ Volume}{Total\ Volume}$	CT scan Porosity
Sample 1: Unfractured	18.78	18.81	0.03	0.022887	3.14*$(\mathbf{1.872})^2$*0.635 = 6.98739	$\frac{\mathbf{0.02887}}{\mathbf{6.98739}}$ = 0.413%	0.40%
Sample 3: Two 90-degree Fractured Vertical	72.28	72.36	0.08	07656	3.14*$(\mathbf{1.872})^2$ *2.772 = 30.50244	$\frac{0.07656}{30.50244}$ = 0.251%	0.26%
Sample 5: Line Complex Fractured	33.38	33.47	0.09	0.08612	3.14*$(1.872)^2$ * 1.34 = 14.74504	$\frac{0.08612}{4.74504}$ =1.815%	1.81%
Sample 6: Triangle Complex Fractured	32.78	32.87	0.09	0.08612	3.14*$(1.872)^2$ * 1.34 = 14.74504	$\frac{0.08612}{4.74504}$ = 1.815%	1.82%

Note: Samples 2 and 4 did not exist when the liquid saturation method was used because they were refractured to produce other types of fractures.

The unfractured sample has a greater porosity, which can be related to the reduction of voids within the fractured samples. This was due to the artificial fracturing operation and due to the lapping, which might plug some of the porosity voids.

4.7.1 Mancos and Marcellus Permeability Test using the Nano-Perm Machine

Additional new samples (the third set of shale samples) from the Mancos and Marcellus Shales were obtained to further investigate the effects of complex fractures on permeability.

Figure 4-13 represents six samples from the Mancos and Marcellus Shales:

- Mancos sample 1 (No Fracture)
- Mancos sample 2 (Complex Fracture 1)
- Mancos sample 3 (Complex Fracture 2)
- Marcellus sample 4 (No Fracture)
- Marcellus sample 5 (Fracture 1)
- Marcellus sample 6 (Fracture 2)

The permeability values of these samples are given in Tables 4-9 to 4-25, and in the graphs shown in Figures 4-16 to 4-40. The Marcellus Shale is greater than Mancos Shale because of the mineral constituents (for example, calcium, 43%). The calcium ratio is higher in Marcellus than in Mancos (calcium, 5%), which is also the case for Barnett (calcium, 41%) and Eagle Ford (calcium, 28%). This implies that, if measured, Barnett has a greater permeability than Eagle Ford due to its incompressibility ratio. The elemental chemical composition values of these samples are detailed in Appendix F on pages 172 and 180.

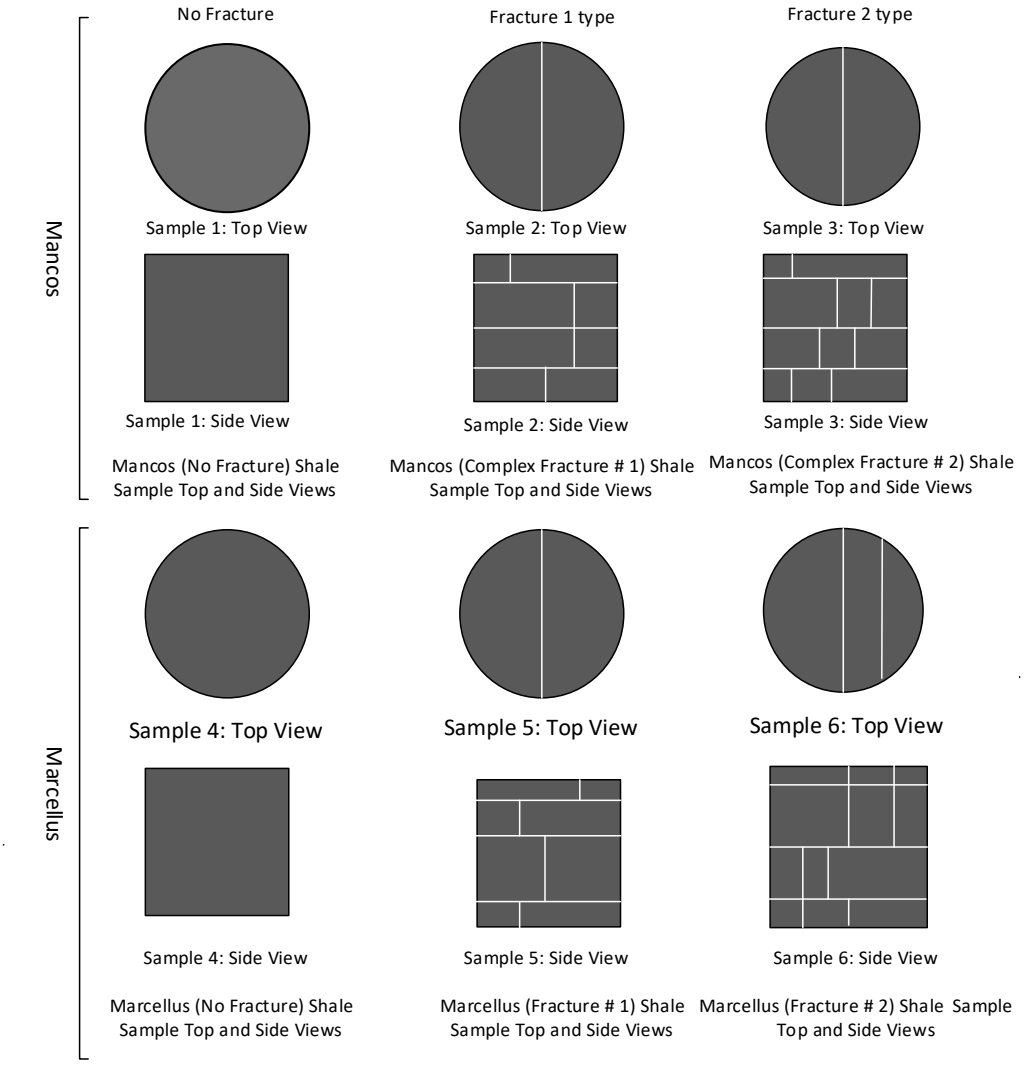

Figure 4-13: Unfractured and Fractured Mancos and Marcellus Shale Samples

Mancos Shale Fractures

Figure 4-14: Show Mancos Shale Sample (No Fracture)

In Figure 4-15 and Table 4-11, as expected, an increase in ΔP increases the permeability of the shale sample. Also, an increase in the overburden pressure from 100 bar to 150 bar decreases the permeability from 8.83E-07 mD to 1.13E-07 mD.

As recognised, the overburden pressure is inversely related to permeability as it causes compaction of the shale sample; however, ΔP is directly related to permeability because it represents the difference between the inlet and outlet pressures on the Nano-perm equipment. This is the reason why a greater ΔP will increase the flow rate. Thus, the permeability values for the Mancos Shale results are within the typical permeability range for shale from that region, (Torsaeter and Vullum, 2012).

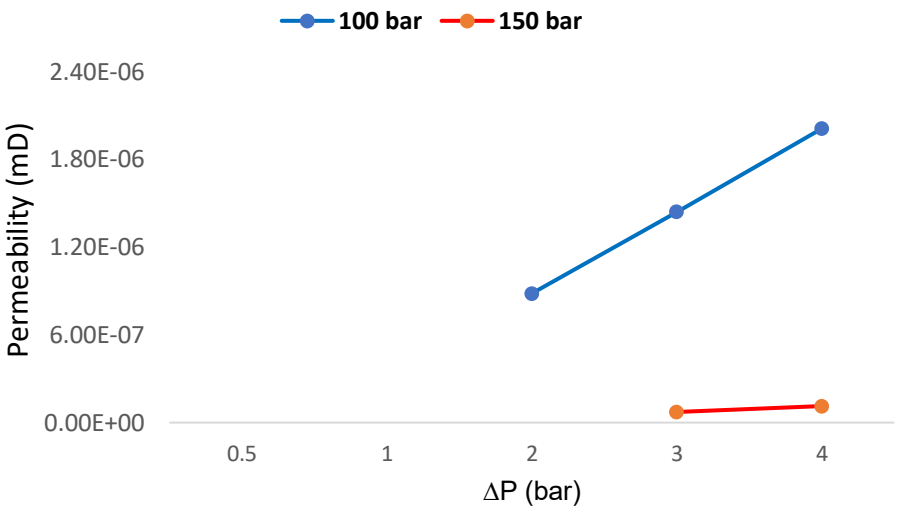

Figure 4-15: Mancos Shale (No Fracture) at 100 bar and 150 bar

Table 4-11: Mancos Shale (No Fracture)

Mancos Shale Sample - No Fracture					
ΔP, bar	0.5	1	2	3	4
100 bar			8.83E-07	1.44E-06	2.01E-06
150 bar				7.24E-08	1.13E-07

Figure 4-16: Mancos Shale Sample (Fracture 1)

For the Mancos fracture 1, Figure 4-17 and Table 4-12 shows that an increase in the value of ΔP causes an increase in the permeability of the shale sample. However, an increase in the overburden pressure from 100 bar to 200 bar reduces the permeability from 2.15E-04 mD to 5.02E-05 mD.

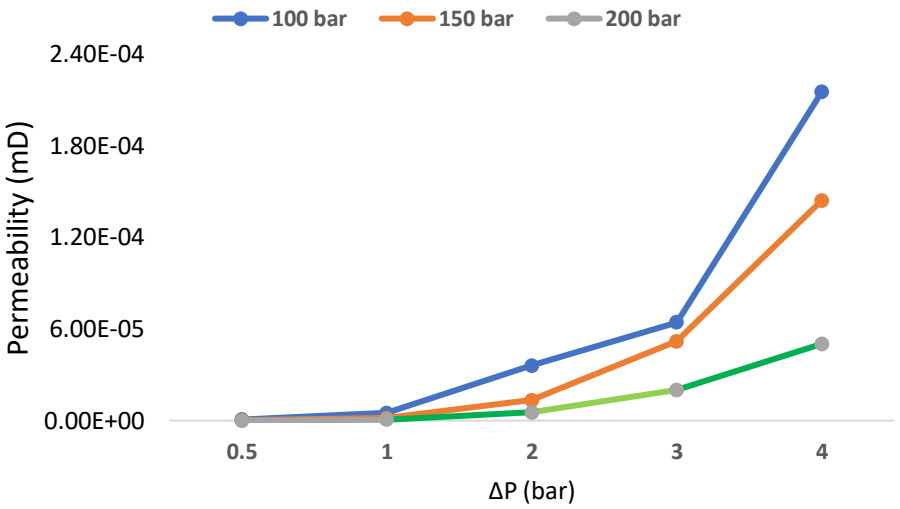

Figure 4-17: Mancos Shale (Fracture 1) at 100 bar and 150 bar and 200 bar Overburden Pressure.

As can be seen, the rate of change of permeability due to ΔP decreases significantly with the overburden pressure.

Table 4-12: Mancos Shale Sample (Fracture 1)

Mancos Shale Sample – Fracture 1					
ΔP, bar	0.5	1	2	3	4
100 bar	7.00E-07	5.00E-06	3.60E-05	6.42E-05	2.15E-04
150 bar	2.29E-07	1.65E-06	1.35E-05	5.20E-05	1.44E-04
200 bar	6.10E-08	5.72E-07	5.51E-06	2.01E-05	5.02E-05

Figure 4-18: Show Mancos Shale Sample (Fracture 2)

For fracture 2 Mancos shale, as shown in Figure 4-19, the permeability results show that the permeability at an overburden pressure of 100 bar is the greater. This is because the pore spaces are less compacted than at the 150 bar overburden pressure.

The permeability profiles with a change in ΔP show the rate of change to be more constant when compared to fracture 1 (Figure 4-17).

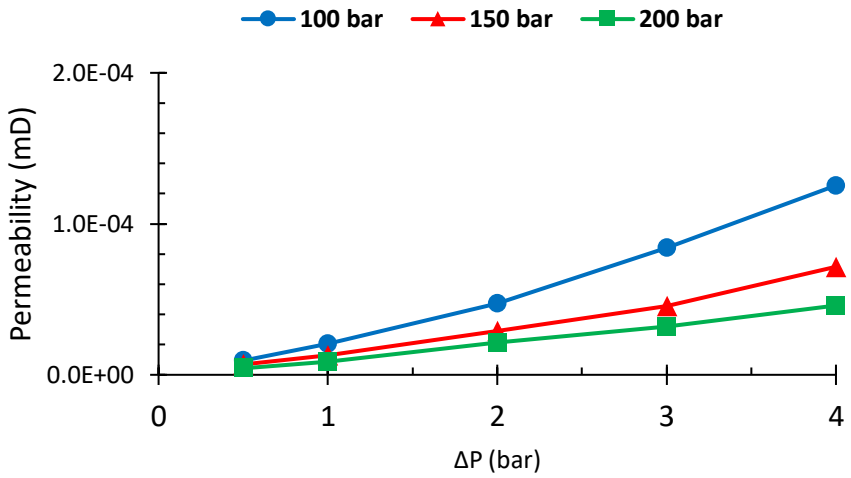

Figure 4-19: Mancos Shale (Fracture 2) at 100 bar and 150 bar and 200 bar Overburden Pressure

Table 4-13: Mancos Shale Sample (Fracture 2)

Mancos Shale Sample - Fracture 2					
ΔP, bar	0.5	1	2	3	4
100 bar	9.42E-06	2.04E-05	4.72E-05	8.41E-05	1.25E=04
150 bar	6.87E-06	1.30E-05	2.89E-05	4.57E-05	7.16E-05
200 bar	4.30E-06	8.59E-06	2.16E-05	3.19E-05	4.59E-05

Figure 4-19 and Table 4-13 illustrate an increase in ΔP which increases the permeability of the shale sample. Although there is an increase in the overburden pressure, from 100 bar to 200 bar, the permeability decreases from 1.25E-04 mD to 4.59E-05 mD at ΔP of 4 bar. Thus, the permeability is affected by the amount of overburden pressure because it causes compression in the shale sample. Fracture types 1 and 2 are compared with the Mancos Shale sample. An overburden pressure of 100 bar gives a greater flow rate because the compression is less than that at 150 bar and the flow rate for 150 bar is greater than that at 200 bar. The

flow rate will also be increased due to the complex fractures, which create more voids and spaces adding multichannel through the sample.

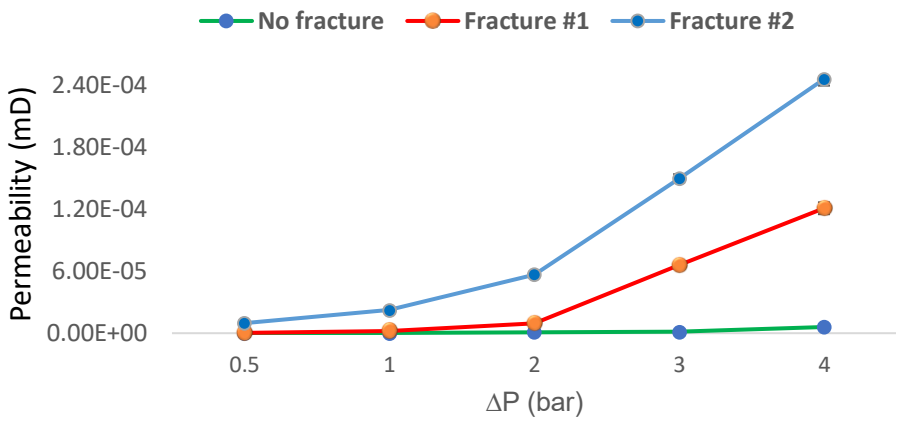

Figure 4-20: Mancos Shale Sample (No Fracture, Fracture 1 and Fracture 2) at 100 bar Overburden Pressure

It can be seen in Figure 4-20 and Table 4-14 that for a ΔP of up to 3 bar, fracture 1 has a lower permeability than fracture 2. This would be expected as there are two, rather than one, vertical parallel pathways, and hence greater connectivity. However, above a ΔP of 3 bar, the permeability of fracture 1 becomes greater than for fracture 2. One possible reason for this is that a greater ΔP causes the fracture to open, which increases the permeability.

In comparison, more complex fractures and the relative closeness of fractures that oppose each other effectively reduce the cross-sectional area of the passageways, which, therefore reduces the permeability.

Table 4-14: Mancos Shale Sample (No Fracture, Fracture 1 And Fracture 2) at 100 bar Overburden Pressure

100 bar Overburden Pressure					
ΔP, bar	0.5	1	2	3	4
No Fracture	8.30E-10	1.77E-07	8.83E-07	1.44E-06	5.97E-06
Fracture 1	3.05E-07	1.91E-06	8.66E-06	6.42E-05	1.15E-04
Fracture 2	9.42E-06	2.04E-05	4.72E-05	8.41E-05	1.25E-04

As can be seen in Figure 4-21, for an overburden pressure of 150 bar the expected permeability results would be less than for those at 100 bar. As shown in Figure 4-21, the profiles are similar to those in Figure 4-20. Thus, up to 3 bar ΔP for fracture 2 has a greater permeability. However, for greater than 3 bar, fracture 1, with its single vertical channels, has greater permeability.

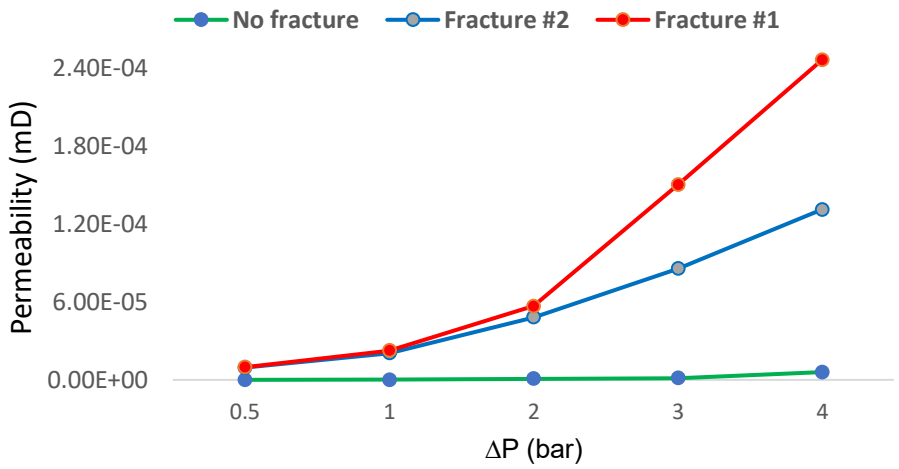

Figure 4-21: Permeability Measurement of Mancos Shale Sample at 100 bar Overburden Pressure.

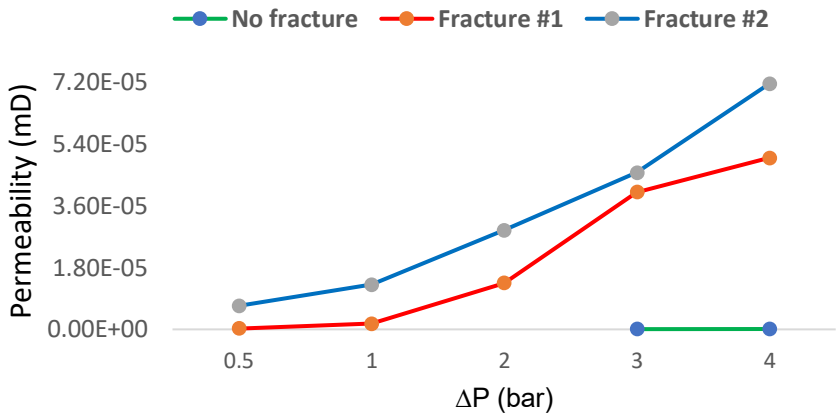

Figure 4-22: Mancos Shale (No Fracture, Fracture 1 And 2) at 150 bar Overburden Pressure

Table 4-15: Mancos Shale Sample (No Fracture, Fracture 1 and Fracture 2) at 150 bar Overburden Pressure

150 bar Overburden Pressure					
ΔP, bar	0.5	1	2	3	4
No Fracture				7.24E-08	1.13E-07
Fracture 1	2.29E-07	1.65E-06	1.35E-05	4.00E-05	5.00E-05
Fracture 2	6.87E-06	1.30E-05	2.89E-05	4.57E-05	7.16E-05

As seen in Figure 4-21 and Table 4-15, ΔP increases the permeability of the shale sample. For ΔP from 0.5 bar to 4 bar, the permeability of fracture 1 increases from 2.29E-07 mD to 5.0E-05 mD.

Figure 4-23: Show Marcellus Shale Sample (No Fracture)

From Figure 4-24 and Table 4-16, it can be understood that a rise in ΔP increases the permeability of the shale sample. However, an increase in overburden pressure from 100 bar to 150 bar decreases the permeability from 2.40E-05 mD to 2.00E-05 mD. Thus, K decreases when the overburden pressure increases.

4.7.2 Marcellus Shale Fractures

The permeability for the unfractured Marcellus Shale sample, at an overburden pressure of 100 and 150 bar, is shown in Figure 4-24. As can be seen, the permeability is very low at 150 bar; this is due to the overburden pressure which closes the pore spacing. The following shows the Marcellus Shale sample (No Fracture) at different overburden pressures.

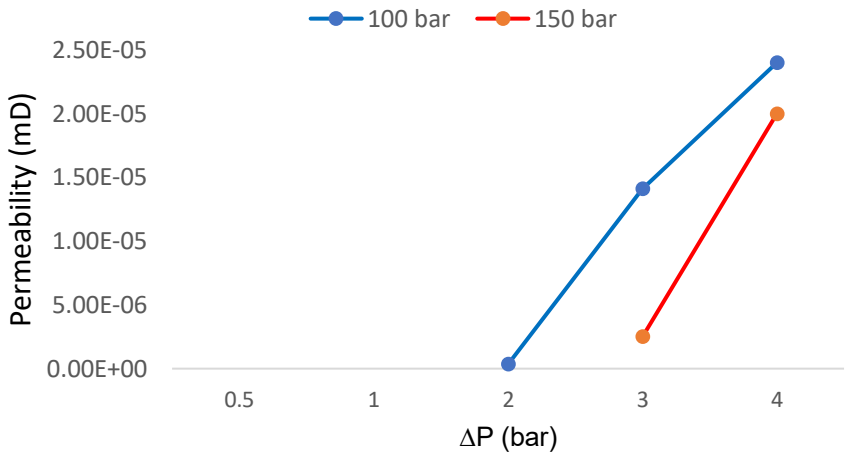

Figure 4-24: Marcellus Shale (No Fracture) at Different Overburden Pressures

Table 4-16: Marcellus Shale Sample (No Fracture) at 100 bar and 150 bar Overburden Pressure

Marcellus Shale Sample - No Fracture					
ΔP, bar	0.5	1	2	3	4
100 bar			3.42E-07	1.41E-05	2.40E-05
150 bar				2.50E-06	2.00E-05

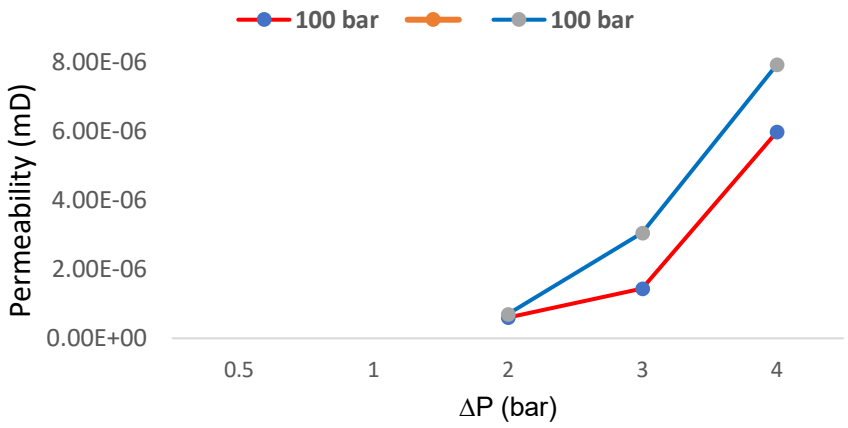

Figure 4-25: Comparison between Mancos and Marcellus Shale Samples

As seen in Figure 4-25 and Table 4-16, Marcellus has a greater permeability than Mancos at an overburden pressure of 100 bar. Marcellus has a higher permeability due to the higher amount of calcium, which is based on the findings from the application of the XRF technique. This makes the rock relatively incompressible, which helps to keep the permeability noticeably higher. Permeability, in general, is higher for both Mancos and Marcellus at 100 bar overburden pressure than at 150 bar. This is because the degree of compactness is less at 100 bar.

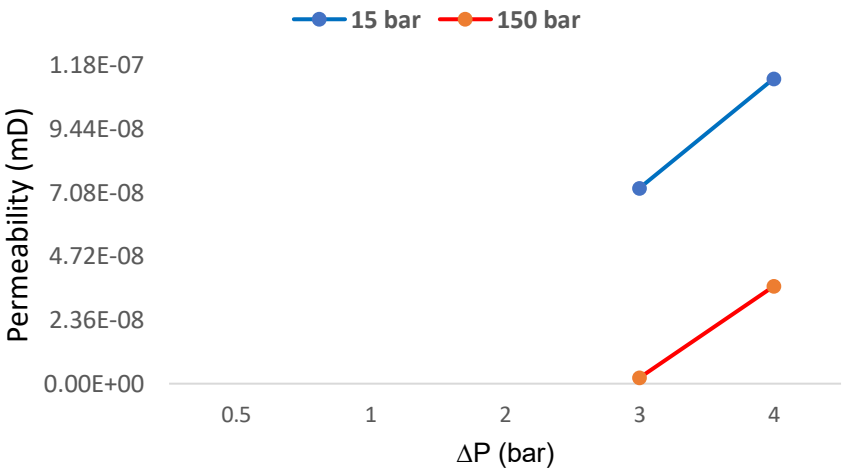

Figure 4-26: Comparison between Mancos and Marcellus Shale Samples

The permeability for both Mancos and Marcellus is less at a higher overburden pressure due to the additional compression and solidification. However, the permeability of Marcellus is higher than Mancos due to the chemical content present in the rock structure (calcium silicate), which enhances the solidification and compactness and makes the rock rather incompressible.

Table 4-17: Comparison of Mancos and Marcellus Permeability of No Fracture Sample at Same Overburden Pressure and ΔP's

Sample	Overburden Pressure	ΔP's		
		2	3	4
Mancos: No Fracture	100 bar	8.83E-07	1.44E-06	5.97E-06
	150 bar		7.24E-08	1.13E-07
Marcellus: No Fracture	100 bar	3.42E-07	3.05E-06	7.92E-06
	150 bar		2.18E-09	3.61E-08

As seen in Table 4-17, Mancos permeability at an overburden pressure of 100 bar and at ΔP = 4 bar, is 5.97E-06; at 150 bar, it is 1.13E-07. In comparison, the permeability of Marcellus at 100 bar and at the same differential pressure is 7.92E-06; at 150 bar, the permeability is 3.61E-08. The permeability of Mancos is lower than Marcellus. As a rule, Marcellus must have a higher permeability due to the higher percentage of calcium that renders the rock relatively incompressible, which helps to maintain its permeability.

Figure 4-27: Show Marcellus Shale Sample (Fracture 1)

For Marcellus Shale fracture 1, Figure 4-26 and Table 4-18 show that the increase in ΔP increases the permeability of the shale sample. Nevertheless, an increase in the overburden pressure, from 100 bar to 200 bar at ΔP = 2 bar, reduces the permeability from 2.67E-04 mD to 8.88E-06 mD.

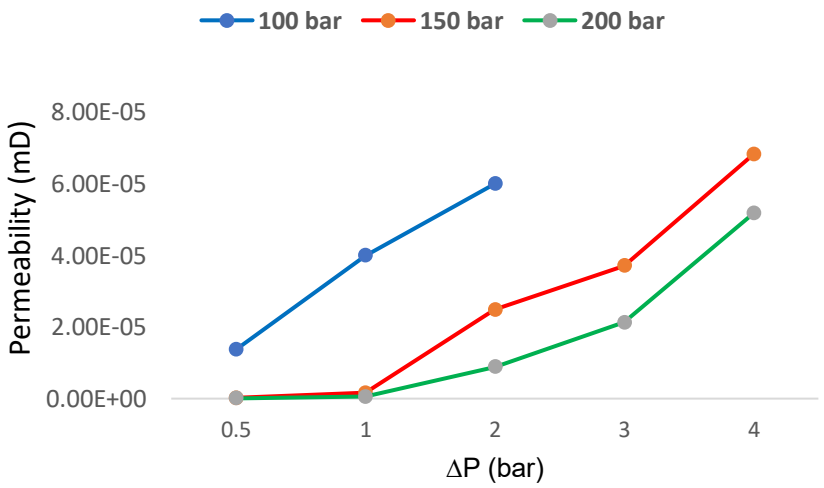

Figure 4-28: Marcellus Shale (Fracture 1) at Different Overburden Pressures

Table 4-18: Marcellus Shale Sample (Fracture 1) at 100 bar, 150 bar and 200 bar Overburden Pressure

Marcellus Shale Sample Fracture 1					
ΔP, bar	0.5	1	2	3	4
100 bar	1.37E-05	6.74E-05	2.67E-04		
150 bar	2.29E-07	1.63E-06	2.49E-05	3.71E-05	6.83E-05
200 bar	6.10E-08	5.72E-07	8.88E-06	2.13E-05	5.18E-05

Figure 4-29: Show Marcellus Shale Sample (Fracture 2)

As shown in Figure 4-28 and Table 4-19, for the fracture 2 sample, it is clear that an increase in ΔP increases the permeability of the shale sample. An increase in overburden pressure, from 100 bar to 200 bar at ΔP = 4 bar, reduces the permeability from 4.24E-04 mD to 1.82E-04 mD. Hence, the permeability decreases as the overburden pressure increases.

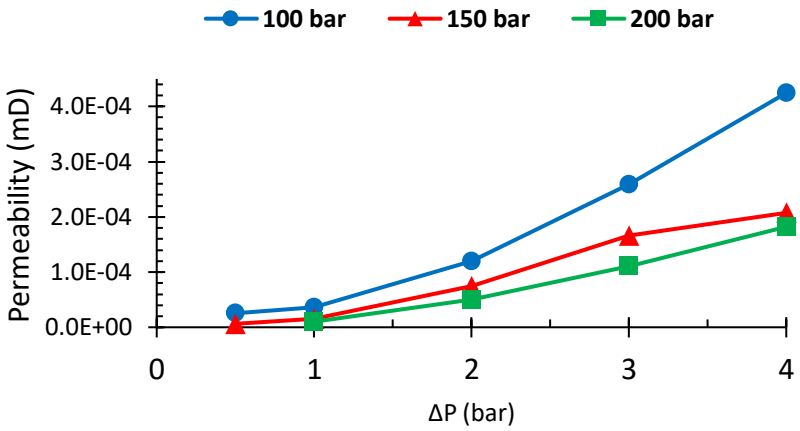

Figure 4-30: Marcellus Shale (Fracture 2) at Different Overburden Pressures

Table 4-19: Mancos Shale Sample (Fracture 2) at 100 bar, 150 bar and 200 bar Overburden Pressure

Marcellus Shale Sample Fracture 2					
ΔP, bar	0.5	1	2	3	4
100 bar	2.54E-05	3.60E-05	1.20E-04	2.59E-04	4.24E-04
150 bar	6.29E-06	1.56E-05	7.47E-05	1.66E-04	2.07E-04
200 bar		1.01E-05	5.06E-05	1.10E-04	1.82E-04

When comparing the two Marcellus fracture cases at 100 bar overburden pressure, as shown in Figure 4-31 and Table 4-20, it can be seen that increasing the ΔP increases the permeability of the shale sample.

The overburden pressure, in this case, is constant at 100 bar; however, the ΔP is directly proportional to permeability as it indicates the alteration between the inlet and outlet pressures that demonstrate that a higher ΔP will increase the flow rate.

As can be seen, for fracture 1, a ΔP of below 2 bar has greater permeability than for fracture 2, even though there are fewer vertical pathways through the shale sample. This indicates that the single vertical channels may enlarge more under an increased ΔP than the multiple channel paths, which may interact with one another and effectively reduce the permeability gap. The multiple channels appear to oppose each other and have reduced the pathway single area.

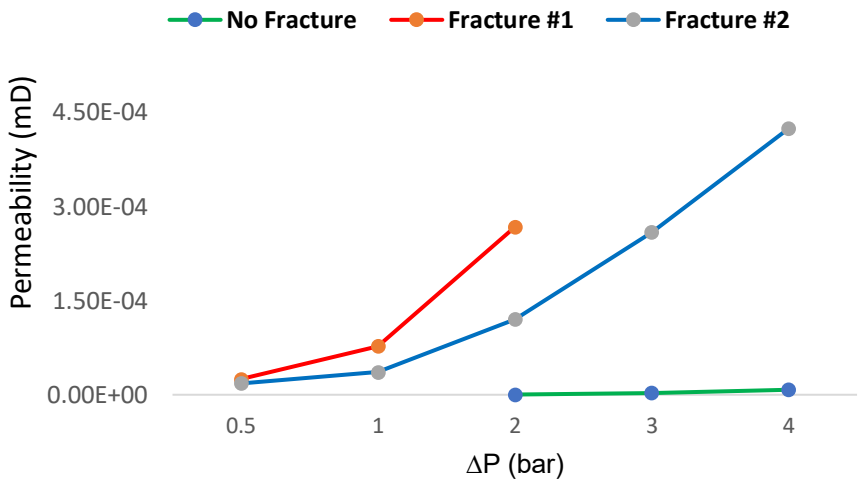

Figure 4-31: Marcellus Shale (No Fracture, Fracture 1 And Fracture 2) at 100 bar Overburden Pressure

Table 4-20: Marcellus Shale Sample (No Fracture, Fracture 1 And Fracture 2) at 100 bar Overburden Pressure

100 bar Overburden Pressure					
ΔP, bar	0.5	1	2	3	4
No Fracture			3.42E-07	3.05E-06	7.92E-06
Fracture 1	2.50E-05	7.74E-05	2.67E-04		
Fracture 2	1.80E-05	3.60E-05	1.20E-04	2.59E-04	4.24E-04

Figure 4-32 and Table 4-21 compare the permeability of the three samples at an overburden pressure of 150 bar.

For both fracture cases, the permeability is far less than at 100 bar (Figure 4-18). There is also a marked difference between the fracture types. The additional multiple paths in fracture 2 provide a greater pathway and have greater permeability than fracture 1.

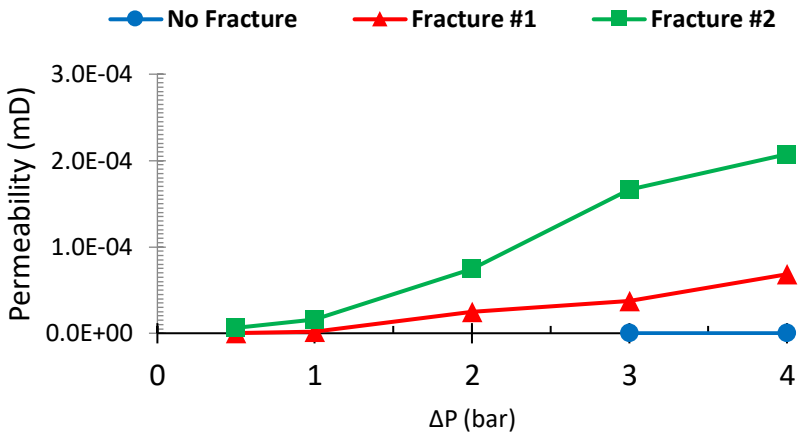

Figure 4-32: Marcellus Shale sample (No Fracture, Fracture 1 and Fracture 2) at 150 bar Overburden Pressure

Table 4-21: Marcellus Shale Sample (No Fracture, Fracture 1 And Fracture 2) at 150 bar Overburden Pressure

150 bar Overburden Pressure					
ΔP, bar	0.5	1	2	3	4
No Fracture				2.18E-09	3.61E-08
Fracture 1	2.29E-07	1.63E-06	2.49E-05	3.71E-05	6.83E-05
Fracture 2	6.29E-06	1.56E-05	7.47E-05	1.66E-04	2.07E-04

It can be seen in Figure 4-33 and Table 4-22 that the permeability is greatly reduced at an overburden pressure of 200 bar, in comparison to the overburden pressures of 100 and 150 bar (Figures 4-28 and 4-30). It also shows that the multiple vertical passageways in case 1, fracture 2 has a greater permeability than for fracture 1 and is similar in profile to the 150 bar overburden pressure case.

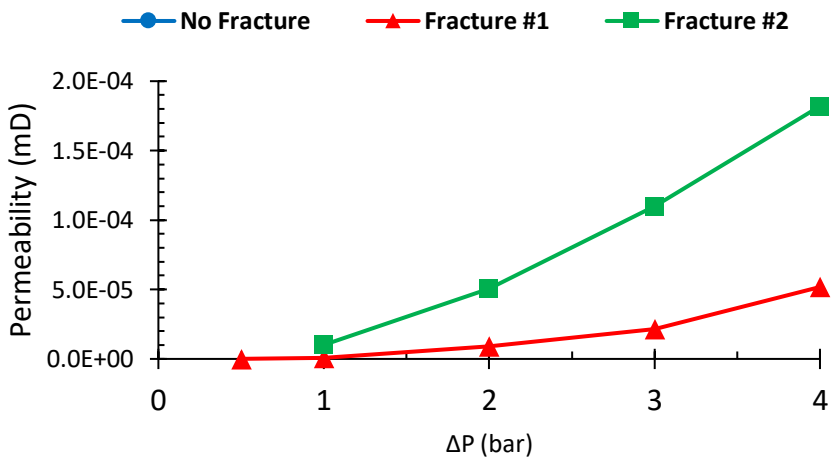

Figure 4-33: Marcellus Shale sample (Fracture 1 And Fracture 2) at 200 bar Overburden Pressure

Table 4-22: Mancos Shale Sample (No Fracture, Fracture 1 And Fracture 2) at 200 bar Overburden Pressure

200 bar Overburden Pressure					
ΔP, bar	0.5	1	2	3	4
No Fracture					
Fracture 1	6.10E-08	5.72E-07	8.88E-06	2.13E-05	5.18E-05
Fracture 2		1.01E-05	5.06E-05	1.10E-04	1.82E-04

4.7.3 Comparison of Permeability Graphs between Mancos and Marcellus Shales (recent results)

In this section, the effect of the shale type on permeability will be presented. Figure 4-34 and Table 4-23 compare the No Fracture Marcellus and Mancos Shales at an overburden pressure of 100 bar. Figure 4-34 shows that, for a ΔP of greater than 2 bar, Mancos Shale has a lower permeability than Marcellus. The graph shows that, at ΔP = 2 bar, Mancos is higher than Marcellus. At 100 bar overburden pressure, all Mancos values are less than Marcellus. This is because the geological setting type causes greater compactness in the Mancos Shale than in Marcellus.

To conclude, the difference in permeability between Mancos and Marcellus could be due to the depositional factors as better sorting increases both permeability and porosity. The gravel and coarse grain size cause irregularly high permeability and even decreased porosity. Very fine grains of silt and detrital clay yield low permeability at higher porosity ranges. A high quartz ratio can also create good permeability values even with low porosity (Lucia, 1995; Lucia, 1999; Mortensen et al., 1998) (Refer to Appendix F, page 172 for the XRF analysis values). The Marcellus Shale sample has a higher ratio of calcium (43%), which renders the rock incompressible to some extent and helps to keep the permeability higher than Mancos, which has lower calcium content (5%), (refer to Table: F3, page 181, Appendix F).

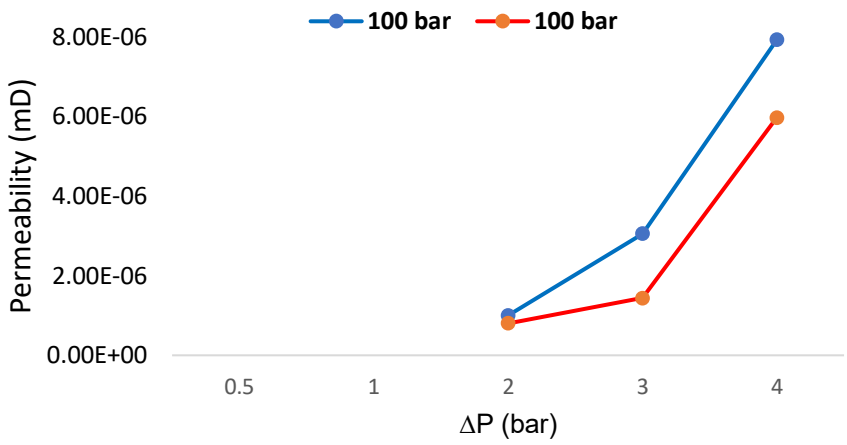

Figure 4-34: Permeability Comparison between Mancos and Marcellus Shale Samples (No Fracture)

Table 4-23: Mancos and Marcellus (No Fracture)

	Marcellus- No Fracture			Mancos- No Fracture		
ΔP	100 bar	150 bar	200 bar	100 bar	150 bar	200 bar
0.5						
1						
2	1.00E-06			8.00E-07		
3	3.05E-06	2.18E-09		1.44E-06	7.24E-08	
4	7.92E-06	3.61E-08		5.97E-06	1.13E-07	

In Figure 4-35 and Table 4-24, Mancos is noticeably greater than Marcellus, at the overburden pressure of 150 bar.

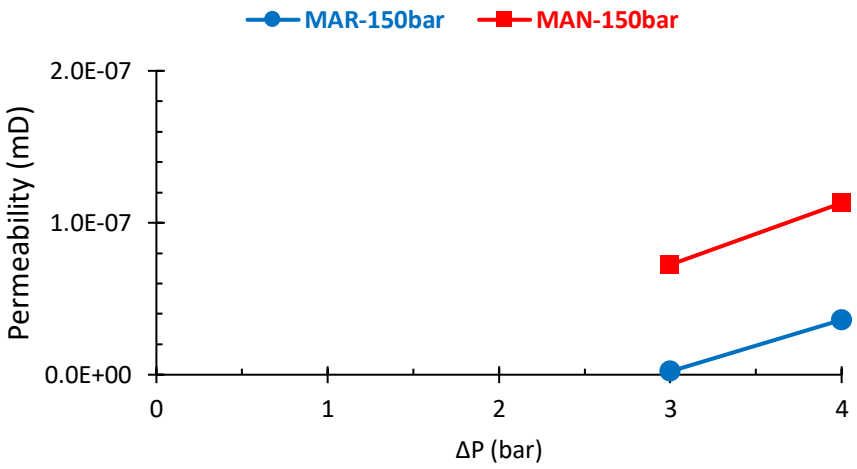

Figure 4-35: Permeability Comparison between Mancos and Marcellus Shale Samples (No Fracture)

Similar to the previous results (Figure 4-37 and Table 4-25), for ΔP = 2 bar, the permeability of Mancos is lower than Marcellus, which is linked to the geological compactness of the Mancos Reservoir area from which the sample was taken. Marcellus should have a greater permeability due to the high ratio of calcium silicate that renders the rock incompressible to some extent and helps to maintain better permeability than Mancos, which has only 5% calcium silicate, (refer to Tables: F3 & F4, pages 181-185, Appendix F).

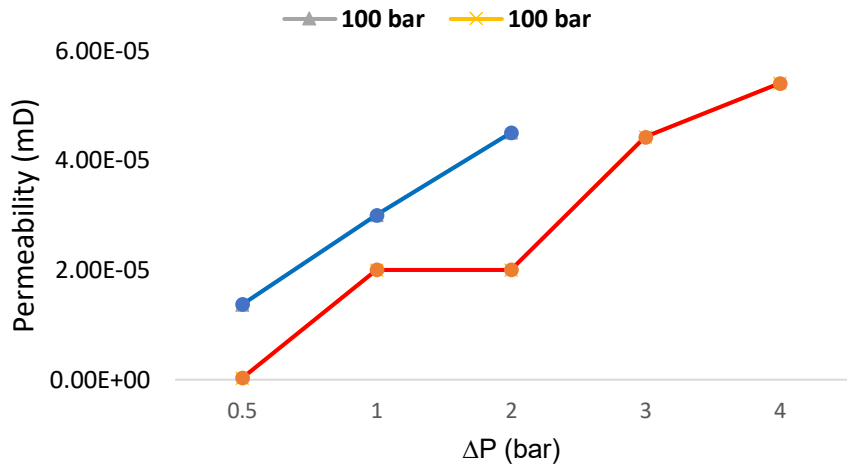

Figure 4-36: Permeability Comparison between Mancos and Marcellus Shale Samples

Table 4-24: Mancos and Marcellus (Fracture 1)

	Marcellus - Fracture 1			Mancos - Fracture 1		
ΔP	100 bar	150 bar	200 bar	100 bar	150 bar	200 bar
0.5	1.37E-05	2.29E-07	6.10E-08	3.05E-07	2.29E-07	6.10E-08
1	3.00E-05	1.63E-06	5.72E-07	2.00E-05	1.00E-06	5.72E-07
2	4.50E-05	2.60E-05	8.88E-06	2.00E-05	1.00E-05	5.51E-06
3		5.00E-05	2.13E-05	4.42E-05	4.00E-05	2.01E-05
4		7.50E-05	5.18E-05	5.40E-05	6.50E-05	5.02E-05

For fracture case 1 at 150 bar, the Marcellus Shale has a greater permeability for all ΔP's. Mancos is lower in permeability than Marcellus because it has less calcium and silicon, (refer to Table: F3, page 181, Appendix F).

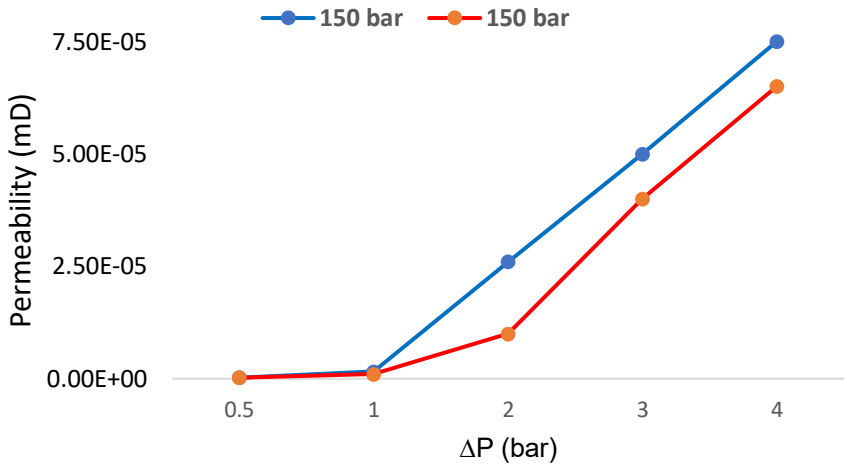

Figure 4-37: Permeability Comparison between Mancos and Marcellus Shale Samples (Fracture 1)

As can be seen in Figure 4-38, at an overburden pressure of 200 bar, the permeability is markedly similar for both the Mancos and Marcellus fracture 1 cases. At such overburden pressures, the passageways are greatly reduced.

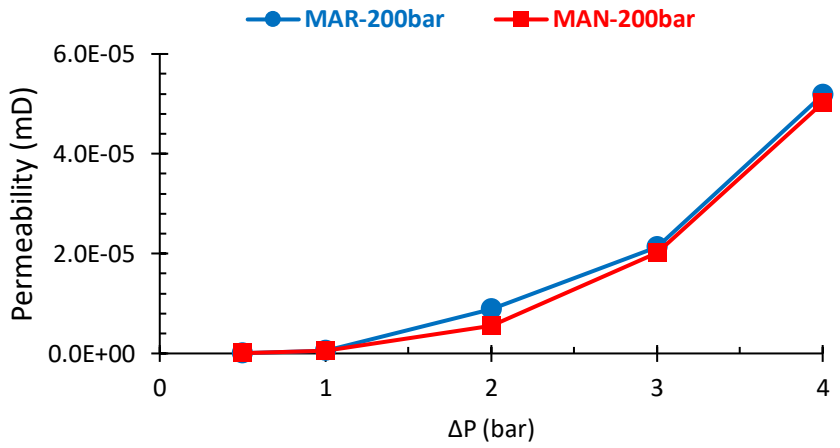

Figure 4-38: Permeability Comparison between Mancos and Marcellus Shale Sample (Fracture 1) at 200 bar Overburden Pressure.

As seen in Figure 4-39, for fracture case 2, at an overburden pressure of 100 bar, the Marcellus Shale has greater permeability for all ΔP's.

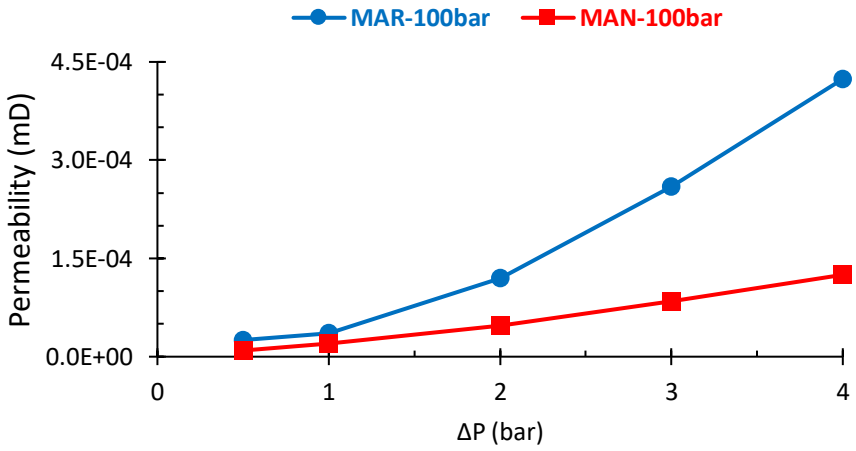

Figure 4-39: Permeability Comparison between Mancos and Marcellus Shale Sample (Fracture 2) at 100 bar Overburden Pressure

Table 4-25: Mancos and Marcellus (Fracture 2)

	Marcellus - Fracture 2			Mancos - Fracture 2		
ΔP	100 bar	150 bar	200 bar	100 bar	150 bar	200 bar
0.5	2.54E-05	6.29E-06		9.42E-06	6.87E-06	4.30E-06
1	3.60E-05	1.56E-05	1.01E-05	2.04E-05	1.30E-05	8.59E-06
2	1.20E-04	7.47E-05	5.06E-05	4.72E-05	2.89E-05	2.16E-05
3	2.59E-04	1.66E-04	1.10E-04	8.41E-05	4.57E-05	3.19E-05
4	4.24E-04	2.07E-04	1.82E-04	1.25E-04	7.16E-05	4.59E-05

At an overburden pressure 150 bar, the fracture 2 permeability results for case 1 (Figure 4-40) show that the Marcellus Shale has greater permeability than Mancos. This is consistent with previous findings, and is due to the geological compactness of the shale and the mineralogy.

The XRF analysis (in Appendix F, on page 172), the Marcellus Shale sample has a higher calcium ratio (43%) which renders the rock incompressible to some extent and helps to keep the permeability higher than Mancos, which has a lower calcium ratio (5%) (refer to Table: F3, page 181, Appendix F).

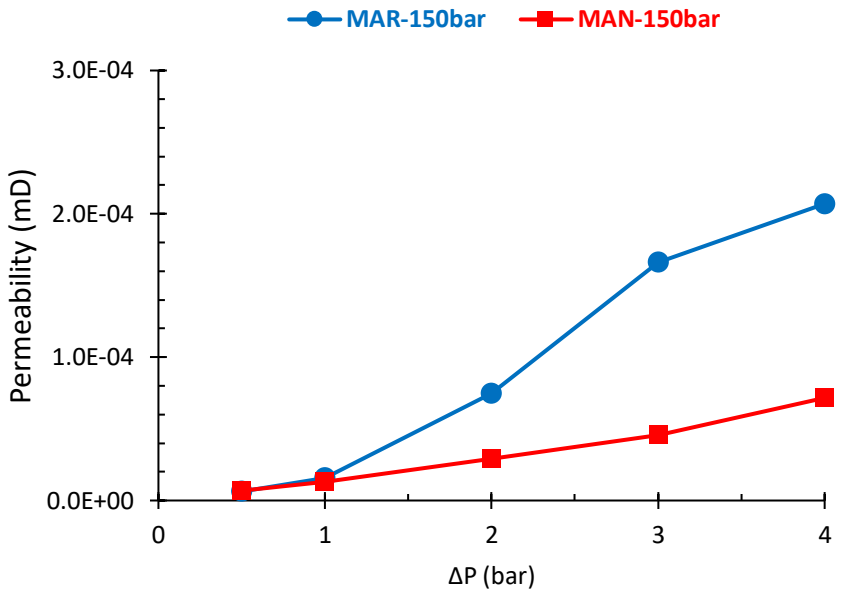

Figure 4-40: Permeability Comparison between Mancos and Marcellus Shale Samples (Fracture 2) at 150 bar Overburden Pressure

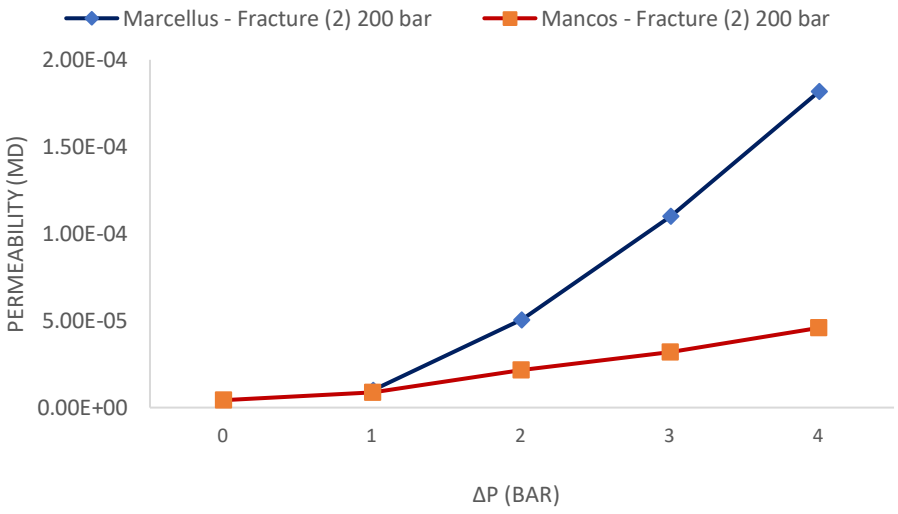

Figure 4-41: Permeability Comparison between Mancos and Marcellus Shale Samples (Fracture 2)

4.8 Chapter Summary

This chapter presented and discussed the results of the shale analysis, the porosity calculation using CT scan technique, and the permeability calculation using the Nano-Perm equipment. It compared fracture and shale types and their effects on permeability.

The main findings detailed in this chapter are:

i. Shale composition, Mancos and Marcellus: the permeability of Mancos and Marcellus is mainly determined by the hard-mineral content, for example, calcium and quartz. As a rule, Marcellus has a higher permeability due to the higher percentage of calcium (43%) that renders the rock relatively incompressible. This helps to maintain the permeability compared with Mancos at a calcium ratio of 5%, (refer to Table: F3, page 181).

ii. Porosity results for the different shales: the porosity for the unfractured Mancos is less due to the lower ratio of hard minerals, for example, calcium at 5%, which renders the rock compressible with a lower porosity. The porosity for the second set of shale samples (Marcellus) was calculated using the two methods, by liquid saturation and the CT scan, and there was a good agreement in the results.

iii. Permeability results, with respect to fracture type and shale type of the third set of Mancos and Marcellus Shale samples: At a low overburden pressure, permeability is enhanced by the fracture type; for example, complex fractures create multiple gaps and spaces within the rock for a fluid to flow through. The channels created across the rock caused various pathways to accommodate the flow. The shale type also enhances the permeability of the rock matrix, as formations differ. For example, Marcellus Shale is more permeable than Mancos due to the rock mineral content and geological setting. It should be noted that, at higher overburden pressures, the permeability may decrease with more complex fractures. This is due to fracture interaction and complex fractures, and a greater pressure drop due to the cumulated pathways.

Chapter 5 Conclusions and Recommendations

5.1 Introduction

The author researched the geomechanical properties of shale rock from different reservoirs, Barnett, Eagle Ford, Mancos and Marcellus. Only the Mancos and Marcellus core samples were induced with complex fractures and the permeability measured for a range of overburden pressures, simulating well depths at 345m, 690m, 1034m and 1379m.

5.2 Conclusions

The XRF analysis for Barnett Shale shows that the major elemental composition is calcium (Ca), 41% and silicon (Si), 3% and the higher elemental percentages for Eagle Ford Shale are calcium (Ca), 28% and silicon (Si), 16%. Other elements, for instance, magnesium (Mg), iron (Fe), sulphur (S) and titanium (Ti), can also be observed but at lesser contents. For Marcellus, calcium (Ca), silicon (Si) and aluminium (Al) are the principal elements, constituting a ratio of 45% of the total weight. Extra elements, such as potassium (K), sulphur (S) and iron (Fe), can be also detected but at reduced percentages.

The CT scan technique was used to calculate the porosity, crack width and crack length of the fractured shale samples. The unfractured shale samples from Barnett, Eagle Ford, Mancos and Marcellus Shales were characterised by using the XRF spectrometer to understand the nature of the composition of these samples. The porosity of the first set of shale samples (Eagle Ford at 5.08%, Mancos at 4.45% and Marcellus at 5.76%) was presented in Table 4-6. There was also good agreement in the porosity results for the two different techniques used, namely the CT scan and the liquid saturation method (shown in Table 4-10).

It was found that, for the Mancos Shale (the third set of shale samples), the more complex fracture had a greater permeability at ΔP's of less than 2 bar and at an overburden pressure of 100 bar. The greater number of passageways through which the gas can flow can explain this. However, above a ΔP of 2 bar and with an overburden pressure of 150 bar, the less complex fracture had greater permeability. One explanation for this is that the overburden

pressures may reduce the gaps between the fractures, and the increased ΔP helps the fractures to interfere with each other to effectively reduce the pore space between them.

For the Marcellus Shale (the third set of shale samples), it was found that overburden pressures of more than 150 bar and for all ΔP's, the more complex fracture had a greater permeability. It was also shown that the Marcellus Shale had a greater permeability compared with Mancos. This was due to the different chemical composition, such as calcium (Ca) and silicon (Si) (detailed in Appendix F, on page 172).

5.3 Recommendations

Once one knows the effects of complex fracture orientation and shale reservoir grain size on permeability, for example, through coring and testing, the engineer/geologist can predict the load effect on this type of formation. Consequently, other geomechanical properties and flow rates can also be predicted. The researcher recommends expanding this research by carrying out more experiments on this topic by using other approaches to cover mathematical modelling.

The CT scan data could also be used to construct a geomechanical model of the shale, which could then be input into a computational fluid dynamics (CFD) package to compare the permeability results from the experiment with CFD. Additional fracture types could also be investigated and fracture interactions could also be predicted.

REFERENCES

Alabbad, E. A. and Olson, J. E. (2016). Examining the geomechanical implications of pre-

existing fractures and simultaneous-multi-fracturing completions on hydraulic fractures: experimental insights into fracturing unconventional formations. SPE annual technical conference and exhibition, 26-28 September, Dubai, UAE, doi:10.2118/181327-MS.

Al-Anazi B.D., Algarni, M. T., Tale, M. and Almushiqeh, I. (2011). Prediction of Poisson's Ratio and Young's Modulus for hydrocarbon reservoirs using alternating conditional expectation algorithm. SPE Middle East oil and gas show and conference, 25-28 September, Manama, Bahrain. doi:10.2118/138841-MS.

Ambrose, R.J., Hartman, R.C., Campos, M.D., Akkutlu, I.Y., Sondergeld, C.H. (2010). New pore-scale considerations for shale gas in place calculations. SPE unconventional gas conference, 23-25 February, Pittsburgh, Pennsylvania, USA.

Aplin, A.C and MacQuaker, J.H.S. (2011). Mudstone diversity: origin and implications for the source, seal, and reservoir properties in petroleum systems. AAPG Bulletin, 95(12): 2031–2059.

Aydin, A. (2009). ISRM Suggested method for determination of the Schmidt hammer rebound hardness: revised version. International Journal of rock mechanics and mining sciences, 46(3), 627-634.

Barenblatt, G.I., Zheltov, I.P. and Kochina, I.N. (1960). Basic concepts in the theory of seepage of homogeneous liquids in fissured rocks [Strata], journal of applied mathematics and mechanics 24:1286-1303.

Barton, N., Bandis, S. and Bakhtar, K. (1985). Strength, deformation and conductivity coupling of rock joints. International Journal of rock mechanics and mining science, 22: 121-140.

Bartuska, J.E., Pechiney, J.J., Leonard, R.S. and Woodroof, R.A. (2012). Optimising completion designs for horizontal shale gas wells using completion diagnostics, SPE Americas unconventional resources conference, 5-7 June, Pittsburgh, Pennsylvania USA.

Belytschko, T., and T. Black, (1999). Elastic crack growth in finite elements with minimal remeshing: International journal for numerical methods in engineering, 45(5): 601–620, doi:10.1002/(SICI)1097-0207(19990620)45:53.0.CO;2-S.

Blanton, T.L. (1982). An experimental study of interaction between hydraulically induced and pre-existing fractures. in SPE/DOE unconventional gas recovery symposium, Pittsburg, Pennsylvania: SPE paper 10847.

Blanton, T.L. (1986). Propagation of hydraulically and dynamically induced fractures in naturally fractured reservoirs. SPE unconventional gas technology symposium, 18-21 May, Louisville, Kentucky. doi:10.2118/15261-MS

Bock, H.F., Foruria, V. (1984). A recoverable borehole slotting instrument for in-situ stress measurements in rock not requiring overcoring. International symposium on field measurement in geomechanics, Zurich, pp. 15–29.

Britt and Schoeffler, (2009). The Geomechanics of a Shale Play: What Makes a Shale Prospective, SPE Eastern Regional Meeting, 2009-01-01, 2009, Society of Petroleum Engineers (2009)

Britt, L. K. and Smith, M. B. (2009). Horizontal well completion, stimulation optimisation, and risk mitigation. SPE eastern regional meeting, 23-25 September, Charleston, West Virginia, USA. doi:10.2118/125526-MS.

Broadhead, R.F. (2015). The Upper Mancos Shale in the San Juan Basin: Three plays, conventional and unconventional: American Association of Petroleum Geologists, Search and Discovery, Article no. 10791, 39 p.

Bruner, K. R. and Smosna, R. (2011). A comparative study of the Mississippian Barnett Shale, Fort Worth Basin, and Devonian Marcellus Shale, Appalachian basin. DOE/NETL report no. 2011/1478, US DOE, Pittsburgh.

Cai, M. (2000). The principle and technique of in-situ stress measurement. Beijing: science press. (in Chinese)

Campbell, C. J., and Laherrere, J. H. (1998). The end of cheap oil, scientific American, 278(3): 78–83.

Centurion, S. M. (2011). Eagle Ford Shale: A multistage hydraulic fracturing, completion trends and production outcome study using practical data mining techniques. SPE eastern regional meeting, 17-19 August, Columbus, Ohio, USA, doi:10.2118/149258-MS

Coates, D.F. (1967). Rock mechanics principles, geoscience abstracts, 8 (12): 97

Collins, R. E., & Jordan, J. K. (1961). Porosity and permeability distribution of sedimentary rocks. Society of petroleum engineers.

Crawford, B. R., Myers, R. D., Woronow, A., Faulkner, D. R. and Rutter, E. H. (2002). Porosity-permeability relationships in clay-bearing fault gouge. SPE/ISRM rock mechanics conference, 20-23 October, Irving, Texas, doi:10.2118/78214-MS.

Daneshy, A.A. (1974). Hydraulic fracture propagation in the presence of plane of weakness. SPE European spring meeting, 29-30 May, Amsterdam, Netherlands.

Ding, W. L., Xu C. C. and Jiu, K. (2011). The research progress of shale fractures. Advances in earth science, 26: 135–144

Er, C., Li, Y., Zhao, J., Wang, R., Bai, Z ., Han, Q. (2016). Pore formation and occurrence in the organic-rich shales of the Triassic Chang-7 member, journal of natural gas science, 1(6): 435-444

Ezisi, I., Hale, B. W., Watson, M. C. and Heinze, L. (2012). Assessment of probabilistic parameters for Barnett Shale recoverable volumes. SPE hydrocarbon economics and evaluation symposium, 24-25 September, Calgary, Alberta, Canada. doi:10.2118/162915-MS.

Fatt, I., and Davis, D. H. (1952). Reduction in permeability with overburden pressure. journal of petroleum technology. 4(12) doi:10.2118/952329-G.

Fitton, G., (1997). X-Ray fluorescence spectrometry, in R. Gill (ed.), modern analytical geochemistry: an introduction to quantitative chemical analysis for earth, environmental and material scientists: Addison Wesley Longman, UK.

Gandossi, L. and Von Estdorff, U. (2013). An overview of hydraulic fracturing and other formation stimulation technologies for shale gas production. Joint research centre of the European commission: Luxembourg. doi: 10.2790/379646.

Gharahbagh, A. E., & Fakhimi, A. (2011). The Effect of Pore Size On Tensile And Compressive Strengths of Rock: A Bonded Particle Simulation. American Rock Mechanics Association.

Gutierrex, M. and Lewis, R. W. (1998). The role of geomechanics in reservoir simulation. SPE/ISRM rock mechanics in petroleum engineering, 8-10 July, Trondheim, Norway. doi:10.2118/47392-MS.

Haimson, B. C. and Cornet, F. H. (2003). ISRM suggested methods for rock stress estimation part 3: hydraulic fracturing (HF) and/or hydraulic testing of pre-existing fractures (HTPF). international journal of rock mechanics and mining science, 40 (7/8): 1011–1020.

Haimson, B. and Fairhurst, C. (1967). Initiation and extension of hydraulic fractures in rocks. society of petroleum engineers journal. 7(3). doi:10.2118/1710-PA.

Hall, R., Bertram, R., Gonzenbach, G., Gouveia, J., Hale, B., Lupardus, P., McDonald, P., Vail, B. and Watson, M. (2010). Guidelines for the practical evaluation of undeveloped reserves in resource plays. Monograph series, SPEE, Houston, Texas, 3: 1-39.

Hall, H. N. (1953, January 1). Compressibility of Reservoir Rocks. Society of Petroleum Engineers. doi:10.2118/953309-G.

Harbor, R.L. (2011). Facies characterization and stratigraphic architecture of organic-rich mudrocks, Upper Cretaceous Eagle Ford formation, South Texas (M.S. thesis), University of Texas, Austin

Holt, R. M., Nes, O.-M., Stenebråten, J. F. and Fjær, E. (2012). Static vs. Dynamic behaviour of shale. ARMA 12-209, presented at the 46th US rock mechanics/geomechanics symposium, Chicago, 24-27 June.

Huang, J., Safari, R., Mutlu, U., Burns, K., Geldmacher, I., McClure, M., and Jackson, S. (2014). Natural-hydraulic fracture interaction: microseismic observations and geomechanical predictions. unconventional resources technology conference, 25-27 August, Denver, Colorado, USA

Jin, X., Shah, S. N., Roegiers, J.-C. and Zhang, B. (2014). Fracability evaluation in shale reservoirs - an integrated petrophysics and geomechanics approach. SPE hydraulic fracturing technology conference, 4-6 February, the Woodlands, Texas, USA doi:10.2118/168589-MS.

Jones, T. A., Wooten, S. and Kaluza, T. J. (1988). Single-phase flow through natural fractures. SPE annual technical conference and exhibition, 2-5 October, Houston, Texas. doi:10.2118/18175-MS.

Kalnicky, D.J., Bernick, M., Kaelin, L., Singhvi, R. and Prince, G. (1995). Optimization of fundamental parameters methods for analysis of hazardous materials with field-portable XRF analysers, in proceedings of an international symposium on field screening methods for hazardous wastes and toxic chemicals, VIP-47, Vol. 2, air and waste management association, Pittsburgh, PA, pp. 1103–1105.

King, G. E. (2012). Hydraulic Fracturing 101: what every representative, environmentalist, regulator, reporter, investor, university researcher, neighbour and engineer should know about estimating frac risk and improving frac performance in unconventional gas and oil

wells. Paper SPE 152596 presented at the SPE hydraulic fracturing technology conference, Woodlands, Texas, USA.

Kumar, N. Varughese, A. Kapoor, V. Dhawan A. (2004). In-situ stress measurement and its application for hydro-electric projects—an Indian experience in the Himalayas, international journal of rock mechanics and mining sciences and geomechanics, 41(1): 195-200.

Kundert, D. P., & Mullen, M. J. (2009, January 1). Proper Evaluation of Shale Gas Reservoirs Leads to a More Effective Hydraulic-Fracture Stimulation. Society of Petroleum Engineers. doi:10.2118/123586-MS

Kutter, H.K. and Fairhurst, C. (1971). On the fracture process in blasting. International journal of rock mechanics and mining sciences and geomechanics. 8(3): 181-202.

Laudeman, S. K. and Ershaghi, I. (1981). Pressure buildup analysis in a naturally fractured shale reservoir, SPE annual technical conference and exhibition, 4-7 October, San Antonio, Texas

Lestz, R. S., Wilson, L., Taylor, R. S., Funkhouser, G. P., Watkins, H. and Attaway, D. (2007). Liquid petroleum gas fracturing fluids for unconventional gas reservoirs. Journal of Canadian petroleum technology. 46(12). doi:10.2118/07-12-03.

Li, C., Chen, X. and Du, Z. (2004). A new relationship of rock compressibility with porosity. SPE Asia Pacific oil and gas conference and exhibition, 18-20 October, Perth, Australia. doi:10.2118/88464-MS.

Liao, H. J., Han, J., Sugiyam, M. and Akaishi, M. (2009). Study on stress-strain relationship based on strain space. ISRM international symposium on rock mechanics - SINOROCK 2009, 19-22 May, the University of Hong Kong, China

Lorenz, J. C. (1999). Stress-sensitive reservoirs. Journal of petroleum technology. 51(1). doi:10.2118/50977-JPT.

Lucia, F.J. (1999). Carbonate reservoir characterization. Berlin: Springer.

Lucia, F.J. (1995). Rock-fabric/petrophysical classification of carbonate pore space for reservoir characterisation. American association of petroleum geologists bulletin. 79(9): 1275-1300.

Luo, M., Arihara, N., & Evans, B. J. (2003). 3-D Analysis of Complex Fracture Systems. Society of Exploration Geophysicists.

McNeal, J., Huhndorf, S., Craig, J., and Atashbari, V. (2017). Characterising Alaska overburden. SPE Western regional meeting, 23-27 April, Bakersfield, California doi:10.2118/185739-MS.

Mgaya, P., Hosoda, T., and Kishida, K. (2006). Fluid flow in measured apertures of a single rock fracture: a depth-averaged model and the local cubic law simulations. Golden rocks 2006, the 41st U.S. Symposium on rock mechanics (USRMS), 17-21 June, Golden, Colorado

Mijrata, S., Miyoshi, T., Matsuoka, T., Saito, T. and Ashida, Y. (2002). Visualisation of the channel flow through a single fracture. ISRM international symposium - EUROCK 2002, 25-27 November, Madeira, Portugal.

Mokhtari, M., Alqahtani, A. A. and Tutuncu, A. N. (2013). Failure behaviour of anisotropic shales. 47th U.S. Rock mechanics/geomechanics symposium, 23-26 June, San Francisco, California.

Montgomery, S. L., Jarvie, D. M., Bowker, K. A. and Pollastro, R. M. (2005). Mississippian Barnett Shale, Fort Worth basin, north-central Texas: gas-shale play with multi-trillion cubic foot potential, AAPG bulletin, 89(2): 155-175.

Mortensen, J., Engstrom, F., and Lind, I. (1998). The relation among porosity, permeability, and specific surface of chalk from the Gorm Field, Danish North Sea. Society of petroleum engineers, 1(3): 245-251. doi:10.2118/31062-PA

Mullen, J. (2010). Petrophysical characterisation of the Eagle Ford shale in South Texas. paper CSUG/SPE 138145 presented at the Canadian unconventional resources and international petroleum conference, Calgary, Alberta, Canada, 19-21 October.

Muralidharan, V., Chakravarthy, D., Putra, E. and Schechter, D. S. (2004). Simulation of fluid flow through rough fractures. SPE annual technical conference and exhibition, 26-29 September, Houston, Texas. doi:10.2118/89941-MS.

Newman, G. H. (1973). Pore-volume compressibility of consolidated, friable, and unconsolidated reservoir rocks under hydrostatic loading. Journal of petroleum technology. 25(2). doi:10.2118/3835-PA

Nilson, R.H., W.J. Proffer, and R.E. Duff (1985). Modelling of gas-driven fractures induced by propellant combustion within a borehole. International journal of rock mechanics and mining sciences and geomechanics, 22(1): 3-19.

Oda, M. (1985). Permeability tensor for discontinuous rock masses. Geotechnique. 35: 483-95.

Ogolo, N. A., Akinboro, O. G., Inam, J. E., Akpokere, F. E. and Onyekonwu, M. O. (2015). Effect of grain size on porosity revisited. SPE Nigeria annual international conference and exhibition, 4-6 August, Lagos, Nigeria. doi:10.2118/178296-MS.

Okubo, K., Mikada, H., Goto, T.-N. and Takekawa, J. (2013). Stress distribution in fractured medium and fracture propagation due to formation pressure changes. Society of exploration geophysicists.

Olson, J. E., Laubach, S. E. and Lander, R. H. (2004). Improving fracture permeability prediction by combining geomechanics and diagenesis. Gulf rocks 2004, the 6th North America rock mechanics symposium (NARMS), 5-9 June, Houston, Texas

Potts, P.J. (1987). A handbook of silicate rock analysis, Chapman and Hall, London.

Raeini, A.Q., Blunt, M.J. and Bijeljic, B. (2012). Modelling two-phase flow in porous media at the pore scale using the volume-of-fluid method. Journal of computational Physics, 231(17): 5653-5668.

Rahman, M. M., Aghighi, M. A., Rahman, S. S. and Ravoof, S. A. (2009). The interaction between induced hydraulic fracture and pre-existing natural fracture in a poro-elastic environment: effect of pore pressure change and the orientation of natural fractures. Asia Pacific oil and gas conference and exhibition, 4-6 August, Jakarta, Indonesia. doi:10.2118/122574-MS.

Reed, R. M., and S. C. Ruppel, (2012). Pore morphology and distribution in the Cretaceous Eagle Ford shale, south Texas, USA: Gulf coast association of geological societies transactions, 62: 599–603

Rickman, R., Mullen, M. J., Petre, J. E., Grieser, W. V., and Kundert, D. (2008). A practical use of shale petrophysics for stimulation design optimisation: all shale plays are not clones of the Barnett Shale. SPE annual technical conference and exhibition, 21-24 September, Denver, Colorado, USA. doi:10.2118/115258-MS.

Safari, M. R., Gandikota, R., Mutlu, U., Ji, M., Glanville, J. and Abass, H. (2013). Pulsed fracturing in shale reservoirs: geomechanical aspects, ductile-brittle transition and field implications. Unconventional resources technology conference, 12-14 August, Denver, Colorado.

Safari, R., Huang, J., Mutlu, U. and Glanville, J. (2014). 3D analysis and engineering design of pulsed fracturing in shale gas reservoirs. 48th U.S. Rock mechanics/geomechanics symposium, 1-4 June, Minneapolis, Minnesota.

Safari, R., Lakshminarayanan, S., Huang, J., Mutlu, O., Jayakumar, R., Christian, S. M. and Rai, R. (2013). Integrating reservoir and geomechanical models to compare the productivity of shale reservoirs using different fracture techniques. Society of petroleum engineers. SPE unconventional resources conference and exhibition-Asia Pacific, 11-13 November, Brisbane, Australia. doi:10.2118/167105-MS.

Sarker, R. and M. Batzle. (2010). Anisotropic elastic moduli of the Mancos B shale-an experimental study. 2010 SEG Annual Meeting, 17-22 October, Denver, Colorado.

Settari, A., Ro, Y. and Jha, K.N. (1992). Coupling of a fracture mechanics model and a thermal reservoir simulator for Tar Sands, journal of Canadian petroleum technology, 31(9), 20, doi:10.2118/92-09-02

Shah, S. N., Vincent, M. C., Rodriquez, R. X., & Palisch, T. T. (2010, January 1). Fracture Orientation And Proppant Selection For Optimizing Production In Horizontal Wells. Society of Petroleum Engineers. doi:10.2118/128612-MS

Siddiqui, S. and Khamees, A. A. (2004). Dual-energy CT-scanning applications in rock characterisation. SPE annual technical conference and exhibition, 26-29 September, Houston, Texas. doi:10.2118/90520-MS.

Snow, D.T. (1969). Anisotropy permeability of fractured media, water resource research. 5:1273-1289.

Soeder, D. J. (1988). Porosity and permeability of eastern Devonian gas shale. SPE formation evaluation. 3(1). doi:10.2118/15213-PA.

Stefik, R. and Paulson, K. (2010). When unconventional becomes conventional. Journal of Canadian petroleum technology. 50(11/12). doi:10.2118/136863-MS.

Stegent, N. A., Wagner, A. L., Mullen, J. and Borstmayer, R. E. (2010). Engineering a successful fracture-stimulation treatment in the Eagle Ford shale. Tight gas completions conference, 2-3 November, San Antonio, Texas, USA. doi:10.2118/136183-MS.

Takahashi, T. and Tanaka, S. (2012). Rock physics model for static Young's Modulus and compressive strength of soft sedimentary rocks. 2012 SEG annual meeting, 4-9 November, Las Vegas, Nevada. doi:10.1190/segam2012-0867.1.

Torsaeter, M., Vullum, P. E. and Nes, O.-M. (2012). Nanostructure vs. macroscopic properties of Mancos Shale. SPE Canadian unconventional resources conference, 30 October-1 November, Calgary, Alberta, Canada. doi:10.2118/162737-MS.

Tsang, Y. W. and Witherspoon, P. A. (1981). The hydromechanical behaviour of a deformable rock fracture subject to normal stress. Journal of geophysical research. 86: 9287-9298.

US EPA/ERT, (1991). Field portable x-ray fluorescence, quality assurance technical information bulletin, 1(4), May.

Villamor Lora R. (2015). Geomechanical characterisation of Marcellus Shale. (MSc thesis). University of Vermont, Vermont. Accessed on: 10 October 2017, from: https://search.proquest.com/

Wade, A. C. and Bilgesu, H. I. (2012). The impact of hydraulic fracture and subsequent increased production due to in-situ stress changes in the Marcellus Shale. SPE eastern regional meeting, 3-5 October, Lexington, Kentucky, USA. doi:10.2118/161354-MS.

Walsh, J. B. (1981). Effect of pore pressure and confining pressure on fracture permeability. International journal of rock mechanics and mining sciences and geomechanics. 18: 429-435.

Wang, G. and Weaver, J. S. (1997). The initial stress states and fluid injection induced overburden instability. Annual technical meeting, June 8-11, Calgary, Alberta. doi:10.2118/97-120.

Warpinski, N.R. and Teufel, L.W. (1987). Influence of geologic discontinuities on hydraulic fracture propagation. Journal of petroleum technology, 39(2): 209-220.

Warpinski, N. R., Mayerhofer, M. J., Vincent, M. C., Cipolla, C. L., & Lolon, E. P. (2009). Stimulating Unconventional Reservoirs: Maximizing Network Growth While Optimizing Fracture Conductivity. Society of Petroleum Engineers. doi:10.2118/114173-PA

Warpinski, N.R., Mayerhofer, M.J., Vincent, M.C., Cipolla, C.L. and Lolon, E.P. (2008). Stimulating unconventional reservoirs: maximising network growth while optimising fracture conductivity. Paper SPE 114173 presented at unconventional reservoirs conference, Keystone, Colorado, USA, 10-12 February.

Witherspoon, P.A., Wang J.S.Y., Iwai, K. and Gale, J.E. (1980). The validity of cubic law for fluid flow in a deformable rock fracture. Water resource research. 16:1016-1024.

Wolhart, S., Davis, E., Roadarmel, W., & Wright, C. (2005, January 1). Reservoir Deformation Monitoring to Enhance Reservoir Characterization And Management. Society of Exploration Geophysicists.

Wright, C. A. and Conant, R. A. (1995). Hydraulic fracture reorientation in primary and secondary recovery from low-permeability reservoirs. SPE annual technical conference and exhibition, 22-25 October, Dallas, Texas. doi:10.2118/30484-MS.

Youn, D. and Gutierrez, M. (2011). Effect of fracture distribution on permeability of fractured rock masses. American rock mechanics association. 45th U.S. Rock mechanics/geomechanics symposium, 26-29 June, San Francisco, California.

Zamirian, M., Aminian, K. and Ameri, S. (2016). Measuring Marcellus Shale petrophysical properties. SPE western regional meeting, 23-26 May, Anchorage, Alaska, USA. doi:10.2118/180366-MS.

Zhi, Y. and Ahmad, G. (2016). Deformation properties of saw-cut fractures in Barnett, Mancos and Pierre shales. American rock mechanics association. 50th U.S. Rock mechanics/geomechanics symposium, 26-29 June, Houston, Texas.

Appendix A: Literature Review

No	Year	Author(s)	Paper Title	Description (Theory or Experiment or Both)	Comments
1	2011	Al-Anazi, B.D., Algarni, M.T., Tale, M., and Almushiqeh, I.	"Prediction of Poisson's Ratio and Young's Modulus for Hydrocarbon Reservoirs Using Alternating Conditional Expectation Algorithm".	Conducted a study on the prediction of Poisson's Ratio and Young's Modulus for hydrocarbon reservoirs using alternating conditional expectation algorithm. Shear modulus, μ, is the ratio between shear stress, σshear and shear strain εshear: $\text{shear modulus } (\mu) = \frac{\sigma_{\text{shear}}}{\varepsilon_{\text{shear}}}$ $\text{shear stress } (\sigma_{\text{shear}}) = \frac{\text{force (F)}}{\text{Area (A)}}$ $\text{Shear strain } (\varepsilon_{\text{shear}}) = \frac{\text{deformation } (\Delta L)}{\text{original length}(L)}$	The alternating conditional expectation (ACE) algorithm method used to build Poison's Ratio and Young's Modulus is incomplete because the author overlooked many significant affecting factors, such as geological studies to compare different rock deposits. In addition, the equations he used to correlate Poisson's Ratio and Young's Modulus are subject to error due to long exponential inputs. They overlooked the quasi-brittle materials, for example, rock that contains pores, micro-cracks and flaws which are arbitrarily distributed inside the material that affects Poisson's Ratio and Young's Modulus values.

2	1961	Collins, R.E. and Jordan, J.K.	"Porosity and Permeability Distribution of Sedimentary Rocks".	Conducted a study on the porosity and permeability distribution of sedimentary rocks. The rocks' permeability is a measure of the resistance to the fluid flow through them. Elevated permeability indicates that fluid passes via the rock more easily. Permeability and porosity, in general, are decreased when depth is increased due to compaction. This is because of the increasing confining pressure and load from the overlying burden of the sedimentation/new rocks.	The study was only random because there was no clear link between porosity and permeability, but sometimes the correlation was only accidental and rare. Porosity is not always effective. Porosity can be much more lager where there was only very small permeability or even zero porosity.
3	1981	Laudeman, S.K. and Ershaghi, I.	"Pressure Buildup Analysis in a Naturally Fractured Shale Reservoir".	They have researched parameters of pressure, confining, differential and in-situ stresses and the relationship between these stresses and permeability, porosity. There should be additional performing pressure transient tests for their potential in providing quantitative estimates of	The authors overlooked experimental and simulation work. They concentrated on microstructure more than anything else. Also, they did not include geological effects and geometry. They depended only on well logs, which are not enough and may be subject to errors. They could have conducted more

				significant reservoir properties, for example, effective porosity and permeability.	pressure transient tests so as to provide a quantitative evaluation of significant geomechanical reservoir properties, for example, effective total porosity and permeability.
4	2009	Liao, H.J., Han, J., Sugiyam, M., and Akaishi, M.	"Study on Stress-strain Relationship Based on Strain".	Conducted a study on stress-strain relationship based on strain space. The quantity of stress that may be applied prior to the rock shift to the next form of deformation relies on the rock type, composition, temperature, the time the rock is kept under stress, and the rock location.	The authors restricted their study to soft rock. These results are applicable only to soft rock conditions. They studied the condition of consolidated triaxial tests. They could have generalised the study to cover other conditions of rocks, for example, undrained and unconsolidated triaxial tests. They could have compared stresses at different depths.
5	2013	Safari, R., Lakshminarayan A.N., S., Huang, J., Mutlu, O., Jayakumar, R.,	"Integrating Reservoir and Geomechanical Models to Compare the Productivity of	Conducted a study on integrating reservoir and geomechanical models to compare the productivity of shale reservoirs using different fracture techniques. By applying the pressure load, a ductile-brittle transition would be set off with some	The drawbacks of the hydraulic fracturing method are that the 20-30% of used water in the injection operation is only recoverable when cleaning up. This sheds doubt over the fracture efficiency, and the overbalanced pressure;

		Christian, S.M., Rai, R.	Shale Reservoirs Using Different Fracture Techniques".	fractures spreading out from the borehole. The fracturing load is utilised in the period of milliseconds to initiate and lengthen multiple fractures laterally from the borehole.	furthermore, fracturing could damage the fracture sand face. Moreover, Pulsed Gas Fracturing has been overlooked. This might be the best technique to apply in the future as it makes the clean-up operation easier and quicker.
6	2012	Takahashi, T., and Tanaka, S.	"Rock Physics Model for Static Young's Modulus and Compressive Strength of Soft Sedimentary Rocks".	Conducted a study on rock physics model for static Young's Modulus and compressive strength of soft sedimentary rocks. Young's Modulus, E, is the ratio between the stress, σzz, and the strain, εzz, or the deformation caused by this stress, as shown in the equations below: $$E = \frac{\sigma_{zz}}{\varepsilon_{zz}}$$ $$\text{Young's Modulus} = \frac{\text{Stress}}{\text{Strain}}$$ $$= \frac{P}{\Delta L/L}, \text{ psi}$$	The paper reviewed only Young's Modulus and the compressive strength of sedimentary rocks by including friction and frictionless grain contacts to model static Young's Modulus when a larger strain quantity is applied. The authors could have included other parameters, such as tectonic effects and natural confines, for example, valleys and mountains.

7	2014	Jin, X., Shah, S. N., Roegiers, J.-C., and Zhang, B.	"Fracability Evaluation in Shale Reservoirs - An Integrated Petrophysics and Approach".	Conducted a study on a fracability evaluation in shale reservoirs - an integrated petrophysics and geomechanics approach. Brittleness is considered one of the most significant mechanical properties of rock (Jarvie et al., 2007). It is presumed that a formation that contains high brittleness is simple to fracture (Rickman et al., 2008), but this presumption is not always right as the formation of higher brittleness may be a fracture barrier. For example, dolomitic limestone has a high brittleness, but in shale reservoirs, it is a fracture barrier (Bruner and Smosna, 2011).	To improve the precision in forecasting fracture toughness, the researchers could have gathered further experimental data. It is more important to derive crack hardiness from logging data via the correlations of minute errors and to bind the amount of core data.
8	2002	Mijrata, S., Miyoshi, T., Matsuoka, T., Saito, T., and Ashida, Y.	"Visualisation of the Channel Flow through a Single Fracture".	Conducted a study on the visualisation of the channel flow through a single fracture. The rock mass is in the upper fraction of the earth's crust, where the geological seclusion is carried out; this includes the diversity scales of cracks. These cracks have elevated	The simulation may not assess the 3D fluid flow performance, as the Reynolds equation takes for granted the local cubic law; moreover, the standard component of the flow rate vectors to the crack

				permeability over the rock mass intact parts and controlled the fluid flow via the rock mass. Thus, one of the major important study subjects is to typify the fluid flow behaviour through the openings. In general, the crack permeability has been approximated by cubic law. Moreover, the fracture permeability is affected by the stress working on the fracture surface (Witherspoon et al., 1980).	surface may not be taken into consideration. The geometrical surface characteristics and the contact state of fissure surfaces were not overseen in the experiment.
9	2004	Muralidharan, V., Chakravarthy, D., Putra, E. and Schechter, D. S.	"Simulation of Fluid Flow Through Rough Fractures".	Conducted a study on the simulation of fluid flow through rough fractures. Lomize performed the initial inclusive work on flow via open cracks in 1951, when he applied for parallel glass plates and showed the effect of cubic law on laminar flow. He demonstrated fluid flow using various crack shapes and examined the influences of altering the crack walls from even to uneven.	Although numerous studies have been conducted on crack aperture spreads, the consequence of different stress states has not yet been examined. Stress alters aperture size and may have an influence on the spreading of crack apertures. Even though previous researchers have demonstrated that the results of this study show that the apertures follow lognormal distribution even at elevated

				Witherspoon et al. (1980) carried out lab tests to authenticate the theory of the parallel plate and they demonstrated that the parallel plate estimate inclines to failure at elevated natural stress: >10 MPa crosswise the crack. The flow via an individual fissure does not develop consistently, as presumed by the theory of parallel plate; rather, it flows via a restricted number of canals (Tsang, 1983, 1984). Therefore, the fluid flow in these indirect canals tends to track a favoured path. Park et al. (1985) carried out laboratory tests where they introduced melted wood's metal in single cracks at various used stress states. The flow of fluid in these pathways was via the bigger fissures which offered minimum opposition to the flow. The outcomes showed that lesser apertures have a key role in limiting fluid movement.	stress conditions, investigations have not been carried out to explore the crack aperture distribution with alterations in stress states. Despite the likelihood of a flawless visualisation of the crack and matrix, the CT numbers do not signify any physical distinguishment.

10	2013	Okubo, K., Mikada, H., Goto, T.-N. and Takekawa, J.	"Stress Distribution in Fractured Medium and Fracture Propagation due to Formation Pressure Changes".	Conducted a study on stress distribution in fractured medium and fracture propagation due to formation pressure changes. Fracking is a crucial scheme to enhance fluid production in the development of a hydrocarbon basin and in conjunction with different well testing techniques; for instance, drill stem, tests of build-up, etc. In recent years, it has becme well known that fracking also plays a key part in the growth of shale oil. It is as well known that the elongated length and the direction of cracks induced by fracking are powerfully affected by the earth's top layer stress enclosure under which any basin is located. Thus, it is essential to have more knowledge of local stress fields before the use of hydraulic cracks, whilst also obtaining the rock physical parameters of basin formation.	It is hard to predict the crack propagation behaviour from wellbores in a medium local stress owing to the absence of arithmetical systems to mimic rock breakdowns. Conversely, as the pressure of formation is enlarged to 20MPa, the fissure propagates to the y-trend with reasonable curving. Thus, the pre-present fissure may have a noteworthy consequence on the fracking examination by applying the wellbore breakout.

				The crack spread is governed by the local stress field, which might be measured by the acoustic emissions positions during the well testing, examining wellbore induced cracks during drilling, etc. The outcomes of these examinations would be applied to assess the local stress field and the hydraulically induced cracks. Instead, it is acknowledged that hydraulically made cracks cannot be induced as scheduled and might cause a few environmental disputes, for instance, due to contamination, influenced seismicity, etc. To represent failures in the earth's top layer materials in a basic way, a lengthy finite element technique is utilised in this research. For instance, in a complicated stress setting, the stress first spreads around the wellbore as shown under the presence of a crack.	

11	2012	Raeini, A.Q., Blunt, M.J. and Bijeljic, B.	"Modelling two-phase flow in porous media at the pore scale using the volume-of-fluid method".	A study on modelling a two-phase flow in porous media at the pore scale using the volume-of-fluid method Knowing the multiphase run at the micro-level is of maximum significance for a broad range of uses, such as stimulated oil recovery, CO2 storage in subsurface aquifers, and the membrane of proton give-and-take (PEM) fuel cells. However, demonstrating a multiphase flow in permeable paths is a perplexing task because it worries forces working at various levels in the flow area. Viscous forces of the fluid system at larger levels influenced the dissipation of energy in the separate fluids majority. Interfacial tension controls the form and travel of the phase confines. Finally, wall bond forces are energetic at the nano-level width of the lines of contact and govern the angle of contact and contact line dynamics. In several transport difficulties in	Significantly, modelling flow of multiphase in permeable media is a difficult task as it deals with forces acting at various levels in the flow area. Viscid forces are accountable for the wastefulness of the energy of the fluid scheme at larger magnitudes, in most specific fluids. The tension between two faces governs the form and drive of the phase limits. Lastly, the forces of wall adhesion are dynamic at the nano-level thickness of the interaction outlines and govern the angle of contact and the dynamics of the contact line.

				permeable media, forces of the capillary are extra important.	
12	2009	Rahman, M.M., Aghighi, M.A., Rahman, S.S. and Ravoof, S.A.	"Interaction Between Induced Hydraulic Fracture and Pre-existing Natural Fracture in a Poro-Elastic Environment: Effect of Pore Pressure Change and the Orientation of Natural Fractures".	Conducted a study on the interaction between induced hydraulic fracture and pre-existing natural fractures in a poro-elastic environment. It examined the effect of pore pressure change and the orientation of natural fractures. Rocks of a reservoir comprise lots of fractures, seams, bedding and defects. In models of conventional fracking, the generally held supposition is that the crack is a perfect, simple, conventional, bi-wing and spreads equally in a flat vertical to the least stress. Furthermore, in obviously-cracked formations, it may vary significantly from fracking in straight reservoirs. However, owing to interactions with natural cracks, the fissure can spread unequally or in several strands or sections in naturally fissured	Mineback tests have many major variances from fracking, such as low depth and small confining stresses. Moreover, it is not possible to observe hydraulic cracks in the subsurface with much precision, as the restricted entree to the layer is below the surface.

				reservoirs. The existence of natural cracks changes the way the persuaded crack propagates via the rock. Daneshy showed that the fracture tracks the local pathway of minimum opposition, not the common path, which leads to significant branching. Blanton has demonstrated that the spreading crack crosses the ordinary fracture, goes into the natural crack, or in some situations, goes into the natural fissure for a small space, then begin again to spread in an automatically additional favourable orientation, relying mainly on the oncoming angle. Practical studies propose that hydraulic cracks incline to cross the present fractures at a differential stress that is elevated and at elevated approach angles. At low approach angles and a small difference of stress, the natural fissure opens, averting the fracturing liquid and stopping the made crack from crossing, at least momentarily. While spreading, a	

				hydraulic fracture goes in the locality of a self-initiated crack as the changed stress around the natural crack begins from the natural fracture tip. Warpinski and Teufel (1987) performed mine back tests to investigate the influence of geologic cut-outs on hydraulic fracture spread. However, mineback tests have several major dissimilarities from fracking; for instance, low depth and small restricting stresses. Instead, it is not possible to display hydraulic cracks in the subsurface with unlimited exactness, due to the restricted entree to the layers of the subsurface.	
13	2012	Wade, A.C. and Bilgesu, H.I.	"The impact of Hydraulic Fracture and Subsequent Increased Production Due to	Conducted a study on the impact of hydraulic fracture and subsequent increased production due to in-situ stress changes in the Marcellus Shale. Several various shale types are available that can yield natural gas, involving the	However, the results of such completion methods and the succeeding production of gas changes the properties of in-situ rocks and stress enclosures or fields. The consequences of those alterations may have dramatic influences on production

			in-situ Stress Changes in the Marcellus Shale".	Haynesville, Barnett and Fayetteville. The shale reservoirs were not searched for profitable production due to their relatively small permeability. Nevertheless, with the application of fracking linked with horizontal oil well accomplishments or completions, shale layers have developed to become economically yieldable. The extra recent shale finding is the Marcellus Shale location. The Marcellus Shale is situated in the Appalachian Basin, layering many various states. The start of fracking linked with horizontal well completions has opened an entirely new region of natural gas yield. The linkage overcomes the very small permeability amounts in the Marcellus Shale plays and permits a profitable economic production and an increase of the basin. However, the results of the aforementioned completion methods follow the production of gas	and may even result in borehole breakdown.

				changes in the in-situ rock parameters and stress enclosure or field. The results of these changes may have dramatic influences on production and may lead to a borehole breakdown. Several various parameters may be analysed applying geomechanics, however, deformation is one of the most essential, and it is the alteration in size and form of a rock when exposed to force. When the elastic boundary has been touched, lasting and non-recoverable distortion happens which is termed plastic distortion, and it relies much on rock temperature and pressure.	
14	1995	Wright, C.A. and Conant, R.A.	"Hydraulic Fracture Reorientation in Primary and Secondary Recovery from	Conducted a study on hydraulic fracture reorientation in primary and secondary recovery from low-permeability reservoirs. The value of knowing that the principal role of in-situ stress in the hydraulic cracks spread	For mature growth projects below secondary recapture or recovery, crack redirection may be very tricky. Nevertheless, for developed growth projects in secondary recapture, crack redirection may be extremely

			Low-Permeability Reservoirs".	has long been recognised in the petrol industry. The in-situ stress condition governs several aspects of a fracture spread, involving: the geometry of the hydraulic fracture and sizes; the near-borehole crack tortuousness; and the hydraulic frack direction. Understanding the main role that the stress condition plays, not only in fracking, but also in wellbore stability, including the control of formation sand, and borehole casing breakage. The industry has long faced this challenge, often ineffectively, with the problems of determining the condition of in-situ reservoir stress. The effort of measuring in-situ stress states is a supplementary difficulty, whilst activities of production themselves may meaningfully bother the original stress condition.	challenging. The study of the spread of the above actions has demonstrated no indication for a big fracture curve. Regrettably, there is not information from an extensive enough variability of environs and locations to understand whether shared a pre-crack redirection is worldwide or universal.

15	2011	Youn, D. and Gutierrez, M.	"Effect of Fracture Distribution on Permeability of Fractured Rock Masses".	Conducted a study on the effect of fracture distribution on the permeability of fractured rock masses. Finding out whether fissured rock mass permeability is the most essential issue in various fields, for example, as groundwater movement demonstrating pollutant flow and carriage, and hydrocarbon creation. In most cases, the crack permeability path is much bigger than the intact rock masses' permeability. Thus, knowing the scheme of the fissure is the most essential requirement in finding out the cracked rock masses' permeability. Nevertheless, it is difficult to consider every single crack in arithmetical analysis, as the crack sets are not only complicated, but also site and level specific. To consider every crack in a cracked rock mass would be mathematically prohibitive.	It is difficult to study every single crack in the arithmetical analysis as the crack sets are not just complex, but also site and level specific. To consider every crack in a cracked rock bulk would be computationally excessive. Owing to these problems, efforts have been taken to improve effective techniques to examine and calculate cracked rock permeability. Conversely, finding out an exact crack scheme is not likely to come from a high-level reliance in the system. Instead, there is only restricted information from core specimens, outcrop similarities and seismic reviews.

				Explicit and discrete crack and matrix replicas have been applied by several scholars and researchers, such as Snow (1969), Stutthof (2000) and Min et al. (2004). The dual continuum technique, involving dual porosity and double permeability, have been established and utilised by Bare Blatt et al. (1960). Oda (1985) established a crack and permeability tensor technique which accounts for the volume fraction of crack set within of the entire cracked rock domain. The tensor of the permeability of a cracked rock specimen may be determined using the fracture tensor together with the geometrical parameters of a fissure set, for instance, as length, fissure, and direction.	
16	2004	Olson, J.E., Laubach, S.E. and Lander, R. H.	"Improving Fracture Permeability Prediction by Combining	Conducted a study on improving fracture permeability prediction by combining geomechanics and diagenesis.	Conversely, not all cracks are plugged by quartz mortar or cement. In a broad variety of sandstones, there is a doorstep kinematic fissure aperture beyond which

			Geomechanics And Diagenesis".	Elevated temperatures and reactive liquids in sandy reservoirs state that interactions and responses between mechanical and geochemical procedures might considerably enhance the developing rock and crack characteristics. A crack-porosity continuity is essential to understand how fissures perform with fluids. A method to forecast spatial planning by unlocking mode aperture systems is conducted via geomechanical modelling, (Olson, 1993; Olson et al., 2001).	crack porosity is conserved and under which cracks are filled.

Appendix B: Calculation of Nanopermeability, Using Nano-Perm Equipment

The permeability of the final set of Mancos and Marcellus fractured shale samples (the third set of shale samples) is measured for comparison.

The fractures of the second set of samples (Marcellus) were carried out for the horizontal, vertical, two 90^0 vertical, and line and triangle complex fractures. The test was carried out at 34.5, 69, 103.5 and 138 bar using the Nano-Perm machine. Porosity, crack width and crack length were determined using the CT scan (see Appendix C, page 155).

First: Unfractured shale sample: 6.35 mm (L) * 37.44 mm (D)

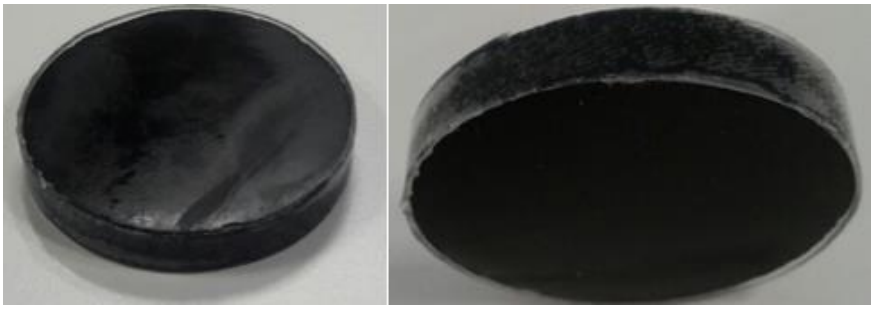

Figure B1: Unfracked Shale Sample (6.35 mm (L) * 37.44 mm (D)

Figure B1 presents the image of the Marcellus unfractured shale sample with dimensions of 6.35 mm (L) x 37.44 mm (D). This sample was measured for permeability and porosity using the Nano-Perm and CT scan (see Table 4-10).

Table B1: Nano-Perm Parameters.

Parameters	Values	Units
Pa	1	atm
ΔP	35/14.696 = 2.382	atm
μ	0.0177	cp
Pm	35/2 =17.5 psi = 17.5/14.696 = 1.191	atm
A	3.14(18.72)2 = 1100 mm2 = 1100*0.01 = 11	Cm2

The parameters Pa, **μ**, Pm and A, shown in Table B1, represent the atmospheric pressure, the viscosity of nitrogen, the mean pressure and the area of the sample. The first three parameters are fixed but the fourth is changeable, which is the area of the sample.

Using the parameters shown in Table B1 and the calculated parameters for ΔP and Q for each pressure value, these are applied to Equation B1 to define permeability as follows:

$$\mathbf{K_{air}} = \frac{\mathbf{Q} * \boldsymbol{\mu} * \mathbf{L} * \mathbf{Pa}}{\boldsymbol{\Delta}\mathbf{P} * \mathbf{Pm} * \mathbf{A}} \ (\mathbf{mD}) \qquad \text{B1}$$

Where,

$\boldsymbol{K_{air}}$ = permeability of air.

Note: Equation (4.1) will be used to calculate all Nano-Permeability.

When overburden pressure = 34.5 bar

Q = rate/time = 0.14/1800 = 7.778 $*\mathbf{10^{-5}}$

$$\mathrm{K_{air}} = \frac{\mathrm{Q} * \mu * \mathrm{L} * \mathrm{Pa}}{\Delta\mathrm{P} * \mathrm{Pm} * \mathrm{A}} \ (\mathrm{mD})$$

$$\mathrm{K_{air}} = \frac{7.778 * 10^{-5} * 0.0177 * 6.35 * 0.1 \ * 1}{2.382 \ * 1.191 * 11} \ (\mathrm{mD})$$

$$\mathrm{K_{air}} = \frac{8.7418 * 10^{-7}}{31.2065} \ (\mathrm{mD})$$

$$\mathrm{K_{air}} = \ 2.80126 * 10^{-8} (\mathrm{mD})$$

When overburden pressure = 69 bar

Q = rate/time = 0.135/1800 = $7.5 * 10^{-5}$ cc/sec

$$\mathrm{K_{air}} = \frac{\mathrm{Q} * \mu * \mathrm{L} * \mathrm{Pa}}{\Delta\mathrm{P} * \mathrm{Pm} * \mathrm{A}} \ (\mathrm{mD})$$

$$K_{air} = \frac{7.5 * 10^{-5} * 0.0177 * 6.35 * 0.1 * 1}{2.382 * 1.191 * 11} (mD)$$

$$K_{air} = \frac{8.4296 * 10^{-7}}{31.20658} (mD)$$

$$K_{air} = 2.701225 * 10^{-8} (mD)$$

The permeability of the unfractured shale sample at the 69 bar is very low because the shale sample is very compacted.

When overburden pressure = 103.5 bar

Q = rate/time = 0.134/1800 = 7.444 $*10^{-5}$ cc/sec

$$K_{air} = \frac{Q * \mu * L * Pa}{\Delta P * Pm * A} (mD)$$

$$K_{air} = \frac{7.444 * 10^{-5} * 0.0177 * 6.35 * 0.1 * 1}{2.382 * 1.191 * 11} (mD)$$

$$K_{air} = \frac{8.3667 * 10^{-7}}{31.20658} (mD)$$

$$K_{air} = 2.6811 * 10^{-8} (mD)$$

When overburden pressure = 138 bar

Q = rate/time = 0.130/1800 = $7.222 * 10^{-5}$ cc/sec

$$K_{air} = \frac{Q * \mu * L * Pa}{\Delta P * Pm * A} \text{ (mD)}$$

$$K_{air} = \frac{7.222 * 10^{-5} * 0.0177 * 6.35 * 0.1 * 1}{2.382 * 1.191 * 11} \text{ (mD)}$$

$$K_{air} = \frac{8.1172 * 10^{-7}}{31.20658} \text{ (mD)}$$

$$K_{air} = 2.20112 * 10^{-8} \text{ (mD)}$$

Second: Fractured shale sample (vertical): 27.72 mm (L) * 37.44 mm (D)

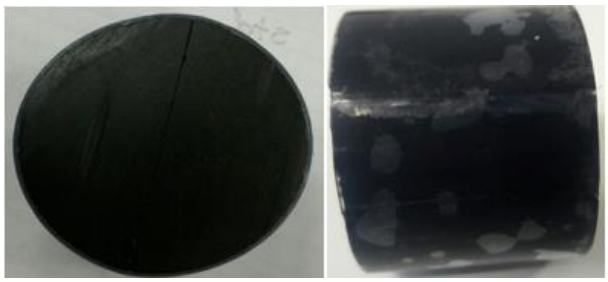

Figure B2: Fractured Shale (Vertical) 27.72 mm, (L) * 37.44 mm, (D)

Figure B2 presents the image of the Marcellus Shale sample fractured vertically at 90^0 with a dimension of 27.72 mm (L) x 37.44 mm (D). This sample was measured for permeability and porosity using the Nano-Perm and CT scan (see Table B2).

When overburden pressure = 69 bar

Q = rate/time = 0.190/1800 = 1.100 *10^{-4} cc/sec

$$K_{air} = \frac{Q * \mu * L * Pa}{\Delta P * Pm * A} \text{ (mD)}$$

$$K_{air} = \frac{1.100 * 10^{-4} * 0.0177 * 27.72 * 0.1 * 1}{2.382 * 1.191 * 11} \text{ (mD)}$$

$$K_{air} = \frac{5.3971 * 10^{-6}}{31.20658} \text{ (mD)}$$

$$K_{air} = 1.7295 * 10^{-7} \text{ (mD)}$$

When overburden pressure = 138 bar

Q = rate/time = 0.190/1800 = $1.060 * 10^{-4}$ cc/sec

$$K_{air} = \frac{Q * \mu * L * Pa}{\Delta P * Pm * A} \text{ (mD)}$$

$$K_{air} = \frac{1.060 * 10^{-4} * 0.0177 * 27.72 * 0.1 * 1}{2.382 * 1.191 * 11} \text{ (mD)}$$

$$K_{air} = \frac{5.2008 * 10^{-6}}{31.20658} \text{ (mD)}$$

$$K_{air} = 1.6666 * 10^{-7} \text{(mD)}$$

Third: Fractured shale sample (double vertical): 27.72 mm (L) * 37.44 mm (D)

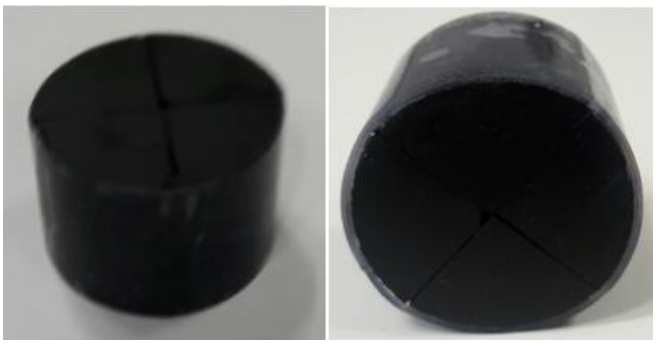

Figure B3: Double Fracked Shale (Vertical) (27.72 mm (L) * 37.44 mm (D)

Figure B3 presents the image of the Marcellus Shale sample with two vertical 90^0 fractures at a dimension of 27.72 mm (L) x 37.44 mm (D). This sample was measured for permeability and porosity using the Nano-Perm and CT scan (see Table B2).

When overburden pressure = 34.5 bar

Q = rate/time = 0.140/1800 = $7.778 * 10^{-5}$ cc/sec

$$K_{air} = \frac{Q * \mu * L * Pa}{\Delta P * Pm * A} \text{ (mD)}$$

$$K_{air} = \frac{7.778 * 10^{-5} * 0.0177 * 27.72 * 0.1 * 1}{2.382 * 1.191 * 11} \text{ (mD)}$$

$$K_{air} = \frac{3.8162 * 10^{-6}}{31.20658} \text{ (mD)}$$

$$K_{air} = 1.2229 * 10^{-7} \text{(mD)}$$

When overburden pressure = 69 bar

Q = rate/time = 0.135/1800 = $7.5 * 10^{-5}$ cc/sec

$$K_{air} = \frac{Q * \mu * L * Pa}{\Delta P * Pm * A} \text{ (mD)}$$

$$K_{air} = \frac{7.5 * 10^{-5} * 0.0177 * 27.72 * 0.1 * 1}{2.382 * 1.191 * 11} \text{ (mD)}$$

$$K_{air} = \frac{3.6798 * 10^{-6}}{31.20658} \text{ (mD)}$$

$$K_{air} = 1.1792 * 10^{-7} \text{ (mD)}$$

When overburden pressure = 103.5

Q = rate/time = 0.130/1800 = $7.222 * 10^{-5}$ cc/sec

$$K_{air} = \frac{Q * \mu * L * Pa}{\Delta P * Pm * A} \text{ (mD)}$$

$$K_{air} = \frac{7.222 * 10^{-5} * 0.0177 * 27.72 * 0.1 * 1}{2.382 * 1.191 * 11} \text{ (mD)}$$

$$K_{air} = \frac{3.5435 * 10^{-6}}{31.20658} \text{ (mD)}$$

$$K_{air} = 1.1355 * 10^{-7} \text{(mD)}$$

When overburden pressure = 138 bar

Q = rate/time = 0.120/1800 = $6.667 * 10^{-5}$ cc/sec

$$K_{air} = \frac{Q * \mu * L * Pa}{\Delta P * Pm * A} \text{ (mD)}$$

$$K_{air} = \frac{6.667 * 10^{-5} * 0.0177 * 27.72 * 0.1 * 1}{2.382 * 1.191 * 11} \text{ (mD)}$$

$$K_{air} = \frac{3.271 * 10^{-6}}{31.20658} \text{ (mD)}$$

$$K_{air} = 1.0482 * 10^{-7} \text{ (mD)}$$

Fourth: Fractured Shale Sample (Horizontal): 27.72 mm (L) * 37.44 mm (D)

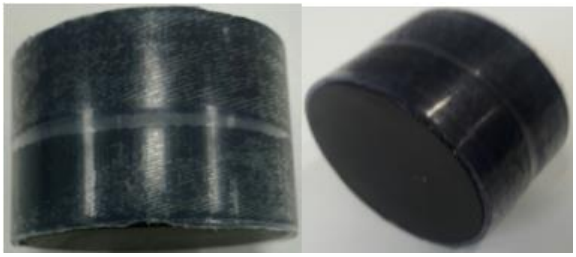

Figure B4: Fracked Shale (Horizontal) (27.72 mm (l) * 37.44 mm (d)

Figure B4 presents the image of the horizontally fractured Marcellus Shale sample with a dimension of 27.72 mm (L) x 37.44 mm (D). This sample was measured for permeability and porosity using the Nano-Perm and CT scan (see Table B2).

When overburden pressure = 34.5 bar

Q = rate/time = 0.100/1800 = $5.556 * 10^{-5}$ cc/sec

$$K_{air} = \frac{Q * \mu * L * Pa}{\Delta P * Pm * A} \text{ (mD)}$$

$$K_{air} = \frac{5.556 * 10^{-5} * 0.0177 * 27.72 * 0.1 * 1}{2.382 * 1.191 * 11} \text{ (mD)}$$

$$K_{air} = \frac{2.7258 * 10^{-6}}{31.20658} \text{ (mD)}$$

$$K_{air} = 8.7347 * 10^{-8} \text{(mD)}$$

When overburden pressure = 69 bar

Q = rate/time = 0.090/1800 = $5 * 10^{-5}$ cc/sec

$$K_{air} = \frac{Q * \mu * L * Pa}{\Delta P * Pm * A} \text{ (mD)}$$

$$K_{air} = \frac{5 * 10^{-5} * 0.0177 * 27.72 * 0.1 * 1}{2.382 * 1.191 * 11} \text{ (mD)}$$

$$K_{air} = \frac{2.4532 * 10^{-6}}{31.20658} \text{ (mD)}$$

$$K_{air} = 7.8612 * 10^{-8} \text{ (mD)}$$

When overburden pressure = 103.5 bar

Q = rate/time = 0.085/1800 = $4.722 * 10^{-5}$ cc/sec

$$K_{air} = \frac{Q * \mu * L * Pa}{\Delta P * Pm * A} \text{ (mD)}$$

$$K_{air} = \frac{4.722 * 10^{-5} * 0.0177 * 27.72 * 0.1 * 1}{2.382 * 1.191 * 11} \text{ (mD)}$$

$$K_{air} = \frac{2.3169 * 10^{-6}}{131.20658} \text{ (mD)}$$

$$K_{air} = 7.4244 * 10^{-8} \text{(mD)}$$

When overburden pressure = 138 bar

Q = rate/time = 0.080/1800 = $4.444 * 10^{-5}$ cc/sec

$$K_{air} = \frac{Q * \mu * L * Pa}{\Delta P * Pm * A} \text{ (mD)}$$

$$K_{air} = \frac{4.444 * 10^{-5} * 0.0177 * 27.72 * 0.1 * 1}{2.382 * 1.191 * 11} \text{ (mD)}$$

$$K_{air} = \frac{2.1806 * 10^{-6}}{31.20658} \text{ (mD)}$$

$$K_{air} = 6.9876 * 10^{-8} \text{ (mD)}$$

Fifth: Fractured shale sample (Line Complex fracture 1): 13.4 mm (L) * 37.44 mm (D)

Figure B5: Line Complex Fractured Shale Sample (13.4 mm, L * 37.44 mm, D)

Figure B5 presents the image of the line complex fractured Marcellus Shale sample with a dimension of 13.4 mm (L) x 37.44 mm (D). This sample was measured for permeability and porosity using the Nano-Perm and CT scan (see Table B2).

When overburden pressure = 34.5 bar

Q = rate/time = 0.190/1800 = 1.000 $*10^{-5}$ cc/sec

$$K_{air} = \frac{Q * \mu * L * Pa}{\Delta P * Pm * A} \text{ (mD)}$$

$$K_{air} = \frac{1.060 * 10^{-4} * 0.0177 * 13.4 * 0.1 * 1}{2.382 * 1.191 * 11} \text{ (mD)}$$

$$K_{air} = \frac{2.514 * 10^{-6}}{31.20658} \text{ (mD)}$$

$$K_{air} = 8.0560 * 10^{-8} \text{(mD)}$$

When overburden pressure = 69 bar

Q = rate/time = 0. 18/1800 = $1 * 10^{-4}$ cc/sec

$$K_{air} = \frac{Q * \mu * L * Pa}{\Delta P * Pm * A} \text{ (mD)}$$

$$K_{air} = \frac{1.00 * 10^{-4} * 0.0177 * 13.4 * 0.1 * 1}{2.382 * 1.191 * 11} \text{ (mD)}$$

$$K_{air} = \frac{2.3718 * 10^{-6}}{31.20658} \text{ (mD)}$$

$$K_{air} = 7.6003 * 10^{-8} \text{(mD)}$$

When overburden pressure = 103.5

Q = rate/time = $0.170/1800 = 9.722 * 10^{-5}$ cc/sec

$$K_{air} = \frac{Q * \mu * L * Pa}{\Delta P * Pm * A} \text{ (mD)}$$

$$K_{air} = \frac{9.444 * 10^{-5} * 0.0177 * 13.4 * 0.1 * 1}{2.382 * 1.191 * 11} \text{ (mD)}$$

$$K_{air} = \frac{2.2399 * 10^{-6}}{31.20658} \text{ (mD)}$$

$$K_{air} = 7.1777 * 10^{-8} \text{ (mD)}$$

When overburden pressure = 138 bar

Q = rate/time = 0.165/1800 = 9.167 $*10^{-5}$ cc/sec

$$K_{air} = \frac{Q * \mu * L * Pa}{\Delta P * Pm * A} \text{ (mD)}$$

$$K_{air} = \frac{9.167 * 10^{-5} * 0.0177 * 13.4 * 0.1 * 1}{2.382 * 1.191 * 11} \text{ (mD)}$$

$$K_{air} = \frac{2.1742 * 10^{-6}}{31.20658} \text{ (mD)}$$

$$K_{air} = 6.9671 * 10^{-8} \text{(mD)}$$

Sixth: Fractured shale sample (Triangle complex fracture 2): 13.4 mm (L) * 37.44 mm (D)

Figure B6: Triangle Complex Fractured Shale Sample (13.4 mm (L) * 37.44 mm (D)

Figure B6 presents the image of the triangle complex fractured Marcellus Shale sample with a dimension of 13.4 mm (L) x 37.44 mm (D). This sample was measured for permeability using the Nano-Perm machine and its porosity was measured using the Liquid Saturation Method and CT scan (see Table B2).

When overburden pressure = 34.5 bar

Q = rate/time = 0.185/1800 = $1.028 * 10^{-5}$ cc/sec

$$K_{air} = \frac{Q * \mu * L * Pa}{\Delta P * Pm * A} \text{ (mD)}$$

$$K_{air} = \frac{1.028 * 10^{-4} * 0.0177 * 13.4 * 0.1 * 1}{2.382 * 1.191 * 11} \text{ (mD)}$$

$$K_{air} = \frac{2.4377 * 10^{-6}}{31.20658} \text{ (mD)}$$

$$K_{air} = 7.8115 * 10^{-8} \text{(mD)}$$

When overburden pressure = 69 bar

Q = rate/time = 0.169/1800 = $9.389 * 10^{-5}$ cc/sec

$$K_{air} = \frac{Q * \mu * L * Pa}{\Delta P * Pm * A} \text{ (mD)}$$

$$K_{air} = \frac{9.389 * 10^{-5} * 0.0177 * 13.4 * 0.1 * 1}{2.382 * 1.191 * 11} \text{ (mD)}$$

$$K_{air} = \frac{2.227 * 10^{-6}}{31.20658} \text{ (mD)}$$

$$K_{air} = 7.1363 * 10^{-8}(mD)$$

When overburden pressure = 103.5 bar

Q = rate/time = 0.165/1800 = $9.167 * 10^{-5}$ cc/sec

$$K_{air} = \frac{Q * \mu * L * Pa}{\Delta P * Pm * A}\ (mD)$$

$$K_{air} = \frac{9.167 * 10^{-5} * 0.0177 * 13.4 * 0.1 * 1}{2.382 * 1.191 * 11}\ (mD)$$

$$K_{air} = \frac{2.1742 * 10^{-6}}{31.20658}\ (mD)$$

$$K_{air} = 6.9671 * 10^{-8}\ (mD)$$

When overburden pressure = 138 bar

Q = rate/time = 0.160/1800 = $8.889 * 10^{-5}$ cc/sec

$$K_{air} = \frac{Q * \mu * L * Pa}{\Delta P * Pm * A}(mD)$$

$$K_{air} = \frac{8.889 * 10^{-5} * 0.0177 * 13.4 * 0.1 * 1}{2.382 * 1.191 * 11}\ (mD)$$

$$K_{air} = \frac{2.1083 * 10^{-6}}{31.20658}\ (mD)$$

$$K_{air} = 6.7559 * 10^{-8}(mD)$$

Table B2: Comparison of Permeability, Porosity and Crack Width & Length.

Shale Core Samples	Sample Size, mm	% Porosity (CT Scan)	Average Width, mm (CT Scan)	Length, mm CT Scan	Permeability, mD: Nano-Perm				Figure No
					34.5 bar	69 bar	103.5 bar	138 bar	
Sample 1: Unfractured (natural)	6.35 (L) * 37.44 (D)	1.37	0.21	34.26	$2.80126 * 10^{-8}$	$2.701225 * 10^{-8}$	$2.6811 * 10^{-8}$	$2.20112 * 10^{-8}$	See Figure B1
Sample 2: Vertical fracture	27.72 (L) *37.44 (D)	4.89	0.22	37.44		$1.7295 * 10^{-7}$		$1.6666 * 10^{-7}$	See Figure B2
Sample 3: Two 90^0 cc/sec vertical Fracture	27.72 (L) * 37.44 (D)	4.17	0.19	37.44	$1.2229 * 10^{-7}$	$1.1792 * 10^{-7}$	$1.1355 * 10^{-7}$	$1.050 * 10^{-7}$	See Figure B3
Sample 4: Horizontal fracture	27.72 (L) * 37.44 (D)	4.50	0.14	37.44	$8.7347 * 10^{-8}$	$7.8612 * 10^{-8}$	$7.4244* 10^{-8}$	$6.9876 * 10^{-8}$	See Figure B4

Sample 5: Line complex fracture	13.4 (L) * 37.44 (D)	1.81%			$8.0560 * 10^{-8}$	$7.6003 * 10^{-8}$	$7.1777 * 10^{-8}$	$6.9671 * 10^{-8}$	See Figure B5
Sample 6: Triangle complex fracture	13.4 (L) * 37.44 (D)	1.82%			$7.8115 * 10^{-8}$	$7.1363 * 10^{-8}$	$6.9671 * 10^{-8}$	$6.7559 * 10^{-8}$	See Figure B6

Appendix C: Crack Width and Crack Length Measurement Using CT scan

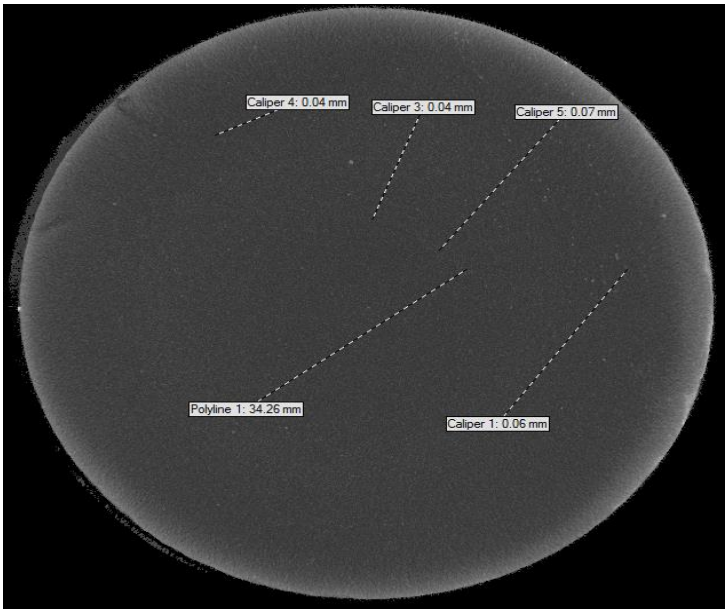

Figure C1: Reconstruction of Unfractured Shale Sample 6.35 mm (L) * 37.44 mm (D)

The image, shown in Figure C1, is the reconstruction of the unfractured Marcellus Shale sample which is processed further to measure the crack width and crack length, as shown in Figure C2.

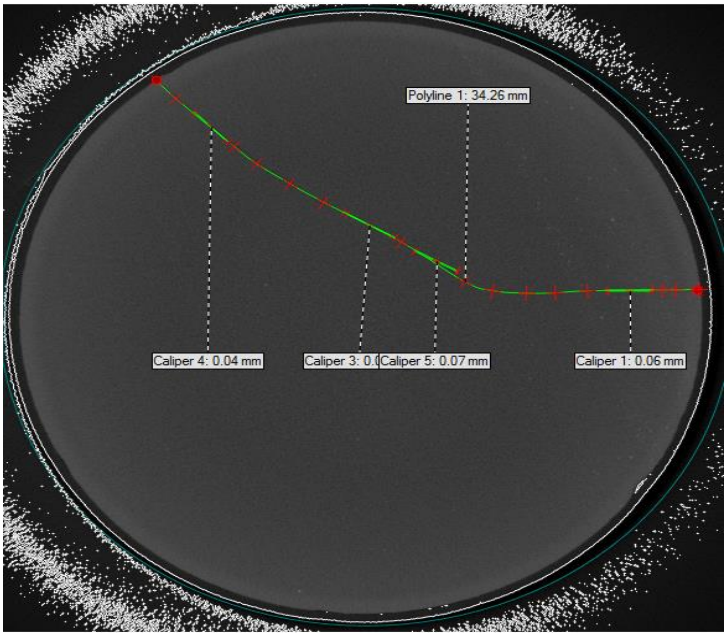

Figure C2: Planar Image of CT Scan of Unfractured Shale Sample

The planar image, seen in Figure C2, shows the method to measure the crack width and crack length. The crack width is measured 4 times and the average is taken, as shown in the calculation below; the length is the polyline of the natural fracture, which is 34.26 mm.

Figures from C1 to C8 show how crack width and crack length are measured.

- This sample is naturally fractured.
- The length of the fracture (Polyline) = 34.26 mm
- The average width of the natural frack = (0.04+0.04+0.07+0.06)/4
  = 0.21 mm
- The porosity and permeability of this naturally fractured shale sample are 1.37% and 4.65E-03 mD.
- Porosity and permeability are the minima for the unfractured shale sample.

Figure C3: Reconstruction of 90^0Vertical Fractured Shale Sample 27.72 mm (L) * 37.44mm (D)

Figure C3 shows the reconstruction of the 90^0 vertical Marcellus Shale sample, which is processed further to measure the crack width and crack length, as demonstrated in Figure C4.

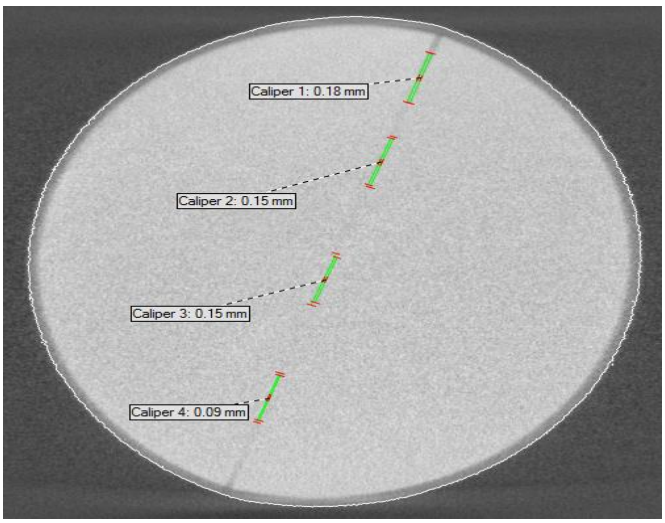

Figure C4: Planar Image of CT Scan of 90^0Vertical Fractured Shale Sample

The planar image, seen in Figure C4, shows the method to measure the crack width and crack length. The width is measured 4 times and then averaged, as shown in the calculation below and the length is the sample diameter, which is 37.44 mm.

- This sample is 90^0 vertically mechanically fractured.
- The average width of the natural frack = (0.18+0.15+0.15+0.09)/4= 0.14 mm
- The porosity and permeability of this vertically mechanically fractured sample are 4.50% and 2.25E-02 mD.
- The porosity and permeability are less than that of the two 90^0 fractured shale sample.

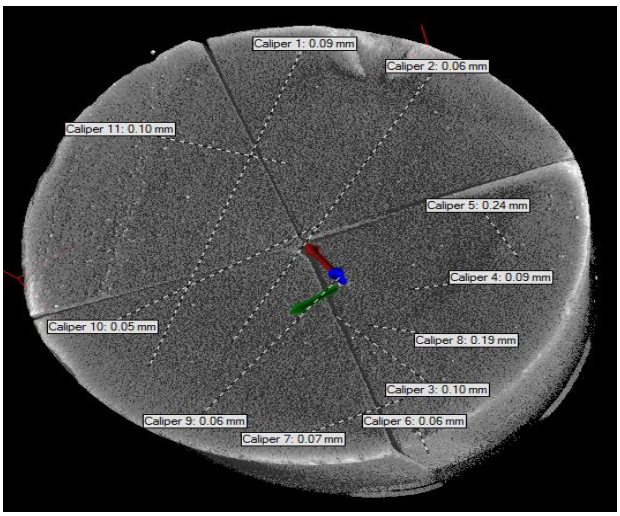

Figure C5: Reconstruction of Two 90^0 Vertical Fractured Shale Sample 27.72 mm (L) * 37.44 mm (D)

Figure C5 shows the reconstruction of the two 90^0 vertical Marcellus Shale sample, which is processed further to measure the crack width and crack length, as shown in Figure C6.

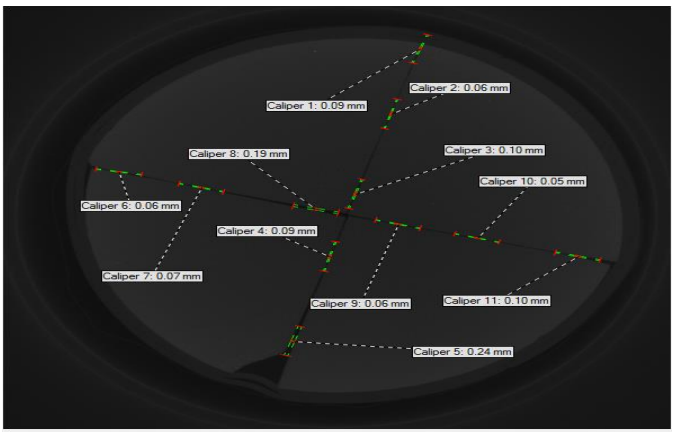

Figure C6: Planar Image of CT Scan of Two 90^0 Vertically Fractured Shale Sample

The planar image, as seen in Figure C6, demonstrates the method of how to measure the crack width and crack length. The width is measured 11 times and then averaged, as shown in the calculation below and the length is the sample diameter, which is 37.44 mm.

- This sample is two 90^0 vertically mechanically fractured.
- The average width of the two 90^0 frack = (0.9+0.6+0.19+0.10+0.05+0.06+0.09+0.07+0.06+0.10+0.24)/11= 0.22 mm
- The porosity and permeability of this two 90^0 mechanically fractured sample are 4.89% and 1.68E-07 mD, as shown in Table 4-9.
- The porosity and permeability are the maxima of the two 90^0 fractured shale sample.

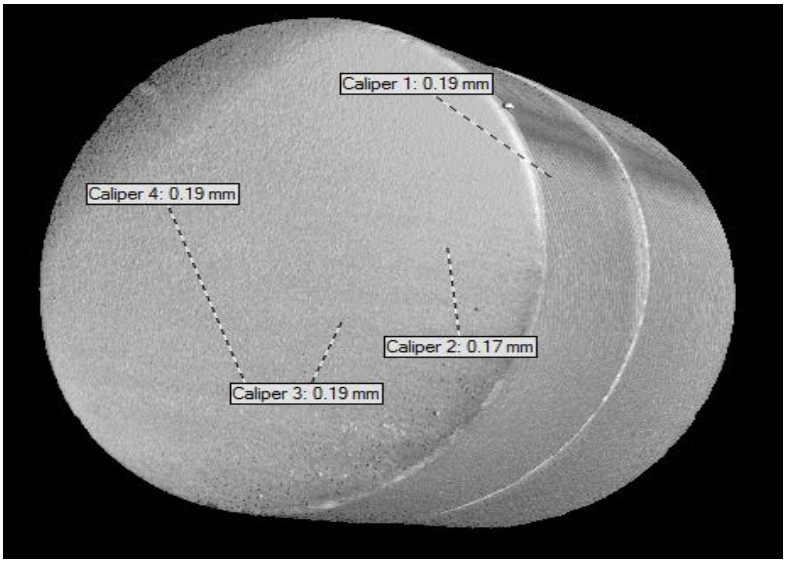

Figure C7: Reconstruction of Horizontal Fractured Shale Sample27.72 mm (L) * 37.44 mm (D)

Figure C7 shows the reconstruction of the horizontal Marcellus Shale sample, which is processed further to measure the crack width and crack length, as shown in Figure C8.

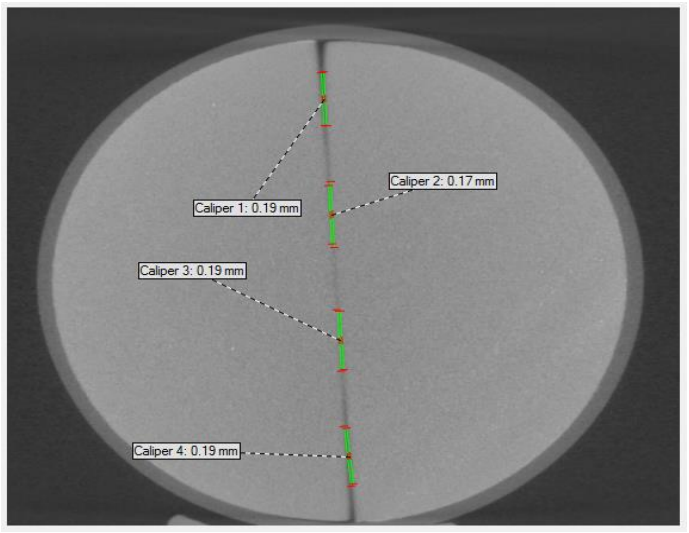

Figure C8: Planar Image of CT Scan of Horizontal Fractured Shale Sample

The planar image, as seen in Figure C8, demonstrates the method to measure the crack width and crack length. The width is measured 4 times and then averaged, as shown in the calculation below and the length of the crack is the sample diameter, which is 37.44 mm.

- This sample is horizontally mechanically fractured.
- The average width of the horizontal frack = (0.19+0.17+0.19+0.19)/4
  = 0.19 mm
- The porosity and permeability of this horizontally mechanically fractured sample are 4.17% and 1.15E-07 mD, as shown in Table 4-9.
- The porosity and permeability are less than that of the vertical at 90^0 fractured shale sample.

CT scan Porosity Values

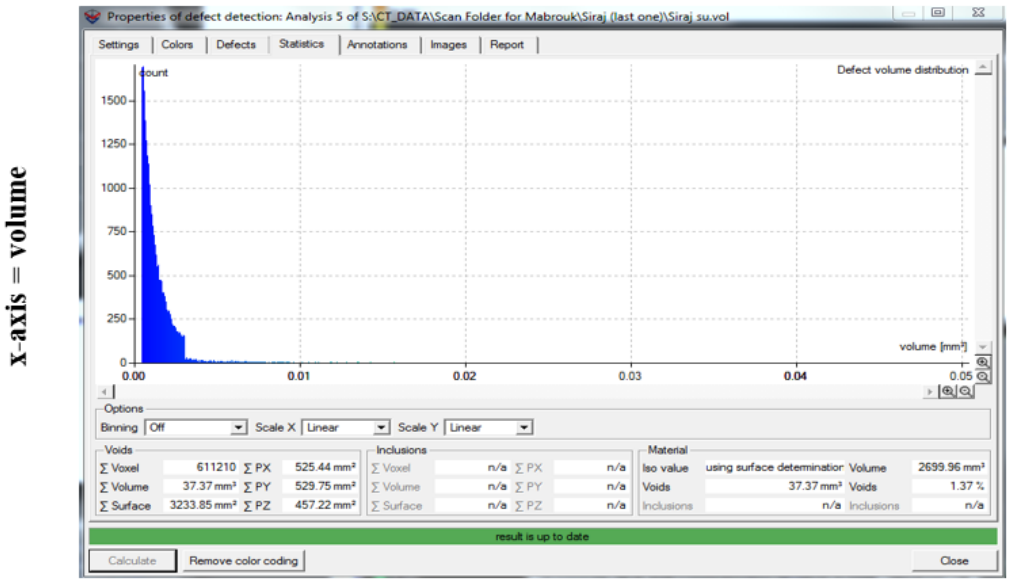

Figure C9: Marcellus Unfractured Shale Sample Porosity Computation using the CT Scanner.

The porosity is found using the CT scan, shown in Figure C9, which is the value of the percentage voids. Here, the Marcellus porosity of the unfractured sample is 1.37%. The porosity accuracy is dependent on the accuracy of the CT scan, which means there will be some negligible minor error (Table 4-7 shows the fractured shale porosity values). For more detail, refer to page 155, Appendix C.

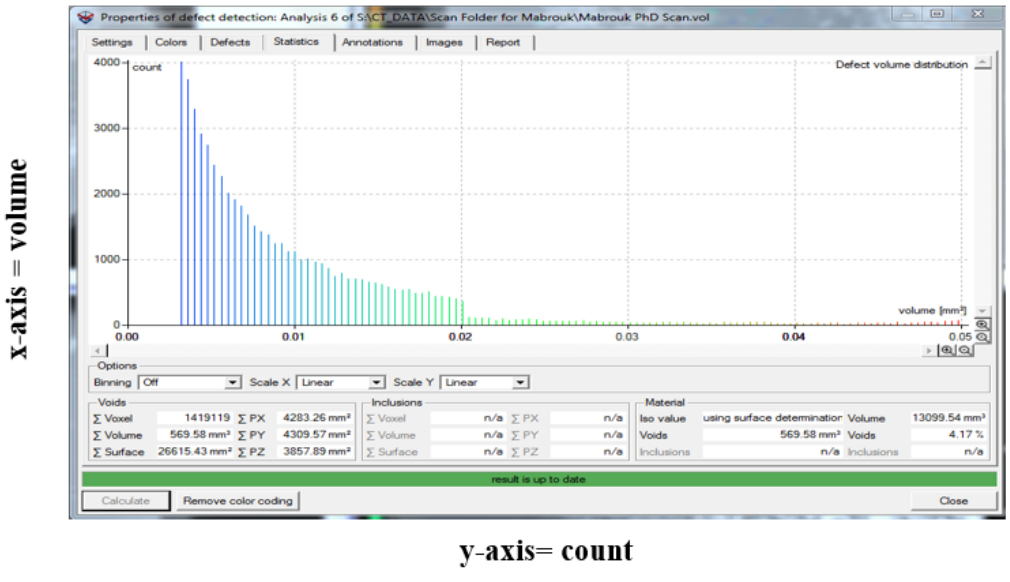

Figure C10: Marcellus Horizontal Fractured Shale Sample Porosity Computation using the CT Scanner.

The porosity is found using the CT scan, as shown in Figure C10, which is the value of the percentage voids. Here, the Marcellus porosity of the horizontal sample is 4.17%. The porosity accuracy is dependent on the accuracy of the CT scan, which means there will be some negligible minor error (see Table 4-3 for the fractured shale porosity values).

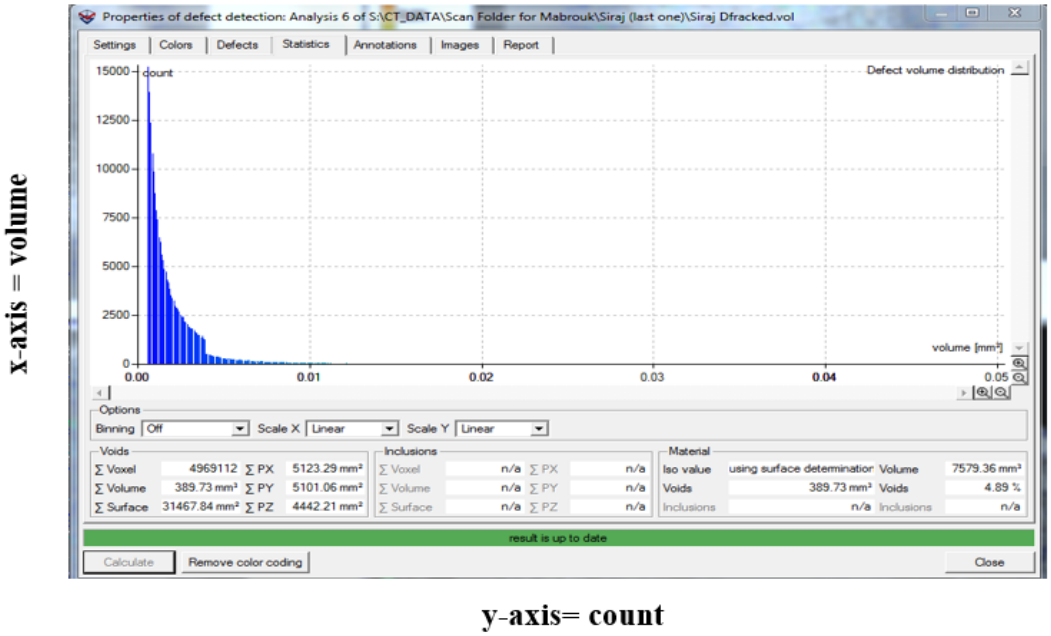

Figure C11: Marcellus Two 90-degree Vertical Fractured Shale Sample Porosity Computation using CT Scanner.

The porosity is found using the CT scan, as shown in Figure C11, which is the value of the percentage voids. Here, the Marcellus porosity for the two 90-degree vertical fractured sample is 4.89%. The porosity accuracy is dependent on the accuracy of the CT scan, which means there will be some negligible minor error (Tables 4-3 and 4-5 show the fractured shale porosity values).

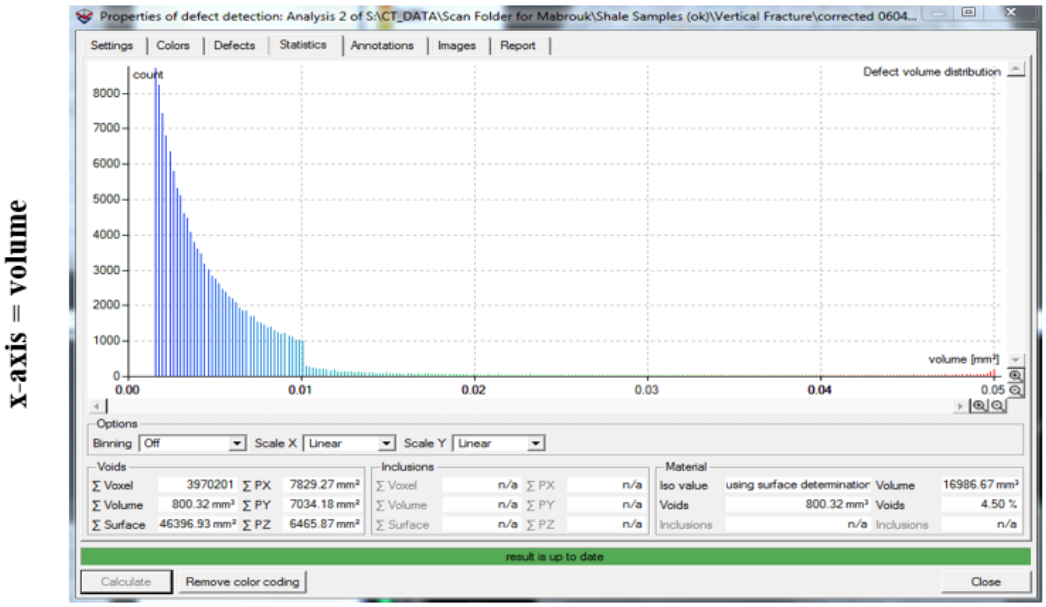

Figure C12: Marcellus 90- Degree Vertical Fractured Shale Sample Porosity Computation Using the CT Scanner.

The porosity is found using the CT scan, as shown in Figure C12, which is the value of the percentage voids. Here, the Marcellus porosity of the 90-degree fractured sample is 4.50%. The porosity accuracy is dependent on the accuracy of the CT scan, which means there will be some negligible minor error when dealing with decimal numbers (see Table 4-4 for the fractured shale porosity values).

Previous Permeability CT Scan Results of the First Set of Unfractured Shale Samples (Eagle Ford, Mancos and Marcellus)

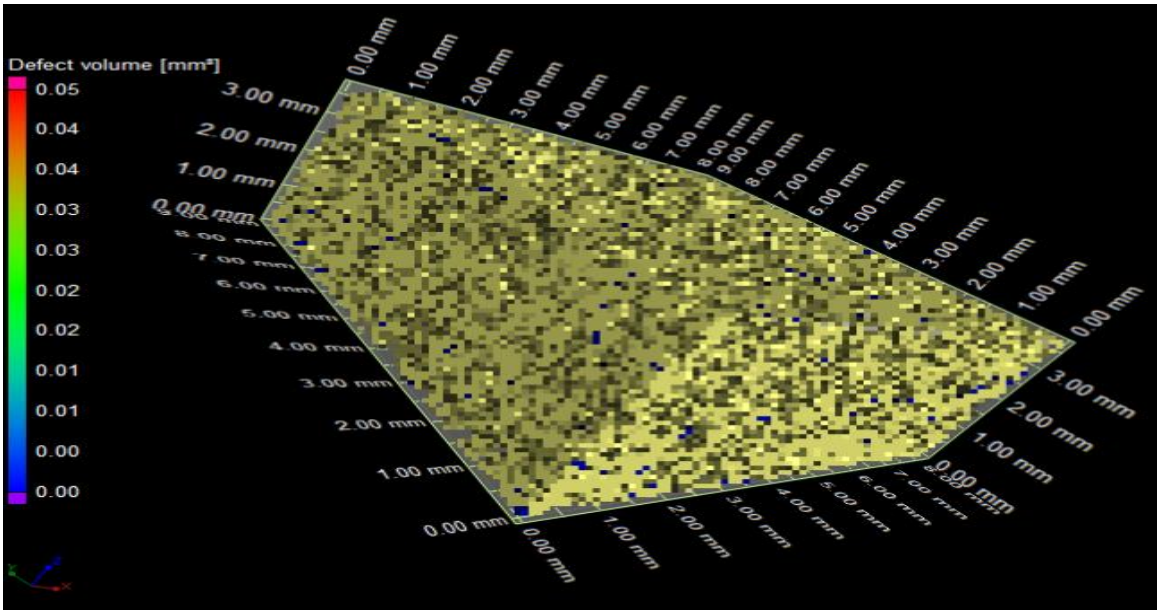

Figure C13: Eagle Ford Shale Sample Reconstruction showing the Compaction of Grains.

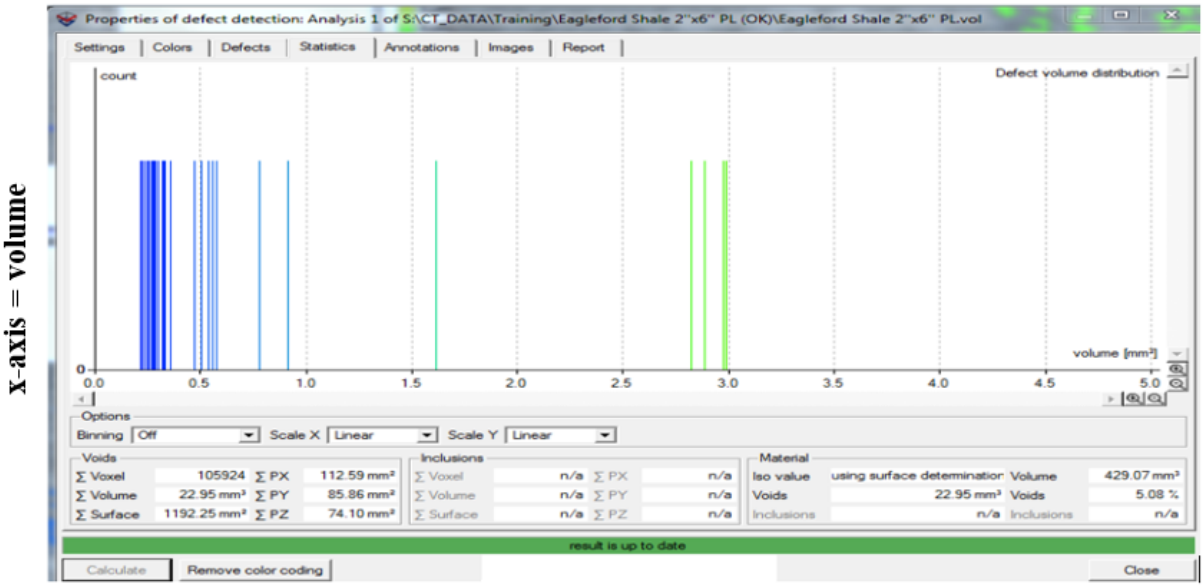

x-axis = volume

y-axis = count

Figure C14: Eagle Ford PL Porosity CT scan

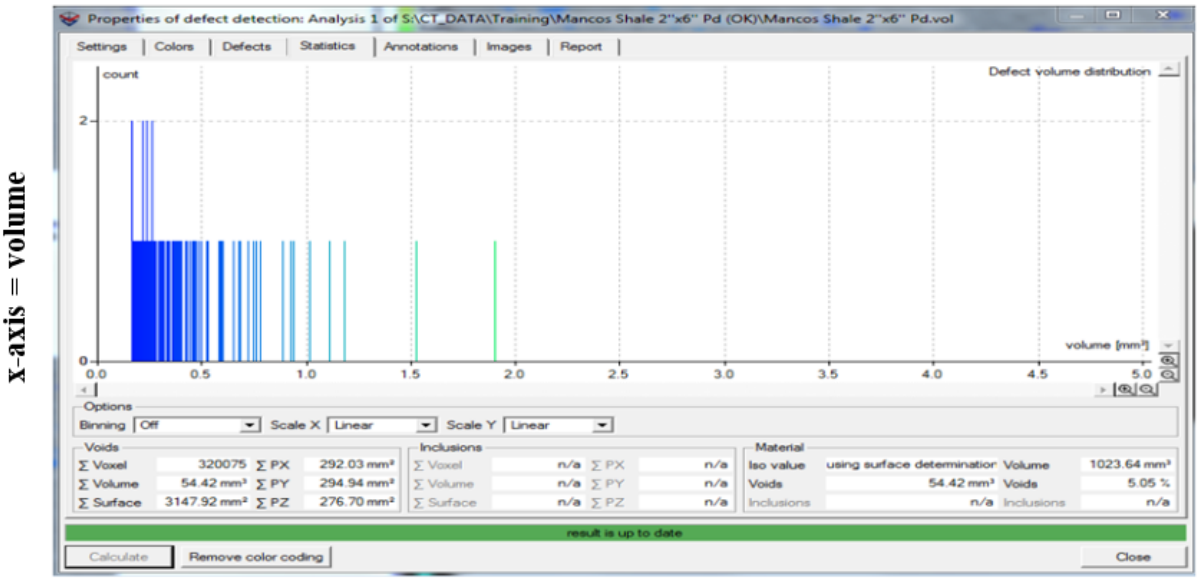

Figure C15: Eagleford PL Porosity using CT Scan

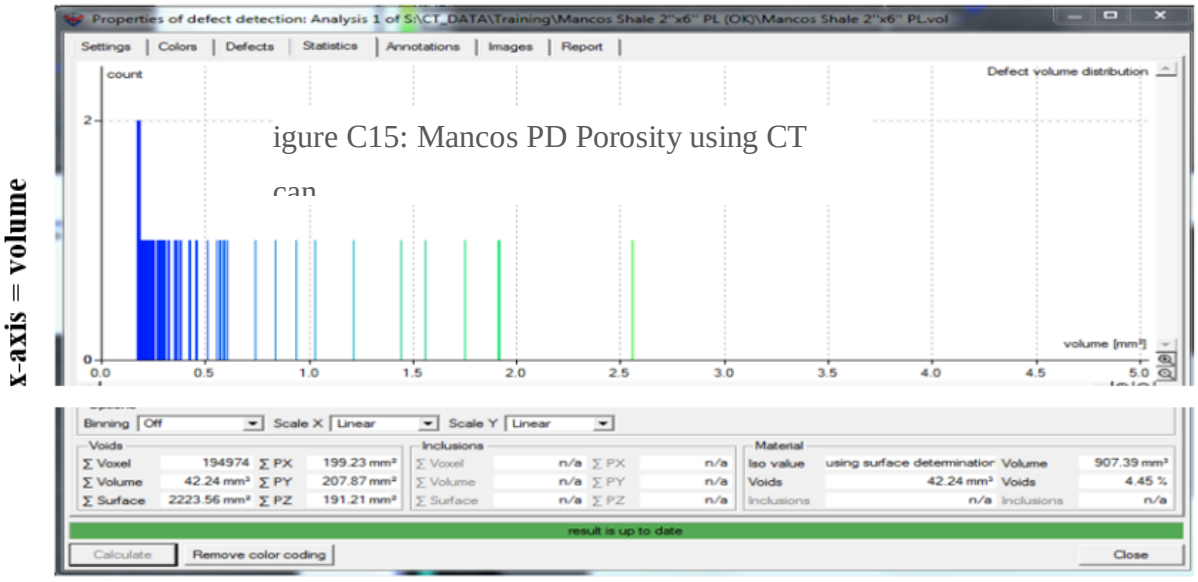

Figure C16: Mancos PL Porosity using CT Scan

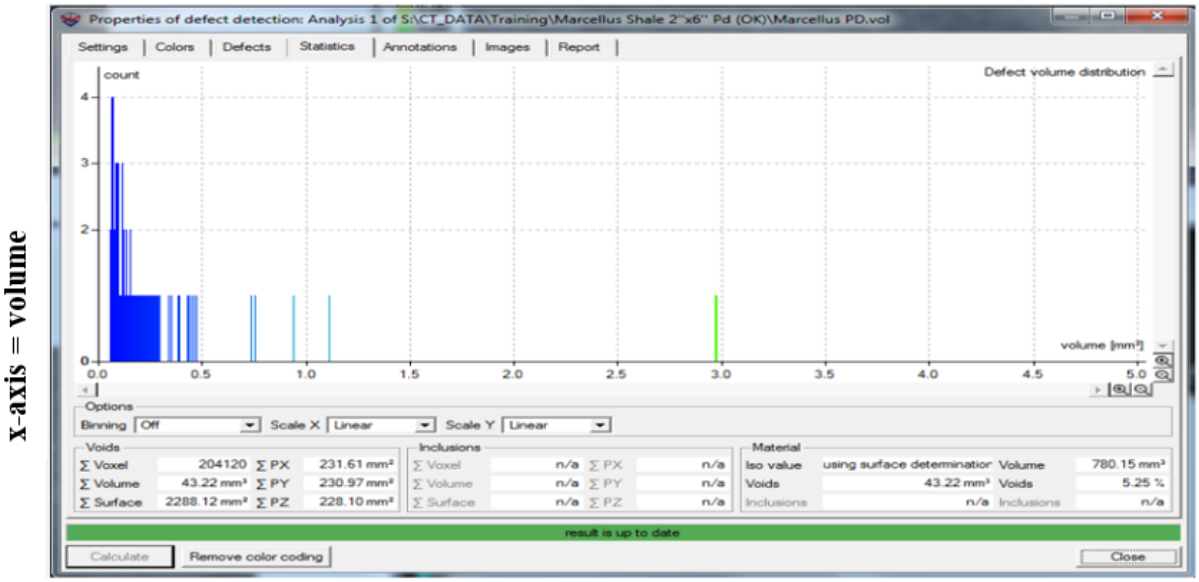

Figure C17: Marcellus PD Porosity using CT Scan

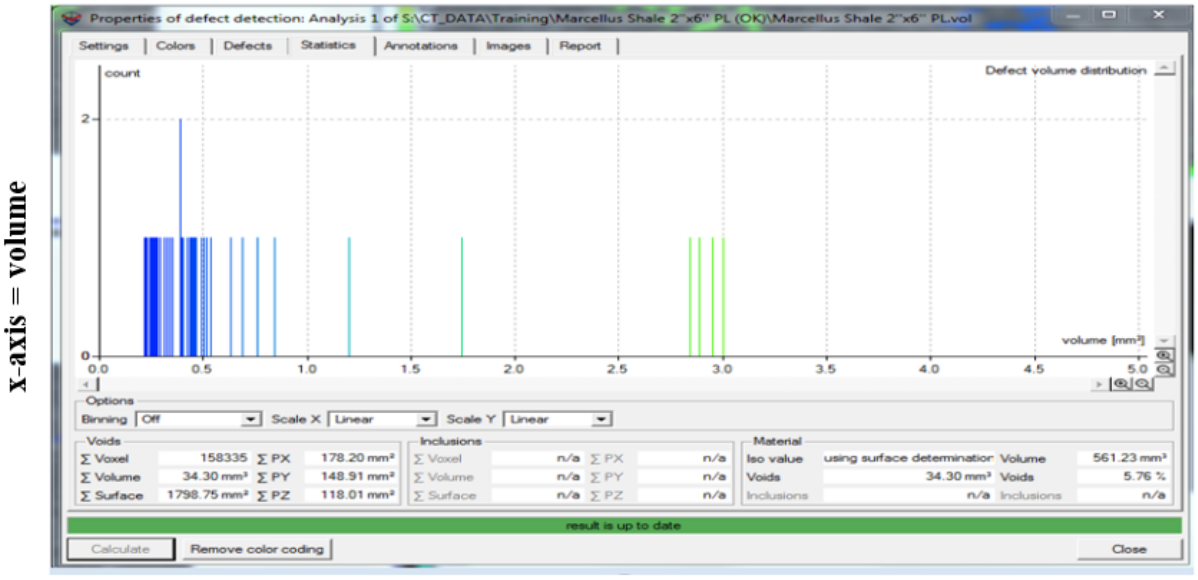

Figure C18: Marcellus PL Porosity using CT Scan

Appendix D: Permeability of the Second Set of Unfractured and Fractured Marcellus Shale Samples (Previous Measurement at Constant Delta and Time)

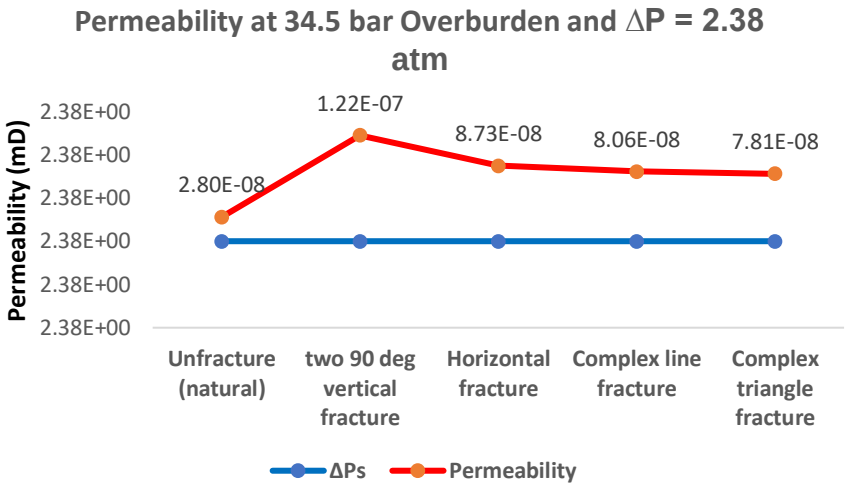

Figure D1: Permeability Values of Unfractured and Fractured Marcellus at 34.5 bar and Different ΔP

As shown in Figure D1, the ΔP is constant at 2.38 atm, but the permeability differs according to shale; for example, the unfractured or fractured at different orientation angles. Specifically, the permeability for the Unfractured Marcellus at 34.5 bar is 2.80E-08, whereas the Triangle Complex Fracture is 1.62E-07 mD. The permeability of complex fractures (line and triangle) is at the maximum due to the presence of more channels through the rock. The overburden pressure is inversely related to the permeability, for example, 2.80E-08 at 34.5 bar and 2.70E-08 at 69 bar, because it creates compaction to the shale sample. In comparison, ΔP is directly related to permeability as it signifies the difference between the inlet and outlet pressures; this is why a greater ΔP will increase the flow rate.

Appendix D: Permeability of the Second Set of Unfractured and Fractured Marcellus Shale Samples (Previous Measurement at Constant Delta and Time)

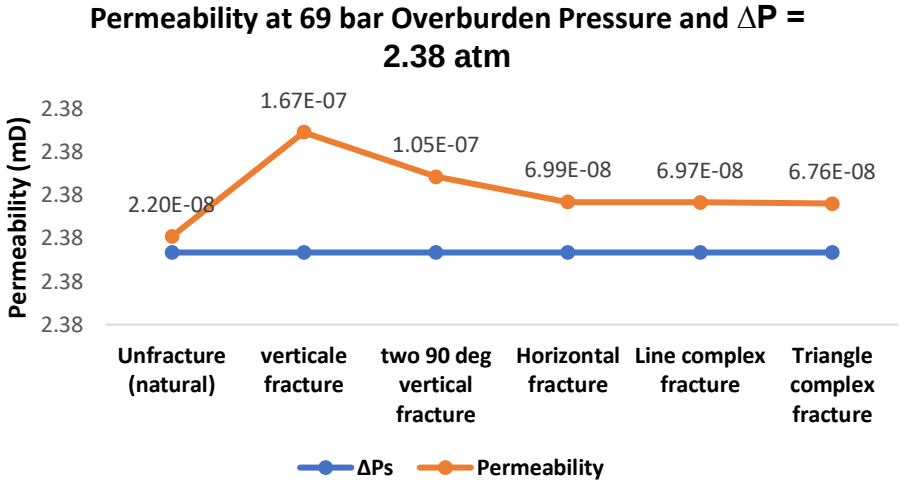

Figure D2: Permeability Values of Unfractured and Fractured Marcellus at 69 bar and Different ΔP

In line with further results (Figure D2), ΔP is fixed at 2.38 atm, but the permeability is dissimilar according to the shale: For example, unfractured or fractured at diverse orientation angles. In particular, the permeability for the Unfractured Marcellus sample at 69 bar shows 2.70E-08 whereas for the Triangle Complex Fracture it is 1.48E-07 mD. The permeability of the complex fractures (Line and Triangle) is higher due to the additional channels penetrating the rock and at 90-degree vertical angles. The overburden pressure is inversely related to the permeability; for example, 2.70E-08 at 34.5 bar and 2.68E-08 at 103.5 bar. This is because it causes compaction to the shale sample whereas the ΔP is directly related to the permeability because it represents the difference between the inlet and outlet pressures and is proof that a greater ΔP will increase the flow rate.

Appendix D: Permeability of the Second Set of Unfractured and Fractured Marcellus Shale Samples (Previous Measurement at Constant Delta and Time)

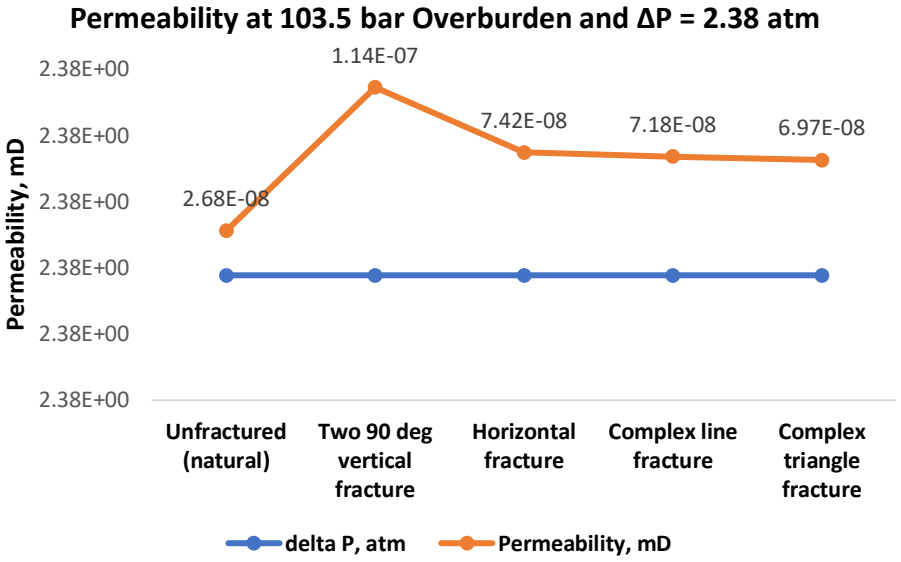

Figure D3: Permeability Values of Unfractured and Fractured Marcellus at 103.5 bar and Different ΔP

It is clear from Figure D3, that ΔP was placed at a fixed value of 2.38 atm, but the permeability values accord with the shale: For example, between the unfractured and fractured at various orientation angles. Thus, the permeability of the Unfractured Marcellus Shale sample, when the overburden is 103.5 bar is 2.68E-08. In comparison, the value of the Triangle Complex Fracture is 1.44E-07 mD. The permeabilities of the complex fractures (line and triangle) are superior because they have more channels crossing the rock. The overburden pressure is contrarily related to permeability; for example, 2.68E-08 at 103.5 bar and 2.60E-08 at 138 bar. This is because of the compaction of the shale sample, while the ΔP is directly related to the permeability as it represents the variance between the inlet and outlet pressures, which explains why a greater ΔP will raise the flow rate.

Appendix D: Permeability of the Second Set of Unfractured and Fractured Marcellus Shale Samples (Previous Measurement at Constant Delta and Time)

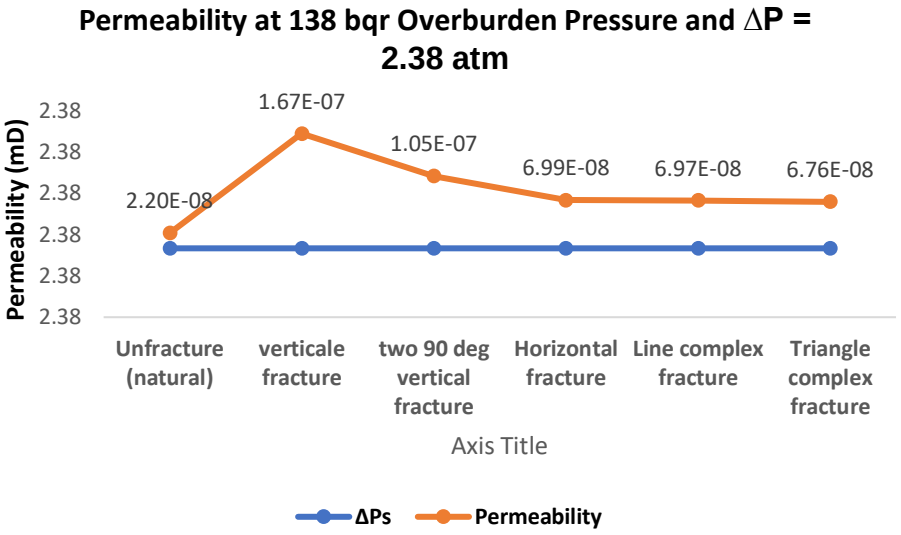

Figure D4: Permeability Values of Unfractured and Fractured Marcellus at 138 bar and Different ΔP

Similar to the previous results (Figure D4), it can be inferred that ΔP has a constant value at 2.38 atm, but the permeability changes according to shale: For example, whether unfractured or fractured at dissimilar orientation angles. The permeability for the unfractured Marcellus at 138 bar is 2.60E-08 whereas the Triangle Complex Fracture has a value of 1.40E-07 mD. The permeability at a 90-degree vertical fracture and at complex fractures (Line and Triangle) are the maximal cause of more channels over the rock. The permeability values are not consistent because an error occurs when the samples are fractured. The overburden pressure is inversely related to the permeability, such as 2.80E-08 at 34.5 bar and 2.60E-08 at 138 bar. This is because it enhances the shale rock compaction, whereas ΔP is directly correlated to the permeability because it exemplifies the dissimilarity between the pressures of the inlet and outlet, which is evidence that a greater ΔP will increase the flow rate.

Appendix E: Comparison of the permeability between Mancos and Marcellus Shales

Table E1: Comparison of the permeability between Mancos and Marcellus Shales

Mancos	Marcellus	Overburden Pressure (bar)	ΔP (bar)	Mancos Permeability (mD)	Marcellus Permeability (mD)
No Fracture	No Fracture	100	2.0	8.83E-07	3.42E-07
			3.0	1.44E-06	3.05E-06
			4.0	5.97E-06	7.92E-06
		150	3.0	7.24E-08	2.18E-09
			4.0	1.13E-07	3.61E-08
Fracture 1	Fracture 1	100	0.5	3.05E-07	1.37E-05
			1.0	1.91E-06	6.74E-05
			2.0	8.66E-06	2.67E-04
			3.0	6.42E-05	NA
			4.0	2.15E-04	NA
		150	0.5	2.29E-07	2.29E-07
			1.0	1.65E-06	1.63E-06
			2.0	1.35E-05	2.49E-05
			3.0	5.20E-05	3.71E-05
			4.0	1.44E-04	6.83E-05
		200	0.5	6.10E-08	6.10E-08
			1.0	5.72E-07	5.72E-07
			2.0	5.51E-06	8.88E-06

			3.0	2.01E-05	2.13E-05
			4.0	5.02E-05	5.18E-05
Fracture 2	Fracture 2	100	0.5	9.42E-06	2.54E-05
			1.0	2.04E-05	3.60E-05
			2.0	4.72E-05	1.20E-04
			3.0	8.41E-05	2.59E-04
			4.0	1.25E-04	4.24E-04
		150	0.5	6.87E-06	6.29E-06
			1.0	1.30E-05	1.56E-05
			2.0	2.89E-05	7.47E-05
			3.0	4.57E-05	1.66E-04
			4.0	7.16E-05	2.07E-04
		200	0.5	4.30E-06	No flow
			1.0	8.59E-06	1.01E-05
			2.0	2.16E-05	5.06E-05
			3.0	3.19E-05	1.10E-04
			4.0	4.59E-05	1.82E-04

Appendix F: Barnett, Eagle Ford, Mancos and Marcellus Shales Chemical Analysis

Table F1: Barnett Shale Sample Chemical Analysis

Elements	Sample Barnett Shale PL TEXT SIDE	1	2	3	4	5	Average Percent
Mo	8.26	7.86	8.43	7.25	8.03	7.47	0.000788333
Zr	12.09	11.41	11.91	11.28	11.39	12.34	0.001173667
Sr	112.93	113.18	112.03	108.95	110.89	108.94	0.011115333
U	< LOD	< LOD	< LOD	< LOD	< LOD	< LOD	0
Rb	13.39	13.65	13.4	12.26	11.97	12.03	0.001278333
Th	< LOD	< LOD	< LOD	< LOD	< LOD	< LOD	0
Pb	40.76	38.44	36.47	8.28	10.22	9.25	0.002390333
Au	< LOD	< LOD	< LOD	< LOD	< LOD	< LOD	0
Se	< LOD	< LOD	< LOD	< LOD	< LOD	< LOD	0
As	8.71	10.63	13.43	3.53	< LOD	4.02	0.0008064
Hg	< LOD	< LOD	< LOD	< LOD	< LOD	< LOD	0

Zn	20.08	15.74	15.12	21.94	19.4	22.87	0.001919167
W	< LOD	< LOD	< LOD	< LOD	< LOD	< LOD	0
Cu	< LOD	< LOD	< LOD	< LOD	< LOD	< LOD	0
Ni	< LOD	< LOD	< LOD	< LOD	< LOD	< LOD	0
Co	< LOD	< LOD	< LOD	< LOD	< LOD	< LOD	0
Fe	11421.84	11436	11391	10588	10685	10645.1	1.102768833
Mn	662.43	684.77	687	681.06	645.7	640.44	0.06669
Cr	47.64	48.54	45.29	36.65	40.34	35.81	0.004237833
V	65.16	62.99	59.37	57.04	52.62	56.82	0.0059
Ti	361.91	356.31	337.42	363.19	324.87	324.23	0.0344655
Sc	< LOD	< LOD	< LOD	< LOD	< LOD	< LOD	0
Ca	404435.03	406956	406910	409629	410255	409104	41.00455
K	5891.5	5858.3	5984.4	5329.2	5231	5305.09	0.559993
S	9237.16	9169.1	9223.4	7466.3	7494.9	7442.39	0.833887833

Ba	446.1	441.93	442.42	462.18	441.19	434.56	0.044473
Cs	22.92	22.75	23.24	23.83	22.77	22.59	0.002301667
Te	230.89	220.08	222.43	228.3	226.77	217.33	0.02243
Sb	122.3	118.21	117.03	120.06	123.04	115.73	0.0119395
Sn	84.8	85.13	81.72	86.13	81.8	78.44	0.008300333
Cd	6.04	6.83	6.49	6.51	5.7	5.44	0.000616833
Ag	< LOD	< LOD	< LOD	< LOD	< LOD	< LOD	0
Pd	15.22	16.5	18.2	15.01	18.44	14.65	0.001633667
Bal	510250.41	516508	516999	532587	529386	532286	53.00269
Nb	3.34	4.27	3.6	2.71	3.22	2.73	0.000331167
Bi	< LOD	< LOD	< LOD	< LOD	< LOD	< LOD	0
Re	< LOD	< LOD	< LOD	< LOD	< LOD	< LOD	0
Ta	< LOD	< LOD	< LOD	< LOD	< LOD	< LOD	0
Hf	< LOD	< LOD	< LOD	< LOD	< LOD	< LOD	0

Al	11391.07	12493	11650	6677	8682.2	7206.11	0.968311167
P	3466.54	3527	3627.6	2600.3	2824.9	2787.26	0.313893
Si	34125	34437	34725	25554	25908	25670.4	3.006988167
Cl	94.73	95.85	89.7	64.25	60.26	57.07	0.007697667
Mg	< LOD	< LOD	< LOD	< LOD	< LOD	< LOD	0
Total Average Percent							100.1047632
Others Total Percent							4.578152733

Table F2: Eagle Ford Shale Sample Chemical Analysis

Elements	Sample Eagle Ford Shale PL TEXT SIDE	1	2	3	4	5	Average Percent
Mo	23.94	23.88	24.35	22.57	23.31	23.4	0.0023575
Zr	35.61	35.05	34.8	36.05	35.05	36.42	0.003549667
Sr	865.97	860.3	865.29	887.44	889.36	883.34	0.087528333
U	5.25	7.93	7.32	6.76	8.24	7.05	0.000709167

Rb	13.4	13.34	12.16	12.22	12.84	12.97	0.001282167
Th	2.67	2.38	2.64	2.49	2.51	2.67	0.000256
Pb	8.4	9.44	8	24.08	21.84	22.57	0.001572167
Au	12.71	12.39	11.2	10.15	11.18	11.26	0.001148167
Se	6.17	7.59	7.74	7.19	7.77	8.05	0.000741833
As	11.05	9.59	10.46	13.73	12.91	14.4	0.001202333
Hg	< LOD	< LOD	5.77	< LOD	< LOD	< LOD	0.000577
Zn	102.02	96.97	100.63	102.11	99.23	103.95	0.010081833
W	27.67	28.86	24.95	37.1	34.53	28.11	0.003020333
Cu	37.05	35.79	31.84	34.23	37.2	34.56	0.003511167
Ni	225.73	220.02	216.7	221.4	217.48	218.75	0.022001333
Co	55.86	46.29	72.28	37.68	47.37	54.23	0.0052285
Fe	5983.2	6000.2	5946.1	6262.6	6234.7	6238.1	0.611079333
Mn	244.61	220.58	236.2	233.01	236.07	222.77	0.023220667

Cr	< LOD	< LOD	< LOD	< LOD	< LOD	< LOD	0
V	192.88	190.52	187.65	189.26	189.23	190.84	0.019006333
Ti	465.68	459.31	448.46	438.21	436.17	463.3	0.0451855
Sc	489.3	399.25	419.8	402.67	343.77	295.2	0.0391665
Ca	268883	269623	270201	276117	278512	278321	28.00094883
K	3651.3	3776.5	3716.4	3473.2	3338.5	3410	0.356097833
S	15360	15449	15474	9780.3	9829.9	9822.4	1.261931
Ba	383.98	386.76	386.41	388.09	401.99	405.12	0.039205833
Cs	19.96	19.21	19.68	19.81	20.59	21.15	0.002006667
Te	191.2	187.48	187.15	186.88	194	196.72	0.019057167
Sb	102.49	102.9	101.92	112.31	110.79	110.51	0.010682
Sn	65.83	70.07	67.56	71.97	74.47	70.81	0.007011833
Cd	6.2	5.56	5.01	5.85	5.46	5	0.000551333
Ag	< LOD	< LOD	< LOD	< LOD	< LOD	< LOD	0

Pd	13.14	11.05	13.52	11.27	12.86	11.77	0.001226833
Bal	520938	517890	515895	528375	533970	533214	52.50469917
Nb	2.74	2.69	2.54	2.6	2.85	2.74	0.000269333
Bi	< LOD	< LOD	< LOD	< LOD	< LOD	< LOD	0
Re	< LOD	< LOD	< LOD	< LOD	< LOD	< LOD	0
Ta	< LOD	< LOD	< LOD	< LOD	< LOD	< LOD	0
Hf	< LOD	< LOD	< LOD	< LOD	< LOD	< LOD	0
Al	19672	20228	20120	15914	15051	14943	1.765471
P	327.49	342.72	327.08	262.11	357.07	519.1	0.035592833
Si	163056	164694	166334	150051	150496	151316	15.76578317
Cl	72.24	103.25	92.58	124.11	96.24	121.28	0.010161667
Mg	< LOD	< LOD	< LOD	< LOD	< LOD	< LOD	0
Total Average Percent							100.0231223
Others Total Percent							2.9951065

Table F3: Mancos Shale Sample Chemical Analysis

Elements	Sample Mancos Shale PL TEXT SIDE	1	2	3	4	5	Average Percent
Mo	1.73	1.67	1.99	1.26	1.54	1.62	0.0001635
Zr	163.91	164.86	164.96	167.72	167.8	167.9	0.016619167
Sr	129.32	130.96	129.83	130.44	129.46	128.67	0.012978
U	6.53	7.34	5.34	6.31	6.45	6.66	0.000643833
Rb	86.78	87.11	87.04	79.26	78.88	78.14	0.008286833
Th	6.46	6	5.83	5.62	6	5.58	0.0005915
Pb	17.72	18.35	18.56	16.07	16.03	17.17	0.001731667
Au	8.96	9.04	10.45	8.35	8.81	10.46	0.0009345
Se	3.32	3.77	3.45	3.81	2.47	2.48	0.000321667
As	4.87	4.79	3.9	3.8	4.39	3.35	0.000418333
Hg	6.96	4.18	< LOD	5.06	5.19	5.93	0.0005464
Zn	55.74	59.71	58.23	56.11	58.3	58.36	0.005774167

W	< LOD	< LOD	< LOD	17.75	17.39	< LOD	0.001757
Cu	28.47	23.81	23.99	22.2	24.37	24.51	0.002455833
Ni	153.91	156.87	156.34	153.91	149.01	164.2	0.015570667
Co	73.44	60.89	59.51	52.08	65.62	63.52	0.006251
Fe	14141.42	14269	14184	12898	12767	12761	1.3503205
Mn	258.27	266.85	247.95	264.31	256.58	262.29	0.0259375
Cr	69.08	73.75	72.04	59.66	60.81	63.51	0.0066475
V	82.42	77.4	83.24	72.04	67.25	70.8	0.0075525
Ti	3303.43	3306.7	3315.5	2981.6	2977.5	2982	0.314446667
Sc	156.58	143.48	143.25	148.82	157.93	139.06	0.014818667
Ca	46997.44	47507	47332	52323	52228	52198	4.9764075
K	19699.29	19846	19702	18245	18346	18143	1.899693667
S	3359.48	3386	3381.6	2952.6	2955.7	2965.7	0.316684167
Ba	460.92	455.76	461.54	464.71	462.43	452.43	0.045963167

Cs	19.68	19.12	19.32	19.58	19.8	18.95	0.001940833
Te	193.06	189.91	185.08	194.77	187.03	187.91	0.018962667
Sb	110.51	102.37	104.59	104.37	113.33	100	0.010586167
Sn	65.75	64.77	64.02	64.86	66.03	63.73	0.006486
Cd	5.22	4.9	5.22	6.09	5.49	5.27	0.0005365
Ag	< LOD	< LOD	< LOD	< LOD	< LOD	< LOD	0
Pd	12.83	10.07	11.68	9.18	11.3	9.59	0.0010775
Bal	528210.25	524312	521027	526825	527072	526456	52.56504417
Nb	9.46	9.9	8.57	8.17	8.31	8.07	0.000874667
Bi	8.52	7.86	7.74	7.53	8.13	7.58	0.000789333
Re	< LOD	< LOD	< LOD	< LOD	< LOD	< LOD	0
Ta	< LOD	< LOD	< LOD	< LOD	< LOD	< LOD	0
Hf	< LOD	< LOD	< LOD	< LOD	< LOD	< LOD	0
Al	65874.37	66587	67729	56983	58120	57930	6.220392167

P	969.78	1032.6	1010.9	996.32	905.67	979.45	0.0982465
Si	302818.41	305025	305864	310943	311980	312963	30.82655733
Cl	24.42	< LOD	31.36	30.32	32.95	22.41	0.0028292
Mg	13878.91	13951	15688	14030	11821	11823	1.353196667
Total Average Percent							100.1410356
Others Total Percent							10.42904193

Table F4: Marcellus Shale Sample Chemical Analysis

Elements	Sample Marcellus Shale PL NON TEXT SIDE	1	2	3	4	5	Average Percent
Mo	10.8	10.64	10.46	11.89	11.34	12.22	0.0011225
Zr	2.17	2.89	2.74	2.23	3.31	3.21	0.000275833
Sr	316.82	317.37	315.36	237.18	237.86	236.41	0.027683333
U	< LOD	< LOD	< LOD	< LOD	< LOD	< LOD	0

Rb	5.87	5.98	6.37	5.29	5.87	5.66	0.000584
Th	< LOD	< LOD	< LOD	< LOD	< LOD	< LOD	0
Pb	8.2	7.7	7.38	28.35	34.05	35.93	0.002026833
Au	< LOD	< LOD	< LOD	< LOD	< LOD	< LOD	0
Se	< LOD	< LOD	< LOD	< LOD	< LOD	< LOD	0
As	< LOD	3.63	3.36	6.6	11.85	10.94	0.0007276
Hg	< LOD	< LOD	< LOD	< LOD	< LOD	< LOD	0
Zn	6.98	6.64	< LOD	42.82	37.11	39.67	0.0026644
W	< LOD	< LOD	< LOD	< LOD	< LOD	< LOD	0
Cu	16.14	18.87	22.08	31.86	38.42	27.69	0.002584333
Ni	< LOD	< LOD	< LOD	< LOD	< LOD	< LOD	0
Co	< LOD	< LOD	< LOD	< LOD	< LOD	< LOD	0
Fe	2790.22	2795.98	2792.21	4844.07	4824.25	4830.15	0.381281333
Mn	219.08	194.29	186.03	222.81	208.8	219.55	0.020842667

Cr	< LOD	< LOD	< LOD	< LOD	< LOD	< LOD	0
V	55.44	66.67	56.96	47.9	62.84	46.96	0.005612833
Ti	164.29	160.85	144.48	129.3	174.6	157.78	0.015521667
Sc	< LOD	< LOD	< LOD	< LOD	< LOD	< LOD	0
Ca	430625.97	430989.47	430721.2	433329.3	434051.2	434073.8	43.2298475
K	3118.56	3052.57	3067.83	3462.92	3456.26	3400.03	0.3259695
S	2049.69	1972.03	1901.9	4508.76	4526.04	4509.23	0.324460833
Ba	424.04	436.61	436.22	438.78	429.78	441.01	0.043440667
Cs	23.35	23.5	23.74	22.82	22.36	23.68	0.002324167
Te	223.49	227.82	241.71	220.39	223.27	232.05	0.022812167
Sb	124.93	118.01	126.04	121.22	123.42	125.81	0.012323833
Sn	86.82	82.79	87.9	84.61	76.53	87.51	0.008436
Cd	6.78	6.36	7.17	5.5	5.77	6.58	0.000636
Ag	< LOD	< LOD	< LOD	< LOD	< LOD	< LOD	0

Pd	19.09	18.17	17.08	18.19	11.41	16.94	0.001681333
Bal	539741.94	539482.94	539971.4	531903.4	532239.1	530011.9	53.455843
Nb	2.19	1.86	2.21	< LOD	2.4	2.32	0.0002196
Bi	< LOD	< LOD	< LOD	< LOD	< LOD	< LOD	0
Re	< LOD	< LOD	< LOD	< LOD	< LOD	< LOD	0
Ta	< LOD	< LOD	< LOD	< LOD	< LOD	< LOD	0
Hf	< LOD	< LOD	< LOD	< LOD	< LOD	< LOD	0
Al	2073.66	2083.32	2267.78	2354.63	< LOD	3454.91	0.244686
P	< LOD	< LOD	< LOD	181.46	< LOD	141.02	0.016124
Si	19895.75	19751.04	19420.21	19635.03	19613.93	19893.49	1.9701575
Cl	112.45	102.69	104.54	278.65	248.76	242.96	0.0181675
Mg	< LOD	< LOD	< LOD	< LOD	< LOD	< LOD	0
Total Average Percent							100.2380569
Others Total Percent							1.790230533

Appendix G: Certificate of Certified Reference Materials

Certificate of Certified Reference Materials

NCS DC 73307 —NCS DC 73312

Stream Sediment

Reissued in 2014

Approved by China National Analysis Center for Iron and Steel

(Beijing, China)

Table G1: Certified Values of Stream Sediment Reference Materials

µg/g	NCS DC 73307	NCS DC 73308	NCS DC 73309	NCS DC 73310	NCS DC 73311	NCS DC 73312
Ag	0.089±0.015	0.27±0.03	3.2±0.5	1.15±0.16	0.048±0.015	0.066±0.015
As	8.41.4	25±4	188±20	115±9	2.0±0.4	6.2±0.9
Au	(0.0013)		(0.0036)	(0.0056)		
B	54±9	26±6	68±7	24±3	4.6±1.1	10.8±3.7
Ba	430□27	42±11	260±26	206±23	950±100	185±37
Be	1.8±0.4	0.9±0.3	26±4	8.2±1.1	3.0±0.5	17.1±1.6
Bi	0.42±0.06	0.38±0.05	50±5	10.9±1.3	0.66±0.11	1.64±0.17
Br	(1.5)	(2.4)	(2.3)	(1.7)		
Cd	0.26±0.05	1.12±0.12	2.3±0.2	4.0±0.4	0.088±0.022	0.065±0.016
Ce	78±9	38±5	58±5	61±5	81±10	192±5
Cl	(50)	(50)	290±32	(163)		
Co	14.4 ±1.8	15.3±1.7	8.5±1.2	8.8±1.1	20.4±3.3	2.6±1.0
Cr	85±10	136±15	40±4	35±4	194±15	12±4
Cs	5.1±1.0	2.3±0.6	17.4±1.0	7.9±0.5	5.1±0.6	16.6±1.8
Cu	32±3	22.6±2.0	79±4	1230±51	22±2	4.9±0.7
Dy	5.1±0.3	2.2±0.3	7.2±0.8	4.8±0.2	4.4±0.6	11±2
Er	2.8±0.3	1.3±0.2	4.6±0.6	3.1±0.3	2.3±0.2	8.2±0.4
Eu	1.33±0.09	0.47±0.05	0.60±0.08	0.61±0.04	1.8±0.2	0.49±0.09
F	494±39	149±38	1650±130	1250±61	870±75	1980±250
Ga	14.0±0.9	6.4±1.0	18.5±1.3	14.1±0.7	23.0±1.4	27.4±1.7
Gd	5.5±0.4	2.2±0.3	5.9±0.5	4.4±0.4	6.1±1.6	9.5±1.4
Ge	1.3±0.2	0.40±0.06	1.81±0.23	1.87±0.13	1.3±0.5	1.7±0.4
Hf	9.7±1.6	1.8±0.4	5.4±0.5	8.3± 1.1	10±2	20±2
Hg	0.083±0.014	0.28±0.04	0.072±0.014	0.056±0.008	0.018±0.004	0.040±0.009

Ho	0.96±0.08	0.45±0.08	1.4±0.2	0.94±0.09	0.88±0.06	2.6±0.4
I	(0.61)	1.6±0.4	2.0±0.3	1.8±0.3		
In	0.056 ±0.008	0.067±0.015	1.9±0.3	0.96±0.17	0.064±0.012	(0.046)
La	40±4	13.0±1.4	30±3	32.7±2.2	43±10	90±10
Li	30±2	13.0±0.7	71±3	39.0±1.5	29.6±2.0	101±6
Lu	0.45±0.04	0.19±0.04	0.78±0.08	0.58±0.08	0.42±0.11	1.6±0.3
Mn	620±30	1010±44	2490±130	1400±73	920±60	240±30
Mo	0.64±0.16	1.2±0.2	5.9±0.8	8.4±0.9	0.74±0.20	2.0±0.4
Nb	18±3	6.8±1.9	25±4	15.4±1.6	35±5	95±9
Nd	34±3	11.8±1.6	27±3	26±4	39±5	62±8
Ni	32±4	30±3	14.3±1.5	12.8±1.9	76±11	5.5±2.1

µg/g	NCS DC 73307	NCS DC 73308	NCS DC 73309	NCS DC 73310	NCS DC 73311	NCS DC 73312
P	670±36	271±23	255±42	235±34	1490±90	200±42
Pb	23±4	27±3	636±34	285±16	24±5	32±8
Pr	9.2±0.9	3.2±0.4	7.4±0.6	6.9±1.2	10.1±1.3	18.6±2.4
Rb	80±4	9.2±2.3	408±17	270±15	116±9	470±33
S	150±30	90±20	170±30	940±60	80±8	89±16
Sb	0.81±0.23	6.3±0.9	14.9±1.8	24±4	0.22±0.10	0.46±0.17
Sc	11.1±0.8	4.1±0.5	7.4±0.6	5.1±0.6	15.6±1.7	4.4±0.7
Se	0.16±0.06	0.28±0.06	0.20±0.06	0.25±0.04	(0.07)	0.20±0.06
Sm	6.3±0.5	2.4±0.2	6.2±0.4	5.0±0.5	7.2±0.6	10.8±1.0
Sn	2.6±.5	1.4±0.4	370±68	54±7	3.1±0.9	29±4
Sr	166±14	25±4	29±5	24±4	525±63	28±11
Ta	1.3±0.2	(0.5)	5.7±0.5	3.2±0.3	3.7±0.3	15.3±1.0
Tb	0.87±0.13	0.42±0.11	1.13±0.14	0.82±0.08	0.86±0.10	1.8±0.3

Te	(0.04)	0.08±0.03	(0.36)	0.29±0.07		(0.03)
Th	12.4±1.0	5.0±0.4	23.3±1.8	21.4±1.7	28±3	70±5
Ti	5500±250	1270±100	2100±150	1510±70	5870±300	1380±120
TI	0.49±0.10	0.21±0.06	2.9±0.5	1.76±0.37	0.61±0.14	1.9±0.5
Tm	0.44±0.09	0.20±0.04	0.74±0.11	0.53±0.07	0.39±0.07	1.55±0.17
U	2.6±0.6	2.1±0.3	9.1±1.3	7.8±1.0	4.4±0.5	17±3
V	97±8	107±7	47±5	47±6	121±11	16.5±2.8
W	1.8±0.3	1.6±0.4	126±13	37±3	1.04±0.30	24±3
Y	27±3	14±3	43±8	29±4	22±4	67±13
Yb	2.8±0.4	1.2±0.3	5.1±0.8	3.7±0.5	2.4±0.4	11±2
Zn	78±5	46±5	373±21	498±27	79±10	44±7
Zr	370±31	70±9	153±19	234±25	310±35	460±40
%						
SiO2	64.89±0.16	88.89±0.29	76.25±0.27	77.29±0.19	58.41±0.22	69.91±0.18
Al2O3	10.58±0.15	2.84±0.11	10.37±0.15	9.30±0.17	14.84±0.11	15.72±0.14
TFe2O3	4.86±0.11	3.86±0.13	4.39±0.11	4.88±0.13	7.35±0.13	1.90±0.08
FeO	1.53±0.07	(0.26)	(0.35)	1.19±0.09	2.26±0.14	0.56±0.07
MgO	2.39±0.09	0.12±0.05	0.62±0.10	0.47±0.12	4.14±0.09	0.21±0.03
CaO	5.35±0.14	0.70±0.04	0.47±0.04	1.16±0.07	4.61±0.10	0.25±0.06
Na2O	1.44±0.06	0.039±0.014	0.46±0.04	0.44±0.04	3.48±0.14	3.03±0.14
K2O	1.99±0.08	0.125±0.020	3.28±0.10	2.91±0.06	2.77±0.09	5.20±0.13
H2O+	2.93±0.27	(2.1)	2.67±0.15	2.15±0.12	2.30±0.15	2.58±0.20
CO2	4.20±0.11	0.42±0.06	(0.09)	(0.18)	(0.12)	(0.10)
Org.C	0.46±0.05	0.40±0.04	(0.24)	(0.40)	(0.18)	(0.39)
L.O.I	7.21±0.22	2.88±0.15	(3.02)	2.62±0.17		
∑(Corr)	100.66	100.24	100.21	100.35	99.86	100.16

Note: Data behind ± are standard deviation; Data enclosed in brackets are proposed values.

Table G2: Analytical Methods

Composition	Methods	Composition	Methods
Ag	AA; AAN; ES; NA	Pb	AA;ES;ICP;ID;POL;XRF
As	AAH; AF; COL; POL; ES;NA;XRF	Pr	ICP;MS;NA
Au	AAN; ES	Rb	AA;FP;NA;XRF
B	COL; ES; ICP	Sb	AA;AAH;AF;COL;POL;ES;NA
Ba	AA; AAN; ES; ICP; NA; MS; XRF	Sc	ES;ICP;NA;XRF
Be	AAN; COL; ES; ICP; POL	Se	AAN;AF;COL;ICP;POL
Bi	AAN;AAH;AF;COL;POL;MS;ES;ICP	Sm	AAN;ICP;ID;MS;NA
Br	COL;IC;NA	Sn	AAN;POL;COL;ES;MS;XRF
Cd	AAN;AAP;ES;ICP;POL	Sr	AA;AAN;ES;ICP;NA;XRF
Ce	ICP;ID;MS;NA;XRF	Ta	COL;ICP;NA
Cl	COL;IC;ISE;NA	Tb	AAN;ICP;MS;NA
Co	AA;AAN;COL;ES;ICP;NA;POL;XRF	Te	AAN;AF;COL;POL
Cr	AA;COL;ES;ICP;NA;XRF	Th	COL;ICP;MS;NA;POL;XRF
Cs	AA;FP;NA	Ti	COL;ICP;NA;XRF
Cu	AA;COL;ICP;POL;XRF	Tl	AAN;COL;POL;ES;MS
Dy	AAN;ICP;ID;MS;NA	Tm	AAN;ICP;MS;NA
Er	AAN;ICP;ID;MS;NA	U	COL;DNA;ID;MS;NA;POL;XRF
Eu	AAN;ICP;MS;NA	V	COL;ES;ICP;NA;POL;XRF
F	COL;ISE	W	COL;NA;MS;POL;XRF
Ga	AAN;COL;POL;ES;ICP;XRF	Y	AAN;ES;ICP;MS;XRF

Gd	ICP;MS;NA	Yb	AAN;ES;ICP;ID;MS;NA
Ge	AAN;COL;POL	Zn	AA;ICP;NA;POL;XRF
Hf	COL;MS;NA;XRF	Zr	COL;ES;ICP;MS;NA;POL;XRF
Hg	AA;AAP;AF	SiO2	GR;ICP;VOL;XRF
Ho	AAN;ICP;MS;NA	Al2O3	COL;ICP;VOL;XRF
I	COL;ISE;NA;POL;VOL	TFe2O3	AA;COL;ICP;NA;VOL;XRF
In	AAN;ES;NA;POL	FeO	COL;VOL
La	ICP;MS;NA;XRF	MgO	AA;GR;ICP;VOL;XRF
Li	AA;FP;ICP	CaO	GR;ICP;VOL;XRF;AA
Lu	ICP;MS;NA	Na2O	AA;FP;ICP;NA;XRF
Mn	AA;COL;ICP;NA;POL;XRF	K2O	AA;FP;ICP;NA;XRF
Mo	COL;ES;NA;MS;POL;XRF	S	VOL;XRF
Nb	COL;ES;ICP;MS;XRF	H2O+	GR;EL
Nd	ICP;ID;MS;NA;XRF	CO2	GR;VOL
Ni	AA;AAN;COL;ES;ICP;NA;POL;XRF	Org.C	GR;VOL
P	COL;ICP;XRF	L.O.I	GR

Note:

AA: Flame Atomic Absorption spectrometry

AAH: Atomic Absorption spectrometry with hydridegeneration

AAN: Non-flame Atomic Absorption spectrometry

AF: Atomic Fluorescence spectrophotometry

COL: Colorimetry

DNA: Delay Neutron Activation method

EL: Electrometric method

ES: Emission Spectrography

FP: Flame Photometry

IC: Ion Chromatography

ICP: Inductively Coupled Plasma spectrography

ID: Isotope Dilution spark source mass spectrometry

ISE: Ion Selective Electrode method

GR: Gravimetry

LF: Laser Fluorescence spectrometry

MS: Mass Spectrometry

NA: Neutron Activation analysis

POL: Polarography

VOL: Volumetry Fluorescence spectrometry

XRF: X-Ray

Professor Wang Haizhou, Chief
China National Analysis Center for Iron and Steel